ELECTRICAL, OPTICAL, AND NOISE CHARACTERIZATIONS OF
MWIR TYPE-II INAS/GASB SUPERLATTICE SINGLE PIXEL DETECTORS

A THESIS SUBMITTED TO
THE GRADUATE SCHOOL OF NATURAL AND APPLIED SCIENCES
OF
MIDDLE EAST TECHNICAL UNIVERSITY

BY

KUTLU KUTLUER

IN PARTIAL FULFILLMENT OF THE REQUIREMENTS
FOR
THE DEGREE OF MASTER OF SCIENCE
IN
MICRO AND NANOTECHNOLOGY

SEPTEMBER 2012

Approval of the Thesis:

ELECTRICAL, OPTICAL, AND NOISE CHARACTERIZATIONS OF MWIR TYPE –II INAS/GASB SUPERLATTICE SINGLE PIXEL DETECTORS

Submitted by **KUTLU KUTLUER** in partial fulfillment of the requirements for the degree of **Master of Science in Micro and Nanotechnology Department, Middle East Technical University** by,

Prof. Dr. Canan Özgen
Dean, Graduate School of **Natural and Applied Sciences** _____

Prof. Dr. Mürvet Volkan
Head of Department, **Micro and Nanotechnology** _____

Prof. Dr. Raşit Turan
Supervisor, **Physics Dept., METU** _____

Prof. Dr. Tayfun Akın
Co-Supervisor, **Electrical and Electronics Eng. Dept., METU** _____

Examining Committee Members:

Prof. Dr. Mehmet Parlak
Physics Dept., METU _____

Prof. Dr. Raşit Turan
Physics Dept., METU _____

Prof. Dr. Tayfun Akın
Electrical and Electronics Engineering Dept., METU _____

Assoc. Prof. Dr. Bülent Aslan
Physics Dept., Anadolu University _____

Dr. Tunay Tansel
Physics Dept., METU _____

Date: 13.09.2012

I hereby declare that all information in this document has been obtained and presented in accordance with acedemic rules and ethical conduct. I also declare that, as required by these rules and conduct, I have fully cited and referenced all material and results that are not original to this work.

Name, Last Name : Kutlu Kutluer

Signature :

ABSTRACT

ELECTRICAL, OPTICAL, AND NOISE CHARACTERIZATIONS OF MWIR TYPE-II INAS/GASB SUPERLATTICE SINGLE PIXEL DETECTORS

Kutluer, Kutlu

M. Sc., Department of Micro and Nanotechnology
Supervisor   : Prof. Dr. Raşit Turan
Co-Supervisor   : Prof. Dr. Tayfun Akın

September 2012, 107 pages

Detection of mid-wavelength infrared radiation is crucial for many industrial, military and biomedical applications. Photon detectors in the market can operate at only low temperature which increases weight, power consumption and total cost. Type-II InAs/GaSb superlattice infrared detectors are expected to have a major role in the infrared detector market with providing high quality detection characteristics at higher temperatures. Therefore, in the past decade, there has been an increasing interest in infrared detectors based on type-II InAs/GaSb superlattice technology due to their long range adjustable bandgap, low tunneling current and Auger recombination rates which bring potential of high temperature operation. Characterization of this photodiodes requires detailed investigations on different aspects.

This study focuses on various optical and electrical characterization techniques for single pixel infrared detectors: responsivity characterization using FTIR and blackbody source, dark I-V and R-V characterizations, response time measurement. Characterizations of detector noise with respect to frequency and bias voltage are studied in detail. These characterization techniques are carried out in order to observe the effects of design with three different "standard" and

a new "N" structure designs and also to understand the effects of surface passivation with atomic layer deposited Al_2O_3 layer and ordinary PECVD deposited Si_3N_4 and SiO_2 layers. When standard photodiodes are compared, we observed that the one with the thickest active absorber region has the highest response and dark current density values. "N" structure design photodiode has very low dark current density while its optical performance is not as high as the standard designs. Si_3N_4 passivation degrades both optical and electrical performances. SiO_2 and Al_2O_3 passivation layers improve optical and electrical characteristics of photodiodes. Theoretical and experimental dark current noise values of SiO_2 passivated sample in agreement up to 0.18V reverse bias while those values of unpassivated and Si_3N_4 passivated samples agree only at zero bias. Temperature dependent R-V characteristics of photodiodes are analyzed and the surface limited activation energy is calculated in order to investigate the additional noise. At the end, surface recombination noise is proposed to cover the deficit on the noise calculation.

Keywords: Type-II InAs/GaSb Superlattice, infrared detectors, characterization, noise analysis, surface recombination noise.

ÖZ

MWIR TİP-II INAS/GASB SÜPERÖRGÜ TEK PİKSEL DEDEKTÖRLERİN ELEKTRİKSEL, OPTİKSEL VE GÜRÜLTÜ KARAKTERİZASYONLARI

Kutluer, Kutlu

Yüksek Lisans, Mikro ve Nanoteknoloji Bölümü
Tez Yöneticisi   : Prof. Dr. Raşit Turan
Ortak Tez Yöneticisi   : Prof. Dr. Tayfun Akın

Eylül 2012, 107 sayfa

Orta dalgaboyu kızılötesi ışınım algılama sistemleri endüstriyel, askeri ve biyomedikal uygulamaların birçok alanında çok önemli bir yer işgal eder. Piyasadaki foton dedektörleri sadece düşük sıcaklıklarda çalışabilirler. Bunun sonucunda ağırlık, güç tüketimi ve maliyet artar. Yüksek sıcaklıklarda yüksek kalite algılama özelliği sunabilecekleri için tip-II InAs/GaSb süperörgü dedektörlerin piyasada önemli bir rol oynamaları beklenmektedir. Ayarlanabilir bant aralığı, düşük tünelleme ve Auger birleşme oranı sonucunda yüksek sıcaklıklarda çalışabilme potansiyeli sayesinde son on yıldan beri tip-II InAs/GaSb süperörgü dedektör teknolojilerine artan bir ilgi vardır. Bu sebeple bu dedektörlerin karakterizayonu farklı açılardan detaylı incelemeleri gerektirir.

Bu çalışma, tek piksel kızılötesi dedektörlerin FTIR ve karacisim kullanılarak yapılan tepkisellik karakterizasyonu, karanlık akım gerilim ve direnç gerilim karakterizasyonu ve tepki süresi ölçümü gibi çeşitli optiksel ve elektriksel karakterizasyonları içerir. Bu çalışmada frekansa ve gerilime bağlı gürültü karakterizasyonlarına da odaklanılmıştır. Bu karakterizasyon teknikleri ile standart yapıda 3 farklı ve bir "N" tip yapıda dizaynın etkileri ile Al_2O_3, olağan

Si$_3$N$_4$ ve SiO$_2$ katmaları ile yapılan yüzey pasivasyonunun etkiler incelenmiştir. Basit dizaynları karşılaştırdığımızda, en kalın aktif emilim bölgesine sahip olan foto diyot en yüksek tepkisellik ve karanlık akım değerlerini vermiştir. "N" tip yapı çok düşük karanlık akım yoğunluğuna sahip olsa da optik performansı standart yapılarınki kadar yüksek değildir. Si$_3$N$_4$ pasivasyonu optiksel ve elektriksel özellikleri düşürmüştür. Hem SiO$_2$ hem de Al$_2$O$_3$ pasivasyon tabakaları elektriksel özellikleri de optiksel özellikleri de iyileştirmişlerdir. SiO$_2$ pasivasyonlu örneğin teorik ve deneysel karanlık akım değerleri -0.18V gerilim değerine kadar örtüşürken pasivasyon uygulanmayan and Si$_3$N$_4$ pasivasyonlu örneklerin bu değerleri sadece sıfır gerilim değerinde örtüşmektedir. Foto diyotların sıcaklık bağımlı R-V karakteristikleri analiz edilmiş ve ek gürültüyü inceleyebilmek için yüzey sınırlı aktivasyon enerjisi hesaplanmıştır. Son olarak gürültü hesabındaki eksikliği giderebilmek için yüzey geri birleşme gürültüsü önerilmiştir.

Anahtar kelimeler: Tip-II InAs/GaSb Superörgü, kızılötesi dedektörler, karakterizasyon, gürültü analizi, yüzey geri birleşme gürültüsü.

to my banne..

ACKNOWLEDGEMENTS

I would like to thank to my supervisor Prof. Dr. Raşit Turan who gave me the opportunity to work with him. I am very grateful to him for his support and his enlightened guidance. I am appreciated to him for giving me chance to join the project KOFDE, meet and cooperate with various valueable scientists.

I specially would like to thank to Dr. Tunay Tansel for tranfusing his vast experiences into me. If I have learned something about working systematically, writing scientific papers and reports, it cannot be done without him. I am thankful for his friendship, our endless discussion and his jokes.

I would like to thank to Prof. Dr. Mehmet Parlak for his guidance especially at the beginning of my study, for his support, helpful discussions and kindness.

I would like to thank to Assoc. Prof. Dr. Bülent Aslan for his helpful discussions, sharing his knowledge and experince on all aspects of infrared detectors throughout this study and his valueable friendship.

I would like to thank to Prof. Dr. Atilla Aydınlı and Dr. Ömer Salihoğlu for the fabrication and passivation processes of the samples and for their valuable discussions.

I would like to thank to Prof. Dr. Yüksel Ergün for providing new design sample, for the contributions to the project. I am also thankful to Assoc. Dr. Uğur Serincan, Bülent Arıkan and Melih Korkmaz and other members of Nano Boyut Laboratory.

I would like to thank to Prof. Dr. Tayfun Akın for being my co-supervisor in this thesis study.

TABLE OF CONTENTS

LIST OF TABLES

TABLES

LIST OF FIGURES

FIGURES

xvii

CHAPTER 1

INTRODUCTION

1.1.   Blackbody Radiation

The blackbody phenomenon is one of the most fundamental concepts in quantum physics. Blackbody is a hypothetical entity i.e. an object or a system which absorbs all energy, reflects none and emits energy with perfect efficiency. Its temperature is the only parameter to determine the radiation spectrum. Thus, this theoretical model helps us to determine where the emission of body (object) is in the electromagnetic spectrum (Figure 1.1) at a given temperature.
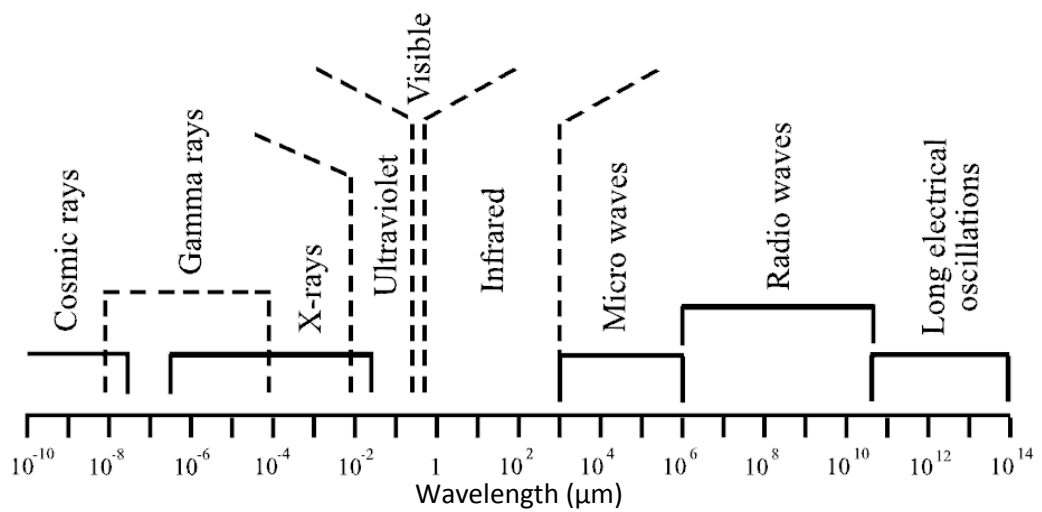
Figure 1.1 Electromagnetic spectrum.

Three laws are used to describe radiation of a blackbody:

1- Planck's law

Planck's Law describes how much energy is radiated of a certain wavelength and at a given temperature:

$$M_e = \frac{2 \cdot \pi \cdot h \cdot c^2}{\lambda^5 \cdot \left\{ \exp\left(\frac{h \cdot c}{\lambda \cdot k \cdot T}\right) - 1 \right\}} \left[\frac{W}{\mu m \cdot m^2} \right] \qquad (1.1)$$

where h is the Planck constant, c is the speed of light, k is the Boltzmann constant, λ is the photon wavelength and T is the blackbody temperature. Figure 1.2 shows Planck curves for different blackbody temperatures.
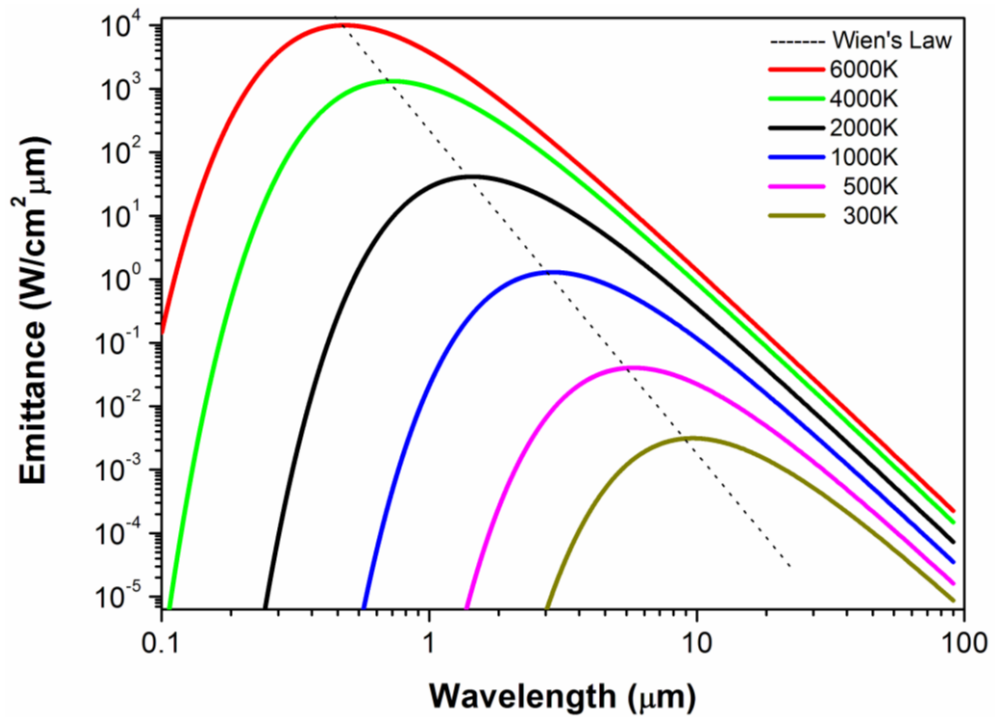
Figure 1.2 Spectral emittance of an ideal blackbody at different temperatures.

It is seen that emittance spectrum of a blackbody at ambient temperature of 300K peaks at 10μm in the infrared range while the blackbody's emittance spectrum peaks at visible range when its temperature at around surface of the sun, 6000K.

2- Wien's Law

Wien's Law describes a relation between temperature of a blackbody and peak wavelength of its emittance spectrum as follows:

$$\lambda_{peak}[\mu m] = \frac{2898}{T\,[K]} \qquad (1.2)$$

Wien's law for different blackbody temperatures is shown in Figure 1.2 as dashed line.

3- Stefan – Boltzmann Law

The total radiated energy from a blackbody at temperature T is stated by Stefan - Boltzmann law and written as

$$M\left[\frac{W}{cm^2}\right] = \sigma \cdot T^4\,[K^4] \qquad (1.3)$$

where σ is Stefan-Boltzmann constant (5.6705×10^{-12} W/ (cm^2.K^4).

The laws mentioned above are for hypothetical, ideal blackbodies. To apply these laws to the real world objects, there is a parameter called emissivity (ε) which refers how close the object acts like ideal blackbody. An ideal blackbody would have ε = 1 and while the object's ability to absorb and radiate energy drops off, emissivity value approaches 0.

1.2. Atmospheric Absorption

Electromagnetic waves would be scattered or absorbed when propagating through a medium. Absorption of electromagnetic waves by atmosphere has important consequences for infrared detection techniques. Carbon dioxide, water vapor and ozone are the most dominant absorber molecules at the atmosphere in the range of infrared spectrum as seen in Figure 1.3. Carbon monoxide, methane and nitric oxide are the other absorbers that have effects on the transmission of infrared light.

Figure 1.3 clearly shows the two parts (also called atmospheric windows) of infrared spectrum, namely Mid-Wave Infrared band and Long-Wave Infrared band which lie in 3 to 5 μm and 8 to 12 μm respectively. Infrared devices for thermal imaging applications are usually designed in accordance with these two windows.
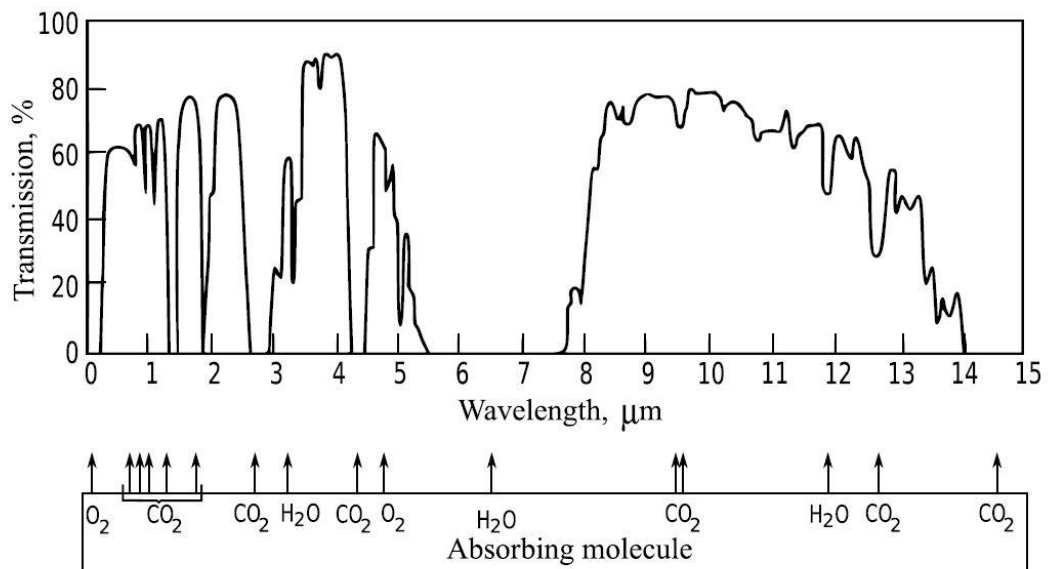
Figure 1.3 Atmospheric transmission of infrared radiation along 2km path at sea level, where precipitable water height is 14mm [1].

4

Infrared radiation is classified by taking into account of atmospheric windows as stated below:

I – Near Infrared Radiation (NIR) covers wavelengths from 0.75 to 1.5 μm;

II – Short Wavelength Infrared Radiation (SWIR) covers wavelengths from 1.5 to 2.5 μm;

III – Medium Wavelength Infrared Radiation (MWIR) covers wavelengths from 3 to 5 μm;

IV – Long Wavelength Infrared Radiation (LWIR) covers wavelengths from 8 to 12 μm;

V – Very Long Wavelength Infrared Radiation (VLWIR) covers wavelengths from 12 to 32 μm.

1.3.   Infrared Detectors

Detector is the main part of the IR sensing system. The incident energy falling upon the detector is transduced into other forms. There are mainly two kind of detectors based on the method of transduction: thermal detectors and photon detectors. Basically, thermal detectors sense the "heat" of the target, on the other hand photo detectors sense the optical radiation emitted by the target.

1.4.1   Thermal Detectors

The principle of thermal detectors is based on two alteration steps. First, the detector's temperature should change with the radiant heat of the target (radiant source), then that changes should be the cause of another change in physical or electrical properties of the detector in order to be measured. The thermal detectors are sensitive to all wavelengths of emitted electromagnetic waves from the object. The only factor that should be concerned about is the intensity of absorbed radiant power.

In thermal detectors, some kinds of processes are utilized for transduction of energy. These processes mentioned below all take places in the second step of the alteration.

- *Bolometric Effect:*
  It is the change of electrical resistance of sensing element due to the absorbed heat from the target.

- *Thermovoltaic Effect:*
  It is based on the consequences of different responses of junction of different metals when absorb heat. The differentiation of response is caused voltage generation.

- *Pyroelectric Effect:*
  The temperature of the crystalline sensing element changes with the absorbed heat which varies the dipole moment of crystalline and creates external electric field.

- *Thermopneumatic Effect:*
  The sensing element in this case is a gas chamber and the pressure of the gas inside the chamber varies with the absorption of heat which varies with the temperature of the gas. The distortion on the flexible mirror placed in the wall of the chamber is detected by an optical system that includes a laser and a detector.

1.4.2. Photon Detectors

The mechanism of photon detectors is based on photoexcitation, the generation of free carriers in the detector. Photon detectors are selectively sensitive to the wavelength of the emitted electromagnetic waves coming from the object and this property is a limiting factor for photon detectors. The incident photon should have a certain amount of

minimum energy to interact with the electrons and creates free electron hole pairs. The minimum amount of energy does vary with the detector material bandgap.

Getting a response from photon detectors is faster than thermal detectors because in photon detectors, the response mechanism is based on electron transportation while it is based on changing physical or electrical properties of sensing element in thermal detectors.

There are different processes also in photon detectors. The two distinct types are below:

- *Photoconductive (PC) Effect:*
  Having electron-photon interactions and creating electron hole pairs increase the amount of free electrons in the conduction band and holes in the valence band. The electrical conductivity of a device is directly proportional to the amount of free carriers hence this process changes the conductivity of the detector called as photoconductive detectors.

  If the photogenerated electrons excite from valence band to conduction band, this kind of photoconductor is called intrinsic photoconductors. The minimum sufficient energy of the incident photon is equal to the band gap of the material. In the other case, which is called extrinsic photoconductors, the transition of carriers is between a localized impurity state and a band. The minimum sufficient energy that the incident photon should have in extrinsic photoconductors is the energy difference between the localized state and the band. This energy is smaller than the band gap of the detector. Therefore the extrinsic photoconductors are used as low bandgap material. Gallium (Ga), antimony (Sb) and arsenide (As) are the most common elements to form localized states in silicon (Si) host crystal.

In order to sweep the photogenerated carriers out into the circuit, an external bias, which causes excessive dark current, is applied as shown in Figure 1.4.
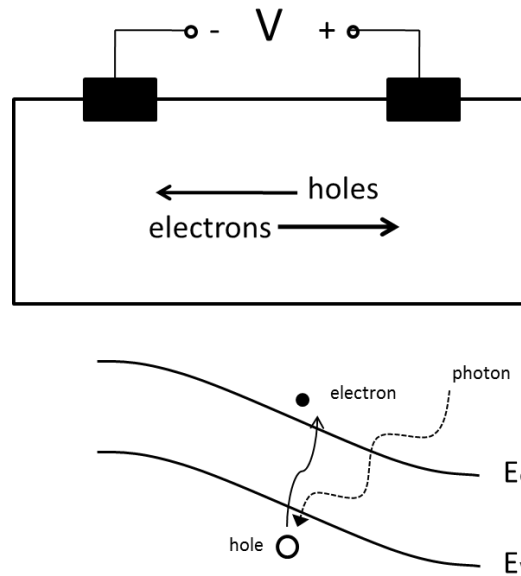
Figure 1.4 Device structure of an intrinsic photoconductor with energy band profile under bias.

- *Photovoltaic (PV) Effect:*

  In semiconductor photovoltaic detectors, created electron hole pairs by photons generate additional voltage difference, that sweeps the free carriers to the contacts, between n-doped and p-doped regions of the p-n junction and it is called as photovoltaic effect. The electron hole pair generation process is similar with the photoconductors however transport of the carriers is realized by the internal electric field at the junction. Thus, the carriers in the junction region, called depletion region, or those created at distance smaller than the diffusion length from the

depletion region are the only carriers those can survive without recombination.

When a p-n junction is formed in a semiconductor, electrons from n-type region diffuse to the p-type side and recombine with the holes there. Similarly, holes from p-type side diffuse to n-type side and recombine with the electrons. The junction region is then depleted from the holes and electrons, leaving behind ionized fixed dopant ions on each side of the junction. This region is called depletion region in which oppositely charged ion cores form an electric field which sweeps any free carriers those can be created by optical excitation.
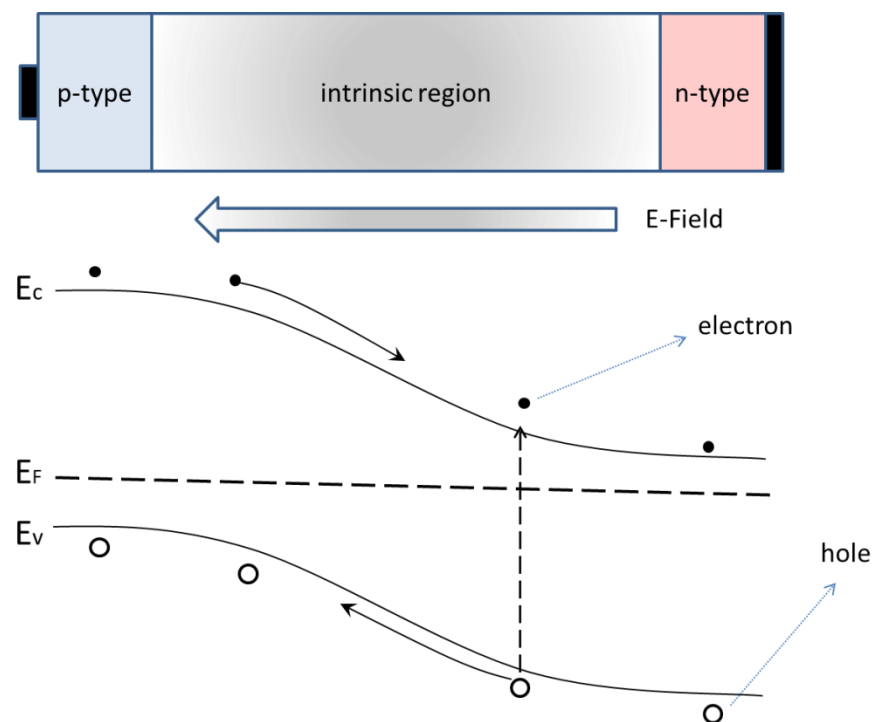
Figure 1.5 Device structure of p-i-n photodiode with energy band diagram.

In order to increase photogenerated current, an intrinsic layer is usually inserted between p-type and n-type regions and, the device is called as p-i-n photodiode (Figure 1.5).

In this case, the electric field is extended across the intrinsic region that can be made wider compare to a p-n junction. The total number of absorbed photons is increased by the extension of the device's active absorber region.

1.4.3. Competitive IR Detector Technologies

Several detector alternatives are available for different aims of applications. HgCdTe (MCT) detectors, InSb detectors, GaAs/AlGaAs Quantum Well Infrared Photodetectors (QWIPs) and microbolometers are the most favorite detector types in field applications for various reasons explained below. Table 1 shows the comparison of the major properties of these technologies [2], [3].

- *Mercury Cadmium Telluride (MCT, HgCdTe) Detectors:*
$Hg_{1-x}Cd_xTe$ detectors were the first generation linear IR detector arrays developed in early 1970's [4] and even today it is the state of the art detector type. By changing the mole fraction of the CdTe, the band gap of the detector can be tailored from 0 to 1.5 eV which covers 1μm - 30μm range of electromagnetic spectrum. The variability of bandgap allows designing dual-band HgCdTe detectors.

The detector structure is grown on CdZnTe substrate. The lattice parameter of detector is almost independent from the mole fractions of the $Hg_{1-x}Cd_xTe$ which brings a great benefit. MCT detectors can reach quantum efficiencies higher than 80% due to their large optical absorption coefficients [5]. Another major advantage of MCT detector is the operability in relatively high temperatures due to the low dark

current density. However, high defect concentration in CdZnTe and HgCdTe which lowers the material quality is the major drawback for MCT detectors. In focal plane array (FPA) applications, one the most important factor is uniformity in large wafers which is a very challenging issue in HgCdTe material system [6]. Another disadvantage of MCT detector is highly dependency of band gap to mole fraction rate. During the growth process, temperature of the system should be precisely (ΔT = 1 - 5 $^\circ$C) under control to attain accurate composition rate. High tunneling currents due to low electron effective mass is another drawback for MCT detectors.

- *InSb Detectors:*

  Growth process of InSb detectors is comparatively easy due to the fact that InSb structure is not a heterojunction. Thus, InSb detectors are highly developed and commonly used. InSb has band gap of 0.23meV at 77K which is equal to 5.4μm cut-off wavelength in the MWIR region of spectrum however the optical absorption coefficient begins rising at 5.2 μm. With increasing temperature, cut-off wavelength of the device shifts to higher wavelengths. Quantum efficiency of InSb detectors is higher than 60% at 77K [7]. Nonetheless, it will be lower at the temperatures under 60K by decreasing lifetime of the minority carriers.

  The most limiting drawback of InSb detectors is its operation temperature that is in the range of 4 - 80 K. In addition, the uniformity of InSb detectors degrades by time and the number of cooling down processes. Correction in imaging system is a necessity to overcome that problem which is impossible in some field applications such as metrology. Therefore InSb detectors are preferred in the high sensitivity MWIR applications where reproducibility is a concern and corrections are doable.

- *GaAs/AlGaAs QWIPs:*

  GaAs/AlGaAs quantum well infrared photodetectors is a product of a totally new approach. Levine *et. al.* performed the first demonstration of high performance QWIP in LWIR band [**8**]. The idea of creating photocurrent in QWIPs is based on photoexcitation of electrons from bound energy states of multi quantum wells to bound, quasi bound or continuum states depending on application. For the photo excited electrons, there is an undesired possibility of capturing by another quantum well. The energy gap between bound and higher states can be predefined before the growth by determining the thickness of quantum wells. Thin layers of low bandgap materials are placed between two high bandgap materials repetitively in order to form multi quantum well structures. Overlapping of wave functions of the electrons at neighbor quantum wells is avoided by large quantum well barrier thickness. In photoconductor QWIP devices, a voltage bias is applied to the device in order to bend the band structure and some cases to lower the barrier height. A schema of the process is shown in Figure 1.6.

  GaAs growth and processing technologies are one the most important advantages of GaAs/AlGaAs QWIPs. QWIPs are grown by Molecular Beam Epitaxy (MBE) instrument. GaAs products can be well controlled, highly uniform even in large area wafer. Therefore QWIPs are low cost and high yield material with respect to HgCdTe based photodetectors.

  In quantum wells, electrons reside in discrete confined states which have selection rules for absorption. Due to the selection rules, which require electric field of incident light to be parallel to the direction of quantum confinement, normal incident photon cannot be absorbed by the electrons in the quantum well. Therefore, to maximize the absorption, QWIP device is placed tilted with an angle of 45° or a grating is required on the surface of the device. As a result of the selection rules, quantum efficiency of QWIPs cannot be as high as other competitor detectors.
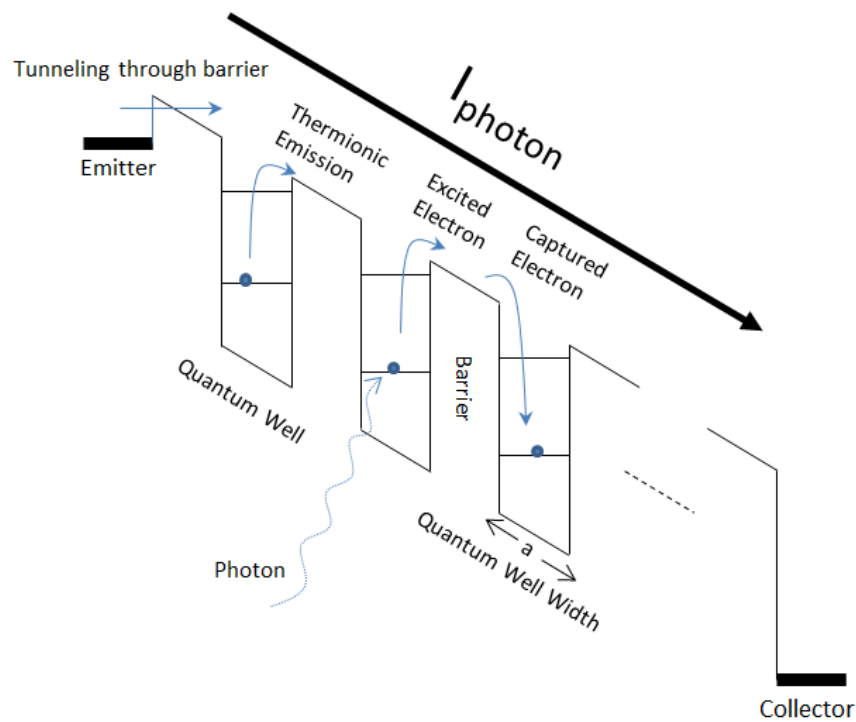
Figure 1.6 QWIP Operating Principle.

- *Microbolometers:*

  Operation principle of microbolometers depends on bolometric effect of thermal detectors. When infrared radiation heats the detector, change in the temperature of sensing element is measured as an electrical signal formed by the system. For higher sensitivity, one needs to obtain maximum temperature variation at detector sensitive element under exposure of a certain infrared radiation. This means that the thermal capacity of the microbolometer should be as small as possible. The optimization of the effect of radiation flux on the detector is related with the reducing thermal contacts with the surroundings which can be achieved by small detector sizes. Alternatively, the absorbing part of the detector is isolated from surrounding by applying micromachining technologies. These challenges are triggering the microbolometer infrared detectors research.

13

Table 1.1 Essential properties of HgCdTe, InSb, QWIP and type-II SL photodiodes at their operating temperatures.

	Quantum efficiency	Cut-off	Operation Temperature	Detectivity (Jones)	Spectral Sensitivity	Multi color, multiband capability	Homogenity
InSb (3-5μm)	>60%	5.7μm	<90K	>10^{11}	Wide	No	No
HgCdTe (3-5μm)	>80%	Adjustable	<140K	>10^{12}	Wide	Yes	No
HgCdTe (8-11.5 μm)	>70%	Adjustable	<80K	>10^{12}	Wide	Yes	No
AlGaAs/GaAs QWIP (3-5 μm)	~20%	Adjustable	88K	>10^{11}	Narrow but tunable	Yes	Yes
AlGaAs/GaAs QWIP (8-12 μm)	~10%	Adjustable	<70K	>10^{10}	Narrow but tunable	Yes	Yes
Type-II Superlattices (3-5 μm)	>30%	Adjustable	<120K	>10^{12}	Wide	Yes	Yes
Type-II Superlattices (8-11.5 μm)	>20%	Adjustable	<80K	>10^{11}	Wide	Yes	Yes
Microbolometers	NA	Infinity	300 K	>10^{9}	All Spectra	No	Yes

CHAPTER 2

INAS/GASB TYPE-II SUPERLATTICE PHOTODETECTORS

Fundamental research on InAs/GaSb superlattice was initiated theoretically by Tsu and Esaki in the 1970s [9]. They also demonstrated optical absorption behavior of InAs/GaSb superlattice. About 10 years later, Smith and Mailhiot published an article which proposed development of superlattice structures for infrared detection [10]. Type II infrared detectors have attracted research groups enormously since the late 1990s.

2.1.   General Properties and Types of InAs/GaSb Type-II Superlattice Photodetectors

The origin of the Type-II Superlattice Structure is based on Quantum Well Structures which can also be called as Type-I Quantum Wells. Actually, there are three types of band alignments; Type-I, Type-II Staggered and Type-II Misaligned as seen in Fig 2.1.

These band alignments have two different and very thin material layers, shorter than the electrons mean path, which results in quantum confinements of energy levels – discrete energy states. Material A acts as a potential barrier for electrons in the conductor band of the neighbor material in all cases. The main difference between Type-I case and Type-II cases is the localization layer of holes' energy states which is in the valence band of Material A in Type-II cases

where it is in the valence band of Material B in Type-I case. It is a consequence of laying the valence band of Material C and D under valence band of Material A.
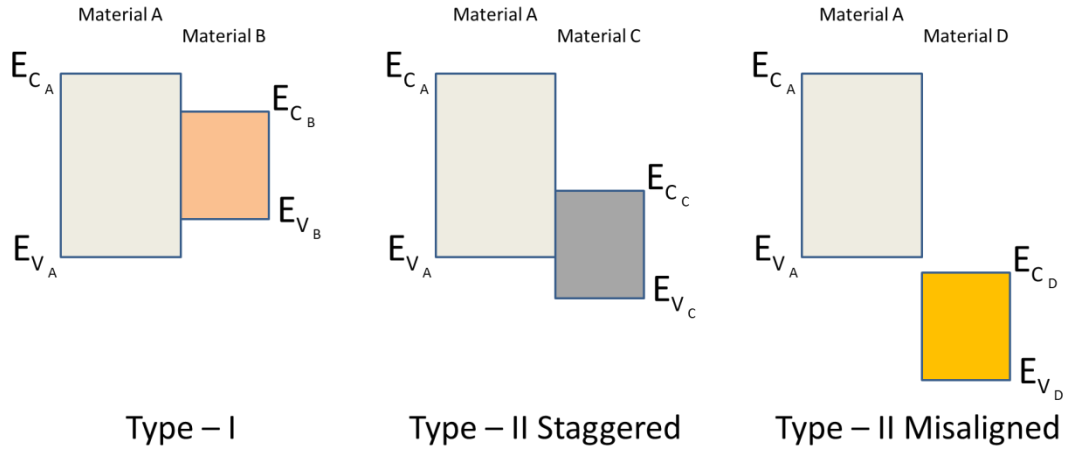
Figure 2.1 Three possible band alignments.

The material type we've investigated is InAs/GaSb which is Type-II Misaligned. It is called as superlattice due to the fact that the period of the lattice is not determined by the lattice constant; but it is determined by the period of layers. If the period of superlattice is shorter than the mean free path of electrons, the whole electron system is in the quantum regime [**11**]. In InAs/GaSb Type-II Superlattice structures, the conduction band of the InAs lies under the valence band of GaSb therefore electrons and holes are not localized in the same material layer (Fig 2.2). Tunneling probability of electrons and the probability of electrons wavefunction overlap in the conduction band of InAs layers increase with the thinner GaSb layers and amount of periodic InAs/GaSb layers. Thus, wavefunction overlap constitute electron miniband. Thinner InAs layer and amount of periodic InAs/GaSb layers also increase the probability of

wavefunction overlap of holes, therefore hole miniband also forms. The energy gap, which determines the region of infrared detector, between the minima of electron miniband and the maxima of hole miniband is the bandgap of InAs/GaSb Type-II Superlattice structure as seen Fig 2.3.

The effective bandgap of the new semiconductor can be tailored over a wide range (from 3 μm to 30 μm) by changing the thicknesses of GaSb and InAs layers. Figure 2.4 shows that the change in bandgap energy with different thickness of layers (the thickness of InAs and GaSb layers are assumed to be equal). Thicker layers form wider quantum wells, which lowers ground energy state in the quantum wells hence the energy difference between electron and hole minibands gets closer.

Therefore, in order to obtain smaller bandgap and higher cutoff wavelengths, structure should be grown with thicker layers which also lower the tunneling probability of electrons and holes.
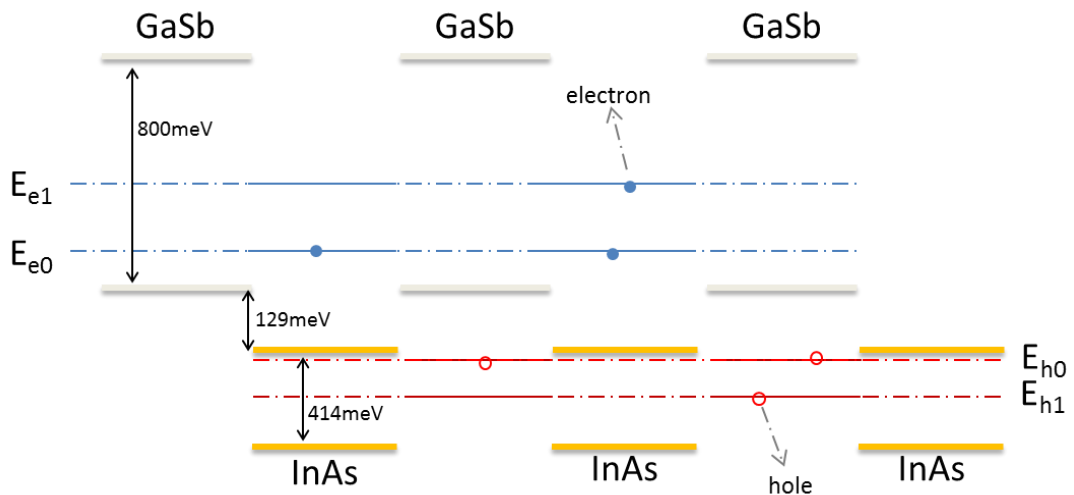
Figure 2.2 Heterojunction formed by three layers of InAs and GaSb at 70K.

In Type-II InAs/GaSb superlattice, optical absorption is associated with overlapping of electron and hole wavefunctions. If the layer is thick, the optical absorption coefficient will be low due to the low overlapping. Wavefunction overlap occurs at the hetero-interfaces mostly. As a result, optical absorption occurs in the vicinity of interfaces [12]. Hence, for a given superlattice length, optical absorption is related with number of interfaces rather than superlattice length. In addition, the reduced electron hole wavefunctions causes undesirable blue shift at the cut off wavelength [13].
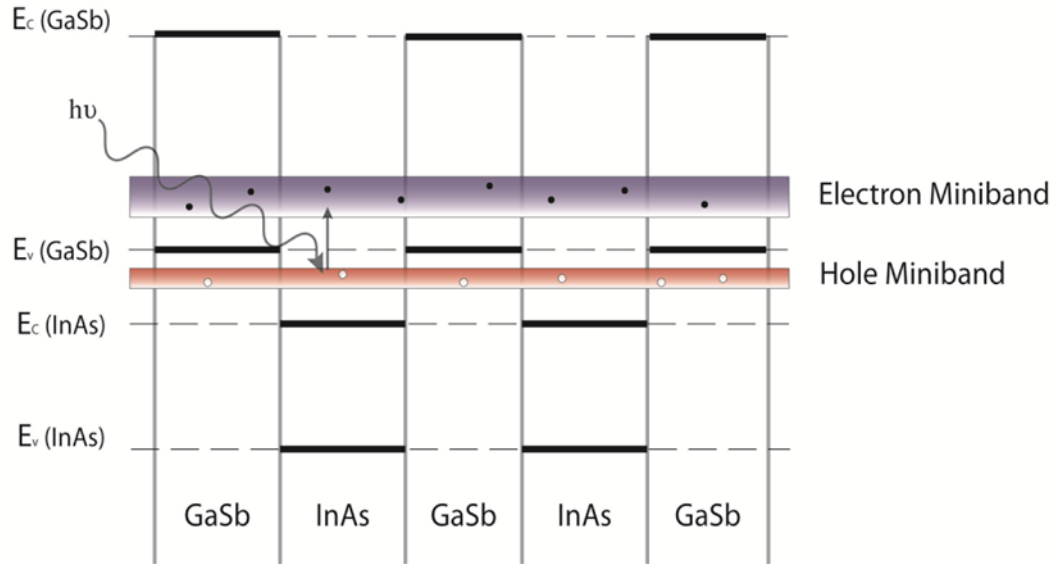
Figure 2.3 Band Structure of InAs/GaSb Type-II Superlattice.

In order to obtain exact results from theoretical calculations, electronic structure of the Type-II superlattice needs to be calculated correctly. Four different methods can be used for the calculations:

- k.p method [14], [15]
- Superlattice Empirical Pseudopotential Method [16]

-        Atomistic Empirical Pseudopotential Method [16]

-        Empirical Tight-Binding Method [17]
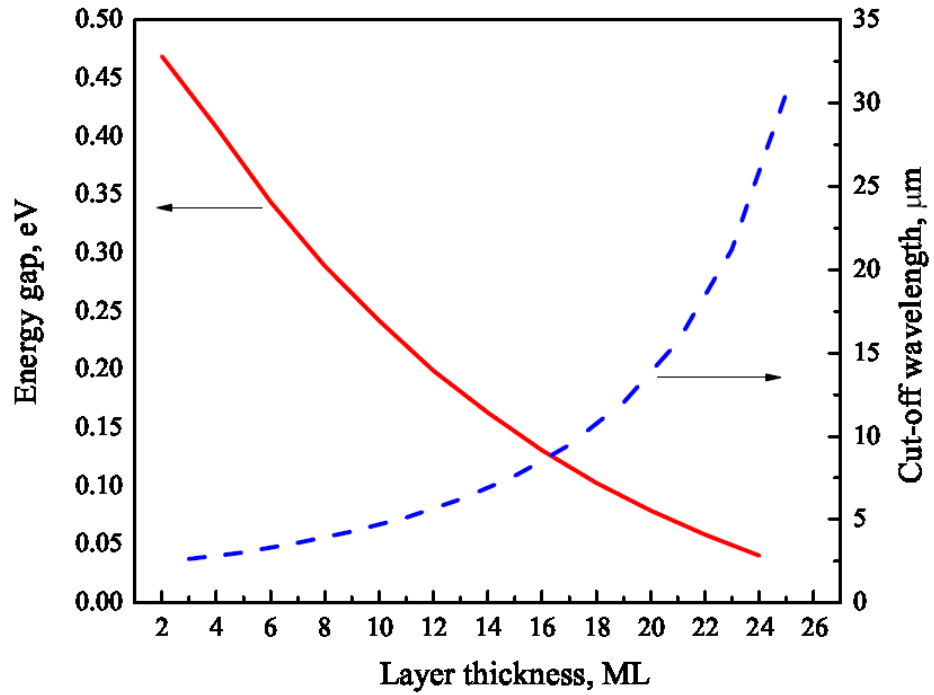
Figure 2.4 Calculated variation of bandgap energy, cut off wavelengths for different layer thickness of InAs/GaSb SL [18].

Even though there is no superior calculation method for the specification of all aspects of a real SL, Empirical Tight-Binding Method stands out with capabilities of calculation of all brillouin zone band structure and, determination of superlattice layers by taking into account of growth errors [19].

The major advantages of SL detectors are: the ability of adjustment of band gap from 3 to 30 μm by varying the thicknesses of the layers which result multi-color FPA applications, reduced tunneling currents due to the larger electron effective mass, and reduced Auger recombination due to large splitting of heavy

and light holes in valence subbands due to strain. High quantum efficiency and responsibility can be reached by growing extremely thick (~6 µm) active regions if the strain at the interfaces is under control. In contrast with QWIPs, normal incidence absorption is permitted which results in high quantum efficiency. Mature large-format FPA production of III-V semiconductor materials technology also offers technological advantages for the SLs.

2.1.1. P-I-N Structure

P-I-N type photodiodes are the most well-known and straight-forward photodiode type. For this reason, most research groups are working on SL photodetectors grown as p-i-n devices. It is based on ordinary p-n junction with an intrinsic region between them as shown in Chapter 1, Fig 1.6. Generally, in p-type region of InAs/GaSb Superlattice Photodetectors, GaSb is usually doped by Be atoms and in n type region, InAs is doped either with Si or Te atoms.

2.1.2. Type II InAs/Ga$_{1-x}$In$_x$Sb Strained Layer Superlattice

Type II InAs/Ga$_{1-x}$In$_x$Sb strained superlattice (SLS) was first proposed in 1984 for the long wavelength photodetectors [20]. In 1988, researchers began to work for first production [21]. In strained superlattice structure, GaSb layer is alloyed with In to get lattice mismatch between GaInSb and InAs layers. Tensile strain due to the smaller lattice parameter of InAs is about – 0.62%. At the transition from GaSb to InAs, group III and group V elements are changed. Depending on the shutter sequence during MBE growth, preferential formation of either GaAs or InAs like interface bonds can be forced to introduce an additional source of strain in the layer stack. In strained superlattice structure, GaSb layer is doped with In molecule to get lattice mismatch between GaInSb and InAs layers. Tetragonal distortions, which shift the bulk energy levels and causes splitting the valence band degeneracies of the light and heavy

20

holes energy levels, are the results of the lattice mismatch. Band edges are shifted due to presence of strain and the energy gap is reduced. In the SLS, the band gap forms between electron states that split upward from the InAs conduction band and heavy hole states split downward from GaInSb valence band. Hence, long wavelength detection can be obtained without decreasing optical absorption just by thinning layers [22].

2.1.3. <u>nBn Structure</u>

nBn type SL photodetectors was introduced by Maimom and Wicks [23]. It was designed in order to decrease Shockley-Read-Hall current so that reduction of dark current and noise can be attained. Thus, photodetectors can reach higher detectivity values at higher operating temperatures. In addition to this, surface passivation is not needed because of the absence of surface leakage currents [23].

As shown in Figure 2.5, a nBn SL detector structure consists of a n- type narrow-band-gap thin contact layer, a 50–100 nm thick wide-band-gap material layer with a large barrier for electrons and no barrier for holes, and a thick n-type narrowband gap absorbing layer. As a result, the majority carrier current between the two electrodes is blocked by the large energy offset, while there is no barrier for photo generated minority carriers. Thus, this device operates as a "minority carrier photoconductor" [24].

nBn structure designed for blocking the majority carrier dark current was applied to MW-LW dual-band superlattice infrared photodetector whose photoresponse band could be selected by the bias polarity. As shown in Figure 2.6, by forward biasing, the band offset in the valence band becomes large, and the diffusion of holes generated in MW SL dominates the photoresponse signal. Under reverse bias, due to enhancement of the conduction band offset and narrowing of the barrier,

holes generated in LW SLS play the major role on photoresponse current even if small amount of electrons activated in MW SL may have a tunneling possibility [25].
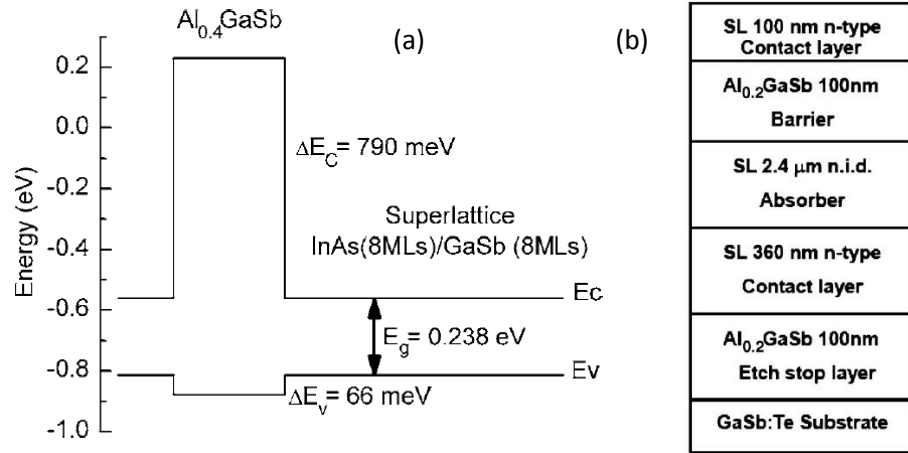
Figure 2.5 (a) Schematic view of nBn structure with calculated offsets [24], (b) Schematic view of heterojunction nBn device [26].

(a) Forward Bias   (b) Reverse Bias
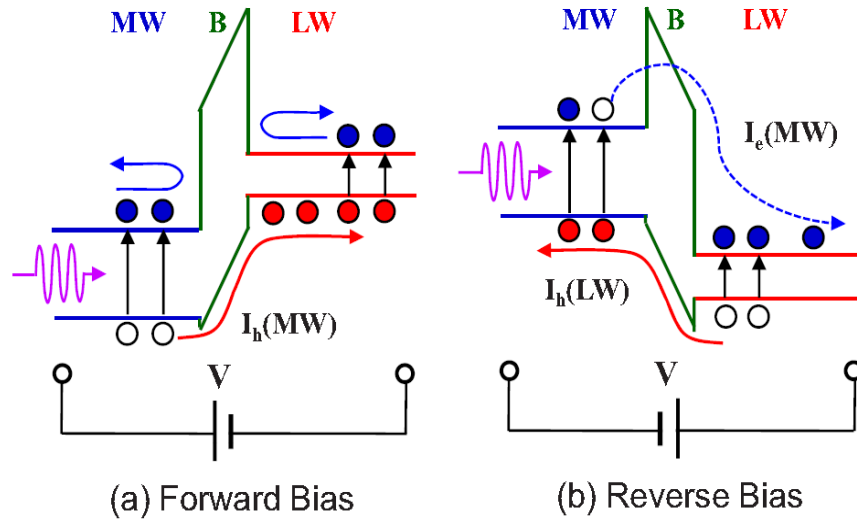
Figure 2.6 Energy band and current flow in dual-band nBn structure under (a) forward and (b) reverse biases [25].

2.1.4. Avalanche Photodiode Superlattice Structure

The first applications of the Avalanche Photodiode Structure in the infrared photodetector systems were on MCT detector systems [27], [28]. In 2007, the first Type-II InAs/GaSb Superlattice Avalanche photodiode was made in the form of p+-n-n junction as seen in Figure 2.7 [29]. In order to create high signals in sensors, high internal gain is desired in the photodiode and Avalanche photodiodes have the highest internal gain. A noiseless Type-II InAs/GaSb Superlattice Avalanche photodiode in MWIR was demonstrated in 2007 [30].
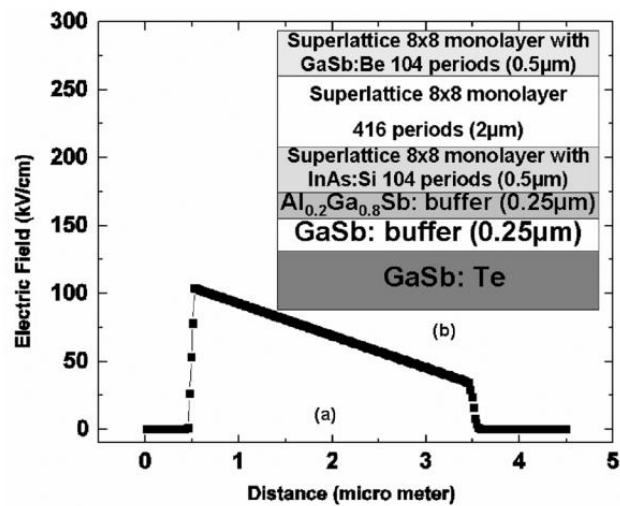
Figure 2.7 (a) Electric field distribution over n- region at the breakdown voltage (20V), (b) Thickness and doping of different layers [29**].**

2.1.5. Two color type II superlattice n-i-p-p-i-n structure photodiodes

The structure of n-i-p-p-i-n SL photodiode is composed of a GaSb layer between two back to back p-i-n SL junctions. Photodiode can be designed for different absorption windows called as blue SL whose cutoff

23

wavelength is shorter, while other junction is called as red SL which has a longer cutoff wavelength. Red SL is grown first because in front side illuminated systems, red SL is wanted to be used as a filter for blue SL [31], [32]. These structures are developed for multi-color FPAs.

2.1.6. "N" Structure for Type-II Superlattice Photodetector

"N" structure type is a new design for Type-II Superlattice detectors proposed by one of our collaborators, Prof. Dr. Yüksel Ergun [33]. The basic modification is introducing a thin layer of AlSb between InAs and GaSb layers as shown in Figure 2.8.
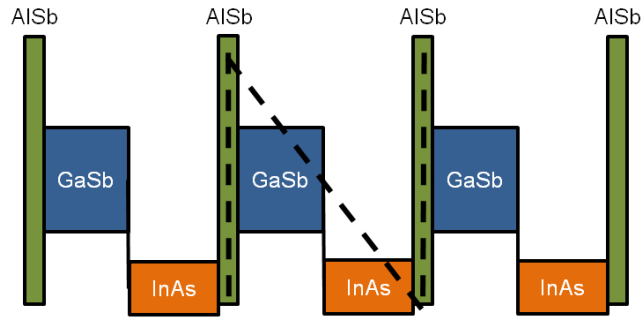
Figure 2.8 Band profiles of "N" structure design [33**].**

AlSb layers acts as electron barriers and electron hole overlap is increased by applying this unipolar barrier to the superlattice system. In reverse bias condition, tilting of the energy band diagram shifts electron and holes wavefunctions. In that case with a symmetrical barrier design, while on one side of the barrier electron-hole overlap increases, on the other side of the barrier it decreases due to the direction of the electric field [33]. However, if the barrier is asymmetrical and in the same

direction of bias, there is an increases in absorption without any loss of overlap. This design also decreases Auger RG process therefore the dark current of the photodiode is expected to be drastically lowered by that design.

Table 2.1 shows some of the best results of MWIR Type-II InAs/GaSb Superlattice single pixel detectors from various research groups.

Table 2.1 Some of the best result of MWIR Type-II InAs/GaSb Superlattice signle pixel detectors.

Reference No	Substrate	p-contact	p-SL layer	i-SL layer	n-SL layer	n-contact	Cut-off	Quantum efficiency/ Responsivity	D* (Jones)
[34]	GaSb:Te	8ML InAs:Be/ 8ML GaSb 4×10^{18} cm^{-3} 20 periods	8ML InAs:Be / 8ML GaSb 1×10^{18} cm^{-3} 30 periods	8ML InAs / 8ML GaSb 260 periods	8ML InAs:Si / 8ML GaSb 1×10^{18} cm^{-3} 30 periods	8ML InAs:Si/ 8ML GaSb 4×10^{18} cm^{-3} 75 periods	4.6 μm	0.9 A/W @77K, 0V	3.5×10^{12}
[35]	GaSb/ AlGaAsSb 500 nm	GaSb:Be 700 nm	9.5 ML InAs / 12ML GaSb:Be 1×10^{17} cm^{-3} 90 periods	9.5 ML InAs / 12 ML GaSb 40 periods	9.5ML InAs:Si / 12ML GaSb 5×10^{17} cm^{-3} 60 periods	InAs:Si 20 nm	5.4 μm	0.7 A/W @ 77K	5.6×10^{12}
[36]	GaSb:Be	GaSb:Be	5.9 ML InAs / 7.2 ML GaSb:Be 80 periods	5.9 ML InAs / 7.2 ML GaSb 200 periods	5.9 ML InAs:Te / 7.2ML GaSb 80 periyot	20nm InAs:Te + 10nm GaSb	3.9 μm @ 250K	22% @78K 25% @300K	4.9×10^{13} @ 78 K 2.4×10^{9} @ 300K
[37]	GaAs n-type	200 nm GaAs / 4 μm GaSb	7ML InAs/ 11ML GaSb 500 nm 1×10^{18} cm^{-3}	7 ML InAs/ 11ML GaSb 2 μm	7ML InAs/ 11ML GaSb 500 nm 1×10^{18} cm^{-3}	10 nm InAs n^{+}	4.08 @77K 4.8 @300 K	36% @ 100K, 3.5 μm	6×10^{11} @ 77K 6×10^{8} @300K
[38]	GaSb undoped	-	9ML InAs/ 10ML GaSb	9ML InAs/ 10ML GaSb	9ML InAs/ 10ML GaSb	10 nm InAs n-doped	5.0 @ 77 K	%25	1.5×10^{13} @ 77 K
[39]	GaSb	7.5/10M InAs/GaSb 1×10^{18} cm^{-3} 500nm	7.5/10MLs InAs/GaSb 3μm 1×10^{17} cm^{-3}	10/1/5/1 MLs of InAs/GaSb /AlSb /GaSb 500 nm M barrier	10/1/5/1 MLs of InAs/GaSb/AlSb /GaSb 1×10^{18} cm^{-3} 500 nm n contact	1.5μm InAsSb n-doped	4.6 μm	%48 @ 110K	7×10^{13}

2.2. Growth of Superlattice by Molecular Beam Epitaxy (MBE)

Molecular Beam Epitaxy invented at Bell Telephone Laboratory in the late 1960's by Alfred Cho is a modern and Ultra High Vacuum (UHV) system for growing single crystal materials on substrates. The atoms and molecules coming from the source of MBE do not react with any other particle before reaching the substrate due to the ultra-high vacuum condition. The substrate is heated up to a point which varies with the crystal desired to be growth. Crystallization reaction between the substrate surface and the particles is occurred via thermal process. The growth rate is generally smaller than 1 atomic monolayer per second and the ability to shutter the beam of particle can be also smaller than one second. Therefore, MBE assures almost atomic level growth control as well as very good control of composition and doping.

MBE systems consist of three main parts; a load lock, a preparation chamber and growth chamber(s).

i)   Load lock is the part used for placing the epi-ready substrate to the vacuum environment for picking up the product after growth. A combination of a mechanical pump and a turbomolecular pump is equipped in order to achieve 10^{-8} Torr pressure in this chamber.

ii)   Preparation chamber is the transition part for substrate from vacuum environment to the growth chamber by using a trolley system. It is also used for storing the substrates and heating the substrate for initial outgassing. The pressure of growth chamber is preferred to be around 10^{-10} Torr therefore an ion pump is used to reach that value.

iii)   Growth chamber is the part of MBE system that growing process is realized. An ion pump, a Helium closed loop cyro-pump and a Titanium sublimation pump are used to achieve UHV level. In the growth chamber, there are numbers of effusion cells which contain required materials that are evaporated during the growth process. Each cell has its own shutter unit to exactly control the rate of growth. The substrate holder is used to

heat and rotate the sample. In the growth chamber, there are also a thermocouple to measure the temperature of substrate, an ion gauge to determine equivalent pressure, a mass spectrometer to monitor residual gas levels, a Reflection High Energy Electron Diffraction (RHEED) gun and fluorescent screen to in situ monitoring of the growth as illustrated in Figure 2.9.
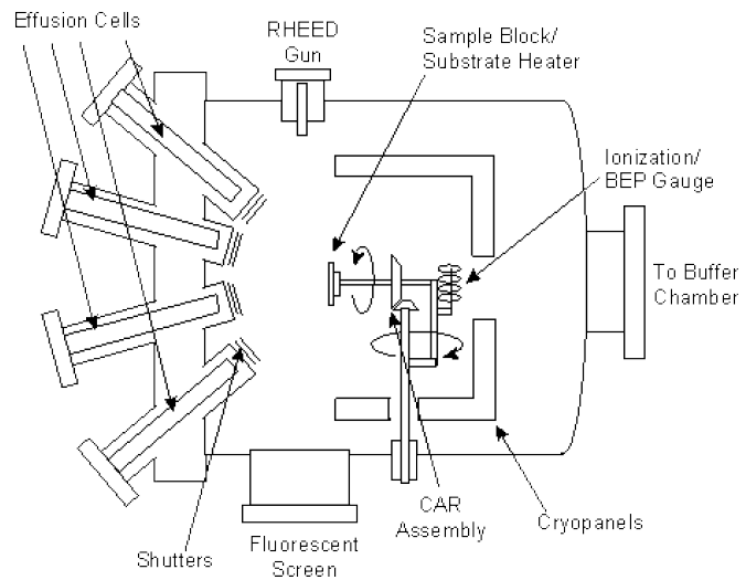
Figure 2.9 Schematic view of MBE Growth Chamber [40**].**

The materials presented in this thesis are grown by IQE Inc. Company on GaSb substrates. The devices are designed as p-i-n photodetectors with a cut-off wavelength around 5 μm, but with different layer periods. The design study was performed by three research groups from Anadolu University, Bilkent University and METU. We have mainly 3 different wafers in total and named them as SL2, SL3 and SL4. The additional sample studied here is the sample called as SLN which the one called "N" structure superlattice photodetector and

described above. In this study, samples fabricated from SL2, SL4 and SLN wafers were used only to observe the electrical and optical effects of different layer periods. Samples fabricated from SL3 wafer were also used to compare to passivation effects and noise analysis.

Structures are based on 60-periods n-type/40-periods a non- intentionally doped (n. i. d.) active region/90-periods p-type for SL2 sample, 60-periods n-type/60-periods a non- intentionally doped (n. i. d.) active region/90-periods p-type for SL3 sample (Figure 2.10) and 60-periods n-type/40-periods a non-intentionally doped (n. i. d.) active region/140-periods p-type InAs/GaSb SL for SL4 sample. Each period in the entire and all structure consists of 2.85 nm InAs and 3.3 nm GaSb layers with InSb-like interfaces. GaSb layers in the p-type superlattice period were doped with Be to a level of 1.5×10^{17} cm^{-3} while the InAs layers were doped with Te to a level of 5×10^{17} cm^{-3}. The entire SL structures were enclosed by a 20 nm n-type InAs: Te (5×10^{17} cm^{-3}) top and a 1μm thick p-type GaSb: Be (1×10^{17} cm^{-3}) bottom contact layers.

The "N" structure photodetector is also designed as p-i-n photodetector. It begins with 100 nm thick GaSb buffer layer and as an insulator and etch stop layer, 20 nm Al$_{(x)}$GaAs$_{(y)}$Sb, followed by 1000 nm GaSb:Be (p=1.0x10^{17} cm $^{-3}$) p contact layer. P-i-n part of the design consist of 90 periods 9 monolayers (MLs) of InAs/2 MLs of AlSb/8.5 MLs of GaSb:Be (p=1.5x10^{17} cm^{-3}) p-type layers, 60 periods 9 MLs of InAs/2 MLs of AlSb/8.5 MLs of GaSb i-layers, 40 periods 9 MLs of InAs:Te (n: 5x10^{17} cm $^{-3}$)/ 2 MLs of AlSb/8.5 MLs of GaSb n-type layers and structure is terminated by 20 nm InAs:Te (n: 5x10^{17} cm $^{-3}$) cap layer to assure good ohmic contact.

Appropriate shutter sequences and InSb like interfaces were applied to compensate the tensile strain caused by lattice mismatch between InAs and GaSb layers.

Layer	Type	Material	Group	Repeat	Thickness (A)	Dopant	CV Level
16	N	InAs			200	Te	5.0E17
15	i	GaSb	3	60	33		
14	i	InSb	3	60	1 ML		
13	N	InAs	3	60	28.5	Te	5.0E17
12	i	InSb	3	60	1 ML		
11	i	GaSb	2	60	33		
10	i	InSb	2	60	1 ML		
9	i	InAs	2	60	28.5		
8	i	InSb	2	60	1 ML		
7	P	GaSb	1	90	33	Be	1.5E17
6	i	InSb	1	90	1 ML		
5	i	InAs	1	90	28.5		
4	i	InSb	1	90	1 ML		
3	P	GaSb			10000	Be	1.0E17
2	i	$Al_{0.93}GaAs_{0.07}Sb$			200		
1	i	GaSb			1000		
SUBSTRATE							

Figure 2.10 Superlattice Structure of SL3 Sample.

2.3. Device Fabrication and Passivation

In order to characterize superlattice photodetector at single pixel level, the wafer grown by MBE has to be fabricated. The fabrication and passivation process of the devices used in this study were realized at Bilkent University, Advanced Research Laboratory. There are four main steps in fabrication process: cleaning, masking, etching and metallization, respectively.

For the first step, 1x1 cm^2 sample cut from the wafer is cleaned in order to decontaminate from physical and chemical dirt. Cleaning process begins with spraying ultra-pure nitrogen gas onto sample for mechanical cleaning and continues with submerging the sample for 5 minutes into acetone, methanol, isopropanol (IPA), de-ionized water respectively. Then ultra-pure nitrogen gas is applied again and in order to get rid of from the water molecules onto the surface, sample is heated up to 120°C within dehydration bake.

After cleaning process is completed, fabrication is proceeded with the masking steps. First, positive photoresist is coated on the sample with 4000rpm spinner speed for 50 seconds and then baked. The coated sample is exposed on the mask aligner and baked again. Subsequently, the sample is dipped into (1:4) (AZ400K:H$_2$O) solution to remove the undesired area. Finally, sample is rinsed in distillated water and dried with nitrogen gas.

Etching process is needed in order to form single pixels. The minimum etching depths to reach the p-contact level are 1330nm, 1450nm and 1655nm for SL2, SL3 and SL4 samples respectively. Before the etching, photoresist thickness is measured by surface profiler to determine the reference point of etching. It is also crucial to know the etching rate of the solution for the sample in order to determine the etch time. Etching process begins with inserting the sample into a phosphoric acid and hydrogen peroxide solution prepared with 20:1 rate. The samples' surface should be parallel to the surface of the solution during the dipping process to prevent any nonuniformity. After the etching is completed, the photoresist on the sample is cleaned by acetone. At the end, the cleaning process described before is repeated to proceed to metallization process.

Metallization is the last step of fabrication process. For metallization, lift-off process is applied as follows: photoresist is applied to the surface and processed with a mask so as to open windows on the region where the metal layers will be placed. The alignment can be adjusted by using alignments marker on the masks as seen in Figure 2.11.
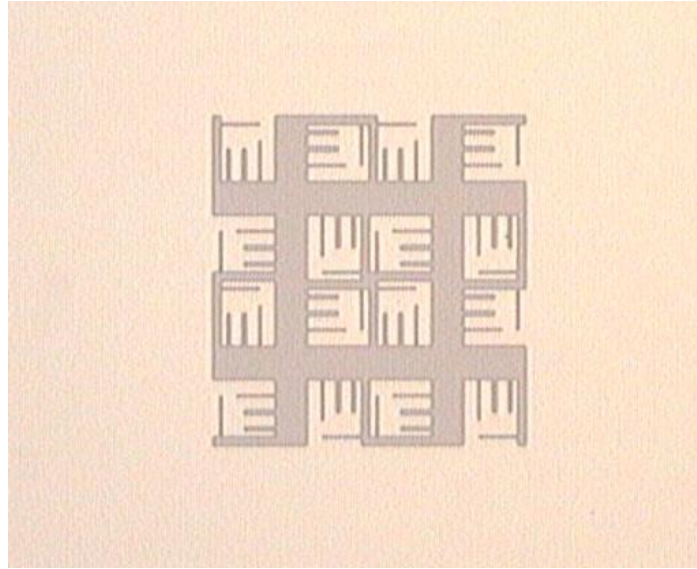
Figure 2.11 Mask Aligner Marker.

After the photoresist development, the metallization process is realized under vacuum environment. 20nm Ti and 300nm Au is then evaporated and applied to the sample. At the end, for lift-off, the sample is soaked in the acetone.

In this study, the mask has 3 different sizes as 400x400 μm^2, 500x500 μm^2 and 600x600 μm^2. Figure 2.12 shows the middle of 4 pieces of 400x400 μm^2 size pixels. The yellow areas as seen like a plus in the middle and as seen like elbows near the corners are Ti/Au metal coated area on the p-type and n-type contacts of the wafer respectively. Dark grey areas indicate the surface of the pixels and light grey areas are the etched regions.

The fabrication process is completed after bonding of the contacts (Figure 2.13) to the pin pads of Dual In-line Package (DIP) by wire bonder if any passivation will not be applied to the pixels.
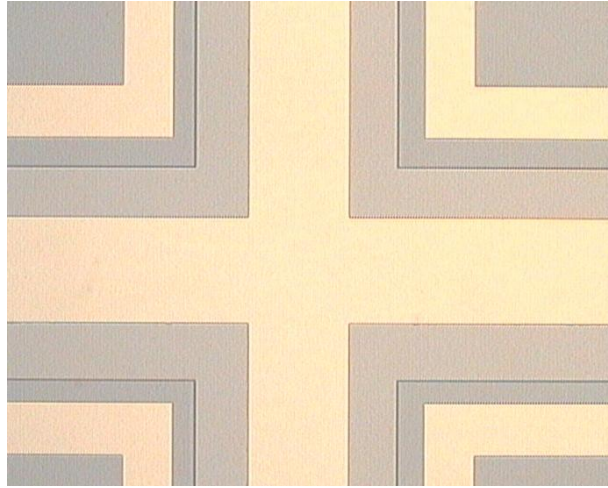
Figure 2.12 Microscopy image after fabrication.

a) Test mesa pattern array after fabricated for different sizes

b) SL device structure (**produced by MBE**) with deposited Ti/Au top and bottom contacts

20 nm InAs:Te n-contact
60 x InAs:Te/GaSb p-type
60 x InAs/GaSb n.i.d.
90 x InAs/GaSb:Be p-type
1000 nm GaSb:Be p-contact
20 nm AlGaAsSb buffer layer
100 nm (100) GaSb Substrate
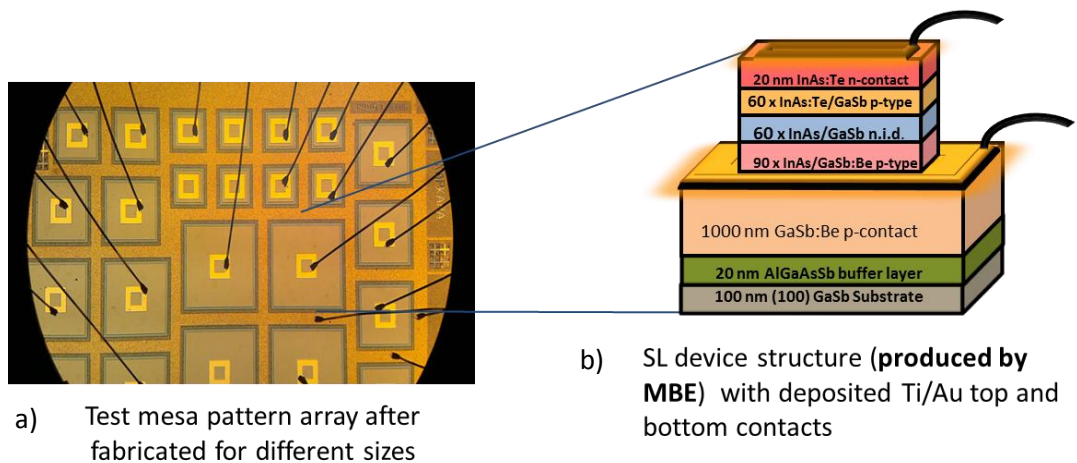
Figure 2.13 Mesa pattern and bonding after fabrication.

In this study, we used three samples of SL3 wafer in regards of passivation; Si_3N_4 passivated sample, SiO_2 passivated sample and an unpassivated sample to compare the passivation effects.

Passivation of photodetector devices is one of the most crucial steps for a good diode production. The existence of surface states at the crystal surface due to

33

abrupt termination of semiconductor surface and native oxides on the SL detector surfaces leads to leakage current that can limit/degrade the SL infrared detector performance. This might lead to a favorable surface potential for easy carrier transport on the surface [41]. Hence, without proper surface passivation, the leakage current may be significant particularly on the mesa side-walls. This is of great importance, especially where the detector area approaches the sizes needed for focal-plane-array applications. Consequently, intentional passivation is needed for mesa etched detectors to suppress the leakage current by minimizing/eliminating the surface states and hence the influence of foreign materials [42].

In this study, for the passivation of SL3 and SLN samples, Plasma Enhanced Chemical Vapor Deposition (PECVD) technique is used to deposit the passivation materials, Si_3N_4 or SiO_2. PECVD is a regular passivation technique and SiO_2 is the most used passivation material for type-II superlattice devices. Thickness of the passivation is around 300nm for each material. PECVD system should be vacuumed before the deposition and temperature of the sample holder is heated up to 250°C. For SiO_2 passivation, SiH_4 and N_2O gases and for Si_3N_4 passivation, SiH_4 and NH_3 gases flow through the PECVD system. In order to create plasma of the reacting gases, RF (AC) source is used with 10W power output. After the passivation layer is deposited, the whole sample is coated by the passivation. A passivation mask is used to lift-off the passivation layer from undesired regions, i.e. metal deposited area. The sample is then soaked into hydrofluoric acid solution, cleaned with distilled water and nitrogen gas. Finally, the sample is ready for bonding and characterization.

SL3 sample is also passivated using another method that is applied first time for type-II superlattice photodiodes by one of our collaborators, Dr. Ömer Salihoğlu [43]. Atomic layer deposited (ALD) Al_2O_3 passivation layer is proposed to use as an alternative to PECVD deposited SiO_2 which needs high growth temperature and might be destructive due to creating high density energetic plasma with RF source. ALD is based on consecutive gas phase reactions. In the growth

chamber, two gases are introduced one at a time. The first reacts on the surface and then absorbed in the previous sequence. Due to the fact that thickness of the passivation layer depends on the number of reaction cycles, ALD process offers control of thickness at molecular level. This is also an advantage when deposited passivation to sharp edges. Al_2O_3 works pretty well as a passivation material over a very wide range of frequency. In order to grow 20nm Al_2O_3, 200 cycles deposition carried out in ALD with 150 ºC substrate holder temperature. Growth of Al_2O_3 has been done by delivering 0.015 s water vapor and 0.015 s trimethylaluminum (TMA) pulses into the chamber in a sequential manner under constant 20 sccm N_2 gas flow. A wait time of 20 s was added after each pulse to ensure surface reactions to take place.

CHAPTER 3

EXPERIMENTAL METHODS

This chapter describes electrical, optical and noise characterization techniques. All of the experimental works were done in METU, Department of Physics, Semiconductor Device and Material Characterization Lab.

3.1. Introduction of Measurement System

In the experiments, an open system liquid nitrogen cryostat system pumped with a mechanical pump up to 10^{-3} Torr is used to decrease the sample temperature below 80K. The cryostat has two ports with 19 pins out, Port A is connected to the temperature controller unit while Port B is connected to a key box. The keys located in the box have three option, they can be connected to red output, black output or no output, when switched to up position, down position or middle position, respectively. The pins on the Port B are connected with the cables inside of the cryostat in order to establish connections with the sample DIP. A photo of a DIP with sample can be seen in Figure 3.1.

As mentioned in the previous chapter, at the end of the fabrication process, pixels are connected to the pads of DIP which have numbers from 1 to 40. A table of connection is filled as which pin is connected to which pixel. Black sockets those have letters A to H and J to S on them is used to connect the DIP to the Port B. Port B and key box have also these letters and all same letters are

connected to each other. Figure 3.2 shows that the connections inside of the cryostat and the between pixels and key box.
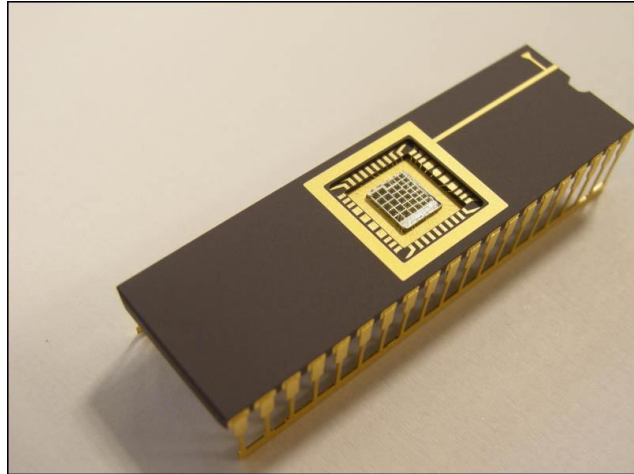
Figure 3.1 DIP with sample after fabrication.

Two temperature sensors are employed, one of them is on the cold head of the cryostat and the other is on the sample holder. In order to minimize temperature difference between two sensors, thermal paste is used between sample holder and DIP. Still, in general there is approximately 1.4K difference.

3.1. Figures of Merit for Infrared Detectors

To be able to compare the relative performances of different type of infrared detectors, fundamental figures of merit should be discussed. As a general definition, a detector coverts incoming signal into another type of signal that can be analyzed. The relationship of these input and output signal from different aspects is investigated in this section.
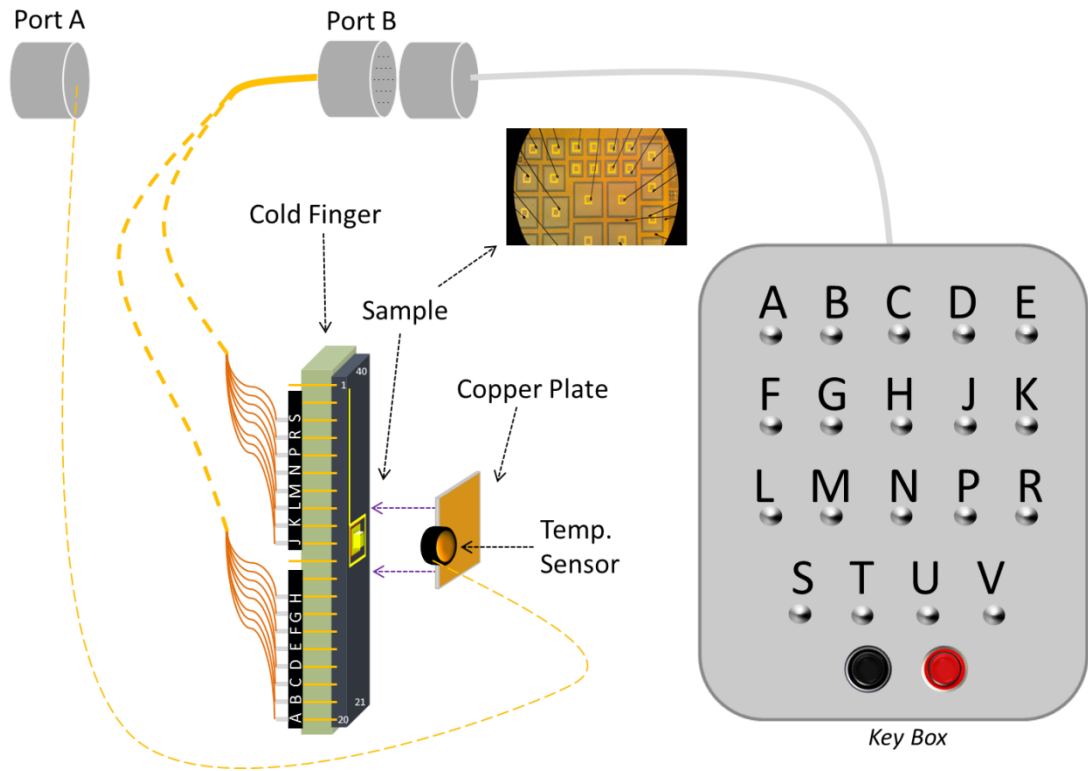
Figure 3.2 Connection schema inside the cryostat.

3.1.1. Responsivity (R)

The most direct relationship between incoming and output signal is responsivity, the ratio between the output signals, in our case this is always electrical – either a current or a voltage, and incoming signal which is radiant input. In other word, responsivity indicates that how much electrical signal is produced in response to unit radiation power received by the detector.

$$Responsivity\ (R) = \frac{Signal\ Output}{E \cdot A_d} \left[\frac{A}{W}\right] or \left[\frac{V}{W}\right] \quad (3.1.1.1)$$

where E is called incidence, the flux density at the detector (W/cm^2) and A$_d$ is the area of the detector (cm^2).

Responsivity can be shown in terms of Quantum Efficiency (η):

$$R = \frac{\eta \cdot q}{h \cdot v} \left[\frac{A}{W}\right] or \left[\frac{V}{W}\right] \qquad (3.1.1.2)$$

where q is the electron charge, *hv* is the energy of incident photons and η is (external) quantum efficiency of detector which is the number of carriers obtained at the output of the detector per number of incident photons per unit time.

Responsivity is an important parameter for a detector due to the fact that it tells to the circuit designers how much amplifier gain they need to get for a satisfactory signal level.

Although, A/W and V/W are the most common units of responsivity, while the output signal type does not change, the input may change to total power, power density, photon arrival rate or photon flux density, depending on the application.

For an ideal photon detector, current responsivity with respect to wavelength for different quantum efficiency values is shown in Figure 3.3.

3.1.1. Noise Equivalent Power (NEP)

Detectors are able to convert any incoming photons into electrical signal although it does not mean that device will be able to sense this signal. If

the detected signal is lower than the intrinsic noise of the detector or the system, that signal is lost in the noise and detection process fails.
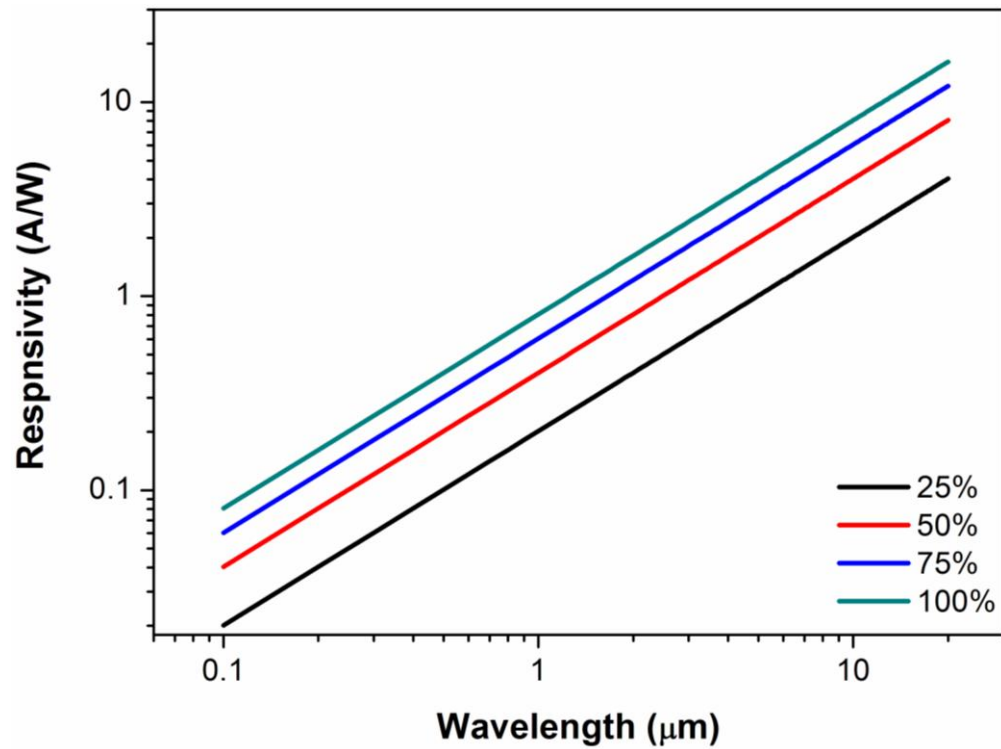
Figure 3.3 Responsivity of ideal photon detector with different quantum efficiencies.

To compare the ultimate sensitivities of different detectors, Noise Equivalent Power (NEP) is defined as the amount of radiation flux needed to produce an output signal equal to the root mean square (rms) of the noise signal of detector. In other words, NEP determines minimum detectable radiation power required to establish a signal. Therefore, the smaller NEP means the more sensitive detector.

$$NEP = \frac{v_{noise}}{R_v} = \frac{i_{noise}}{R_i} = \frac{\Phi}{i_{signal}/i_{noise}} \ [W] \qquad (3.1.2.1)$$

3.1.2. Specific Detectivity (D*)

Detectivity is the inverse of NEP value. NEP is a good performance parameter though it is still dependent on the active area of the detector and signal bandwidth. If we don't have any information about detector size and bandwidth, we cannot conclude whether NEP of detector is acceptable or not. Therefore, we need to define another parameter, specific detectivity (D*), for comparison of different detectors.

$$D^* = \frac{\sqrt{A_d \cdot \Delta f}}{NEP} = \frac{\sqrt{A_d \cdot \Delta f}}{\Phi} \cdot \frac{i_{signal}}{i_{noise}} = R_i \cdot \frac{\sqrt{A_d \cdot \Delta f}}{i_{noise}} \left[\frac{cm \cdot \sqrt{Hz}}{W}\right] (3.1.3.1)$$

where A_d is active area of detector, Δf is signal bandwidth, R_i responsivity in term of current, and i_{noise} is noise current. Of course, voltage terms R_v and v_{noise} can be used instead of current terms. Unit of D* is called as Jones.

Thus, specific detectivity can be defined as signal-to-noise ratio of a detector when 1W of radiant power is received by a detector with an area of 1 cm^2 and bandwidth of 1 Hz. Higher D* values indicates better performance of detectors for sure.

3.2. Optical Measurements

In this study, optical characterizations to obtain responsivity and quantum efficiency values of single pixel detectors have two main steps. First of all, spectral measurements of single pixels are conducted using FTIR instrument and then peak responsivity measurements are carried out using a calibrated blackbody source. Response time of the photodetectors is also investigated.

3.2.1. Spectral Measurement

In spectral measurements, FTIR Bruker Equinox 55 instrument, SRS 560 voltage preamplifier and cryostat system with key box are used as shown in Figure 3.4. Data collection and FTIR control are provided via OPUS software.

After reaching below 79K temperature limit, experiment proceeds with background data collection. While in regular FTIR measurements, background data is gathered from a reference sample, in device measurements, we obtain the background data using an empty sample slot of FTIR. This means, air transmission of IR radiation is used as background radiation. A Deuterated Triglycine Sulfate (DTGS) detector which has an ideal flat responsivity curve is employed for sensing the IR radiation for background. After collecting background transmission, cryostat is placed into the sample slot.

Port B is connected to the key box, and key box is connected to the preamplifier. External A input of FTIR is connected to the preamplifier to get the signal from sample. In order to obtain the spectral response of the single pixel detector, one of the keys which is connected to n-side of the device is switched to down and one of the keys which is connected to p-side of the device is switched to up.
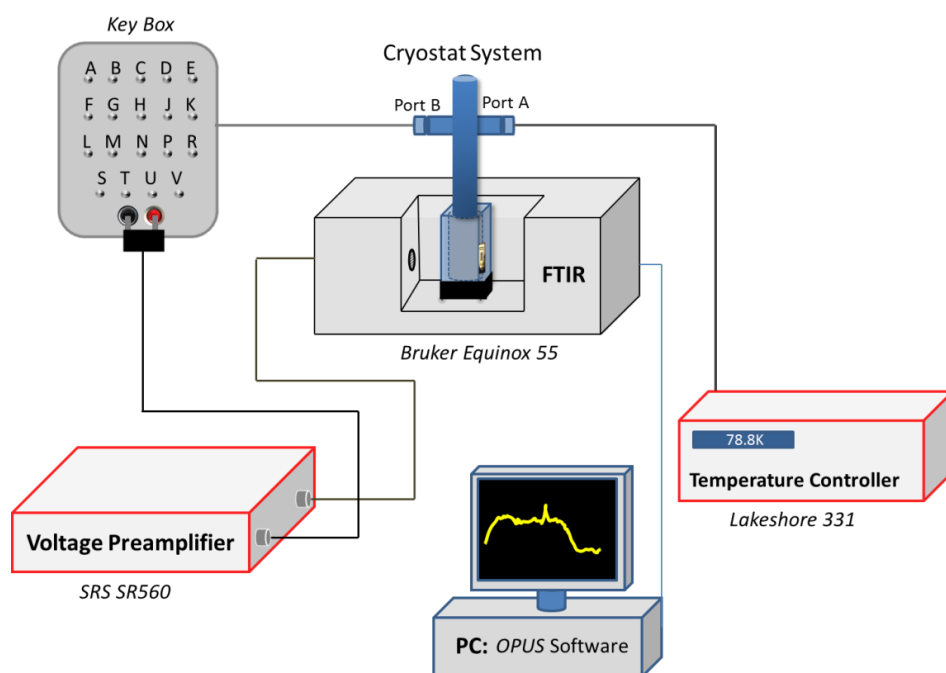
Figure 3.4 Spectral Measurement Setup.
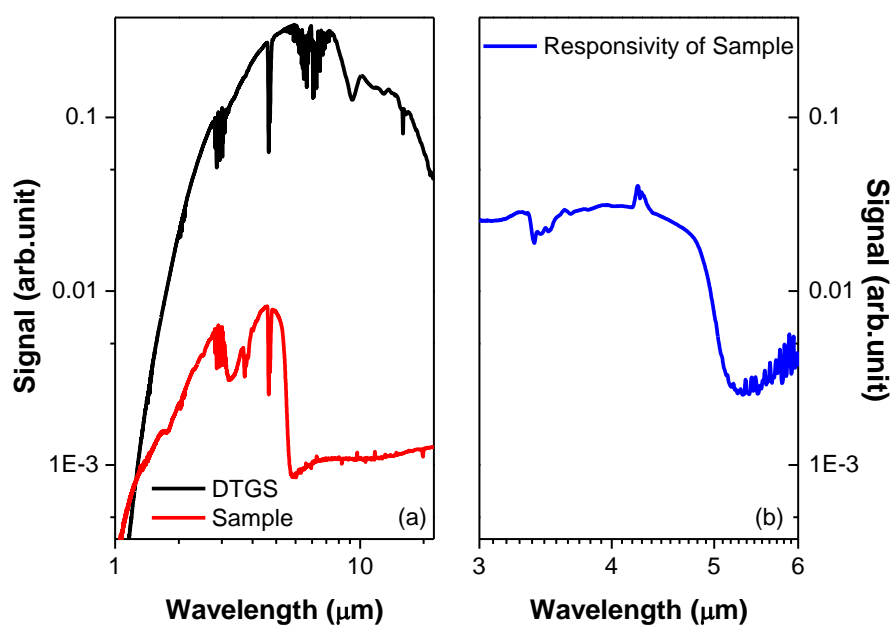
Figure 3.5 (a) Transmission of air detected by DTGS detector, single pixel detector and (b) responsivity curve of sample.

The result given in Figure 3.5 is the ratio of transmission of air detected by single pixel to the transmission of air detected by DTGS detector.

3.3.2. Peak Responsivity Measurement

After completing the measurement of responsivity curve of the sample pixel, peak responsivity measurement should be done in order to obtain the value of responsivity at the y-axis of the graph. A calibrated blackbody source, a lock-in amplifier and a chopper are employed for this measurement. In order to obtain responsivity value as A/W unit, a current preamplifier is also employed. The temperature of blackbody source is adjusted to 450°C because the peak wavelength of a blackbody source at that degree is at 4µm, at the middle of MWIR window.
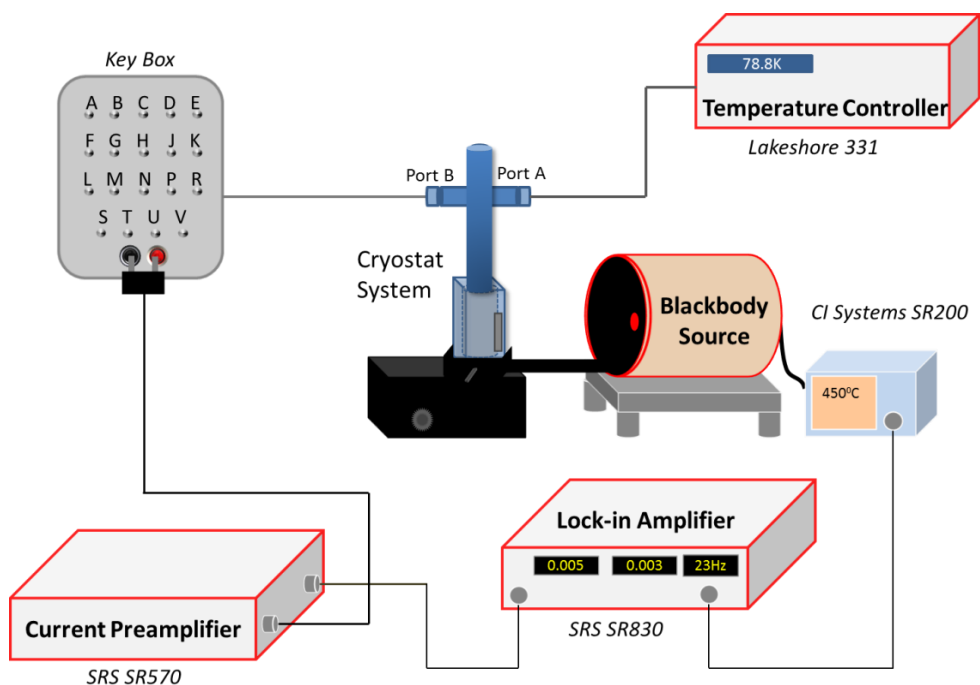
Figure 3.6 Peak Responsivity Setup.

The cryostat with sample is placed onto X-Y-Z platform in front of the blackbody source with a distance around 20cm and all the radiation emitted from blackbody is sensed by single pixel photodiode.

The blackbody source is not the only infrared source in the experiment environment. Therefore, to eliminate the effects of infrared radiation sources other than the blackbody source, a chopper is used in front of the aperture of blackbody. It chops the signal only emitted from blackbody and by introducing the chopper frequency as a reference to lock-in amplifier, the amplifier detects only chopped signal. Other required parameters are adjusted in the lock-in amplifier for stable and accurate measurement. Schematics of the peak responsivity measurement can be seen in Figure 3.6.

The only measured parameter required to calculate peak responsivity of single pixel is the voltage value measured by lock-in amplifier. Due to the fact that all emitted wavelengths from blackbody are sent to the pixel, calculations given below are needed to obtain peak responsivity value [44], [45]. All the calculations are done via responsivity VI (Virtual Instruments) written by LabVIEW software as shown in Appendix A.

$$R = k \times R_{BB} \tag{3.3.2.1}$$

$$k = \frac{\sigma T_{BB}^4}{\int_{\lambda_1}^{\lambda_2} M(\lambda)_{T_{BB}} \times S(\lambda) d\lambda} \tag{3.3.2.2}$$

$$R_{BB} = \frac{V_{SL} \times s}{\dfrac{D_{BB}{}^2 \times A_D}{4r^2} \times \left(\int\limits_{\lambda_1}^{\lambda_2} M(\lambda)_{T_{BB}} d\lambda \right) \times T_P \times M_F} \qquad (3.3.2.3)$$

$$M(\lambda)_T = \frac{2\pi h c^2}{\lambda^5 \times (e^{(hc/\lambda k_B T)} - 1)} \qquad (3.3.2.4)$$

where, R is peak responsivity, R_{BB} is blackbody responsivity, $M(\lambda)_{T_{BB}}$ blackbody spectra for a given blackbody temperature, k is blackbody-to-peak conversion factor, σ is Stefan-Boltzmann constant, T_{BB} is the temperature of blackbody, $S(\lambda)$ is the normalized form of signal obtained from FTIR, V_{SL} is the voltage value observed in the peak responsivity measurement, s is the sensitivity value of preamplifier, D_{BB} is the aperture size of blackbody, A_D is the optically active area size of the pixel, T_P is the transmission ratio of cryostat window, M_F is the modulation factor of chopper, h is Planck constant, c is the speed of light, k_B is Boltzmann constant and λ is wavelength.

The definition of blackbody responsivity is the signal measured at the output of the system per power of blackbody incidence, i.e. how much ampere is read from lock-in amplifier for 1 Watt of blackbody power. In order to determine blackbody responsivity, one needs to calculate the flux falling on the detector by using solid angle between single pixel and blackbody aperture. To eliminate the absorption of Thallium Bromo-iodide (KRS-5) window, transmission ratio of the window (80%) is included as a parameter. Due to the fact that the voltage value obtained from lock-in amplifier is a root-mean-square value of the measurement, the power term of the blackbody responsivity equation has to be also rms value. Therefore, modulation factor is taken from modulation factor

table, Ref. [**46**], which varies with the aperture diameter, tooth width of aperture and number of tooth-slot pairs of aperture.

In order to determine peak responsivity value, we should have the information about how much the single pixel responsivity curve close to the blackbody spectra curve, Fig 3.7. It is because the amount of radiation that can be detected has to be known. This ratio is called as blackbody-to-peak conversion factor. The signal obtained from spectral response measurement has to be normalized before multiplication with blackbody emittance and taking the integral over all the wavelengths. The integral of blackbody emittance curve also has to be taken and then divided to the previous integral result.
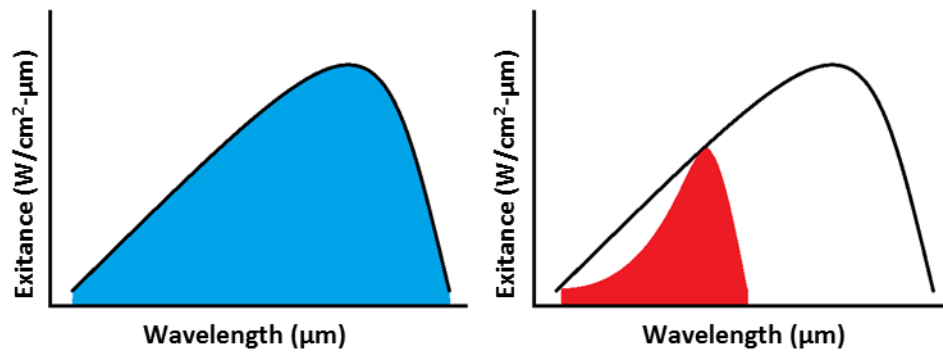
Figure 3.7 Blackbody emittance (blue) and comparison with pixel response (red).

In the final step blackbody responsivity value is multiplied with the blackbody-to-peak conversion factor, hence peak responsivity value is obtained. The peak responsivity value is then multiplied by the normalized responsivity spectra to determine the responsivity graph of single pixel.

3.3.3. Response Time Measurement

Response time measurement is independent from responsivity measurements. The aim of response time measurement is to obtain how fast the pixel response to the incidence of radiation. The ultimate goal of all detector researches is to develop Focal Plane Array (FPA) cameras in order to create images. Speed of the camera, i.e. frame per second (fps), can be very crucial for some field applications. The response time measurement of a single pixel photodetector provides us with the knowledge about the speed of the pixel.

The response time of a detector is usually defined as the time required for a signal to reach value equal to 0.632 of its maximum steady state value [47]. The equations in response time (τ) in time and frequency domains are given below [48].

$$R(t) = R(t = \infty) \left(1 - e^{-t/\tau} \right) \tag{3.3.3.1}$$

$$R(f) = \frac{R_0}{\sqrt{1 + (2\pi f \tau)^2}} \tag{3.3.3.2}$$

Schematic view of response time measurement setup is given in Figure 3.8. The measurement is realized in 10mW rms incidence of blackbody source at 100Hz. In order to reach that power, temperature of blackbody source is set to 390°C, chopper is set to 100Hz and the aperture is adjusted to 1.6mm. The key box is connected to the voltage amplifier and it is connected to a spectrum analyzer. Spectrum analyzer is switched to time scale from frequency scale. If the signal is too noisy, it can be improved by applying low pass and high pass filters in the preamplifier.
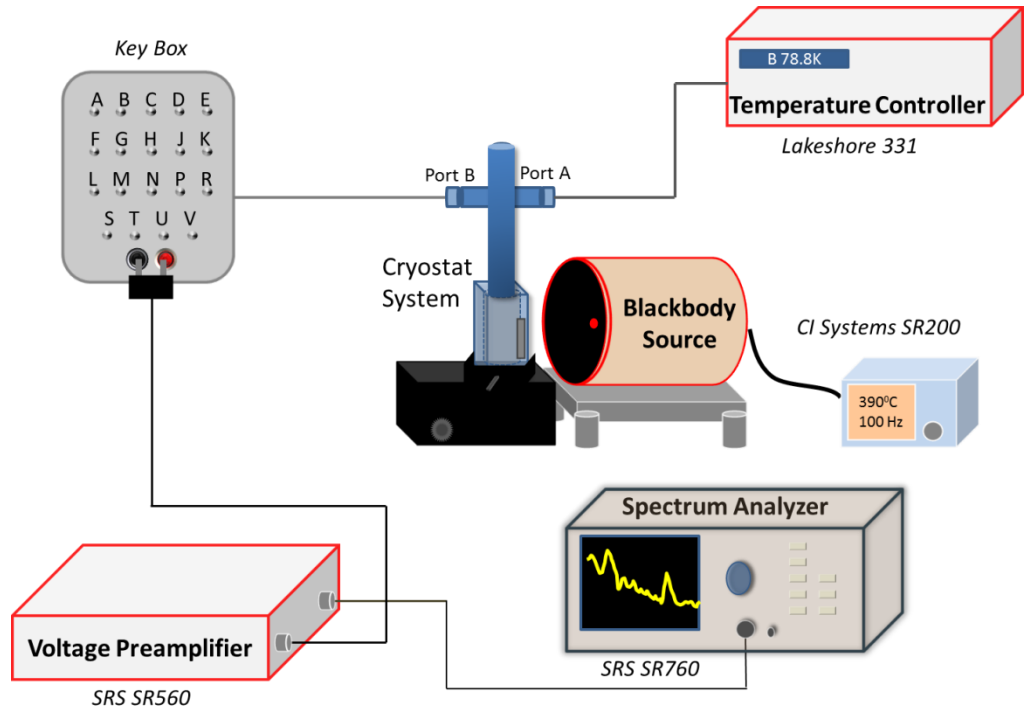
Figure 3.8 Response Time Setup.

3.4. Electrical Measurements

In this study, electrical measurements include dark current vs. voltage (I-V) measurements and dark current noise measurements. I-V measurements are also conducted for different temperatures.

3.4.1. Dark Current vs. Voltage (I-V) Measurements

Dark I-V measurements are vital in order to obtain knowledge on the quality of the device. From these measurements, one can see whether the photovoltaic single pixel is ohmic or rectifying. Zero bias resistance value (R_0) is one most important parameter to compare different passivation on the device surface. We are also interested in the reverse bias regime as FPA cameras operate at a small reverse bias. Therefore dynamic impedance (RA) values are also investigated.

In dark I-V measurements, a copper plate is placed in front of the sample. This is crucial due to the fact that the sample has to look to an object with same temperature as itself in order to reach dark condition. A picoampere meter is employed to apply the bias and read the current, Figure 3.9. Picoammeter is controlled by a computer with SL I-V.vi (see Appendix A) via GPIB port.
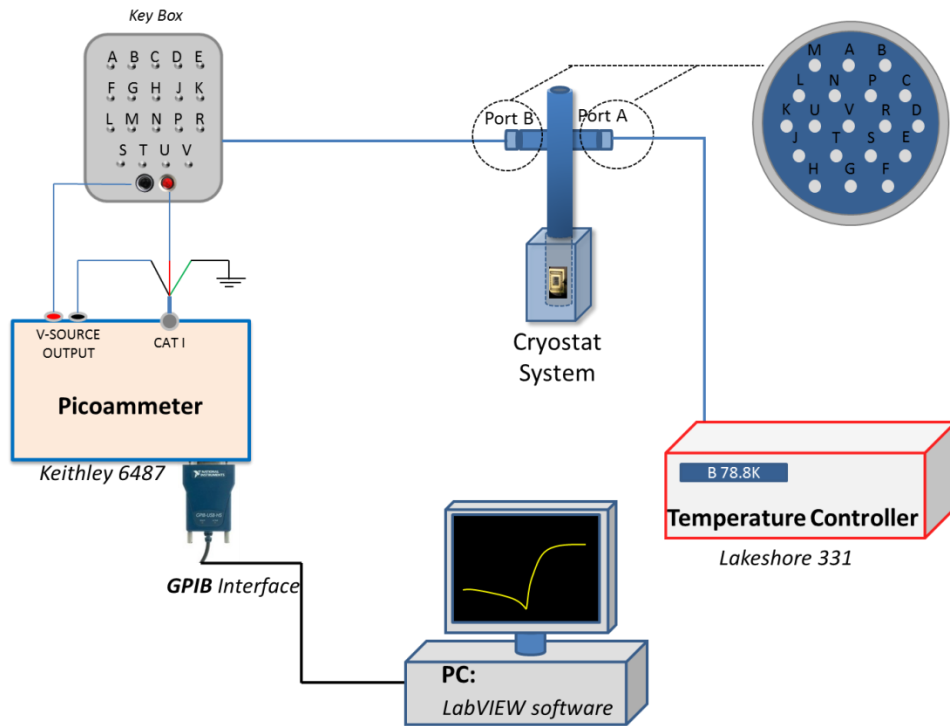
Figure 3.9 Dark I-V Setup.

Equation 3.4.1.1 is solved for the I-V curve to calculate R_0A value of the measured pixel [46]. In our measurements, the difference of two applied bias (voltage step) voltages is 25mV. Therefore, the current values of -25mV and +25mV bias voltages are measured and put them into the equation. R_0 is then multiplied with the area of the single pixel to avoid

from the effects of the different size of pixel area. RA values are also calculated with the same manner.

$$R_0 A = \left(\frac{dV}{dI}\right)_{V=0} \times A = \frac{0.01 - (-0.01)}{I_{V=0.01} - I_{V=-0.01}} \times A \qquad (3.4.1.1)$$

3.4.2. Temperature Dependent I-V Measurement

Temperature dependent I-V measurement is a very effective technique when dominated current mechanisms at different ranges of temperatures of a device are to be investigated. In this study, a closed loop helium refrigeration system is employed to reach temperatures below 77K. Dark current vs. voltage characteristics of pixels are measured at the temperature interval of 250K – 10K with approximately 5K temperature steps. At very low temperatures where dark current is also very low, there might be some undesired problems caused by the refrigeration system, i.e. recycling of refrigerant gas and vacuum pump may generate vibration. As a consequence, there might be flaw on the current measured. Accordingly, to avoid from this possible error, before starting the measurements, the system temperature is lowered to below 10K. Then all the mechanical and electrical units are turned off. The measurements are started at 10K however, at that low temperatures, system temperature raises rapidly, i.e. 3K per minute. The rate of warming decreased with increasing system temperature. After 35K, it is around 2K per minute and after 45K it slows down up to 1K per minute. Since we are interested in the temperature range between 250-50K, this strategy works properly.

The warming rate is totally dependent how well the system vacuum is sealed. In order to accommodate warming rate, the voltage steps in the I-V measurements are increased from 25mV to 50mV. By doing this

adjustment, the time required for one measurement drops down to 30 seconds which means an acceptable rate of maximum 0.5K for a measurement. The setup can be seen in Figure 3.10.

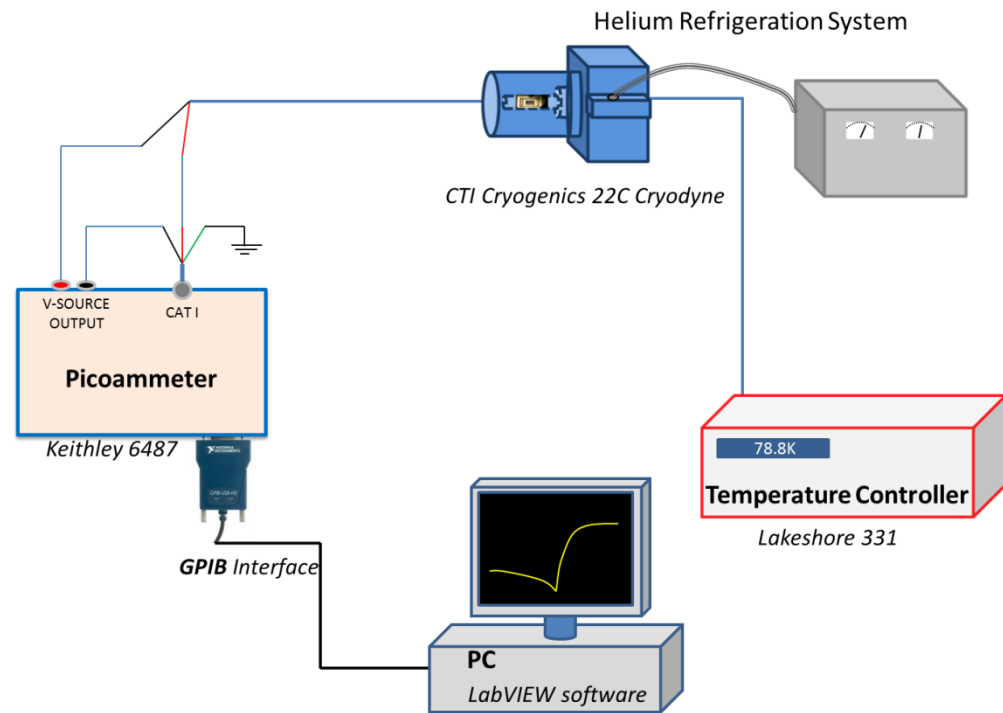**Figure 3.10 Temperature dependent I-V measurement setup.**

In temperature dependent I-V measurements, the same pico-ampere meter is employed with the same connection schema. The key box is not compatible with this cryostat therefore it is not used in these measurements. The pixels are selected before the measurement by comparing the results of the dark I-V measurements done before at below 79K.

3.4.3. Dark Current Noise Measurement

Dark current noise measurement is not a very common characterization tool even though dark current noise of a detector is very crucial. There are two main reasons for the lack of common interest: the dark current/voltage noise of a detector can be calculated from dark I-V measurement, and noise measurement is not straight forward and is a very sensitive measurement. It is therefore hard to measure due to the fact that there are lots of external noise sources in a lab environment.

The most essential modification on measurement setup for a noise measurement is necessity of a Faraday cage made of a metal box. It blocks all external electromagnetic waves and noise sources. Ground connections of all the instruments employed in this setup are connected to the inside of the cage and outside of the cage is connected to the ground of power outlet which literally head to the ground with a copper rod.

Beside the cryostat, the dark current noise measurement setup contains a current preamplifier and a spectrum analyzer in order to obtain frequency spectra. The key box is not used in this experiment because it may create additional noise. The cryostat is employed without its mechanical vacuum pump in order to avoid vibration. This type of small and open system cryostats have the advantage of mobility without warming up. After closing the valve and turning off the pump, the sample stays at the temperature around 79K with a full of liquid nitrogen reservoir for 45 minutes. By adding liquid nitrogen in every 30 minutes, it can be extended up to 3 hours.

Dark current noise characteristics of photodiode pixels are studied in two ways: frequency spectra at specific bias voltages and bias voltage relationship at specific frequencies. The current preamplifier has its own

battery for using it without any power outlet connection. And it also provides an adjustable DC bias voltage that can apply external bias to the sample. The spectrum analyzer needs power outlet connection therefore, in order to prevent its effects from cryostat and preamplifier; it is placed in another division inside the Faraday cage as can been seen in Figure 3.11.
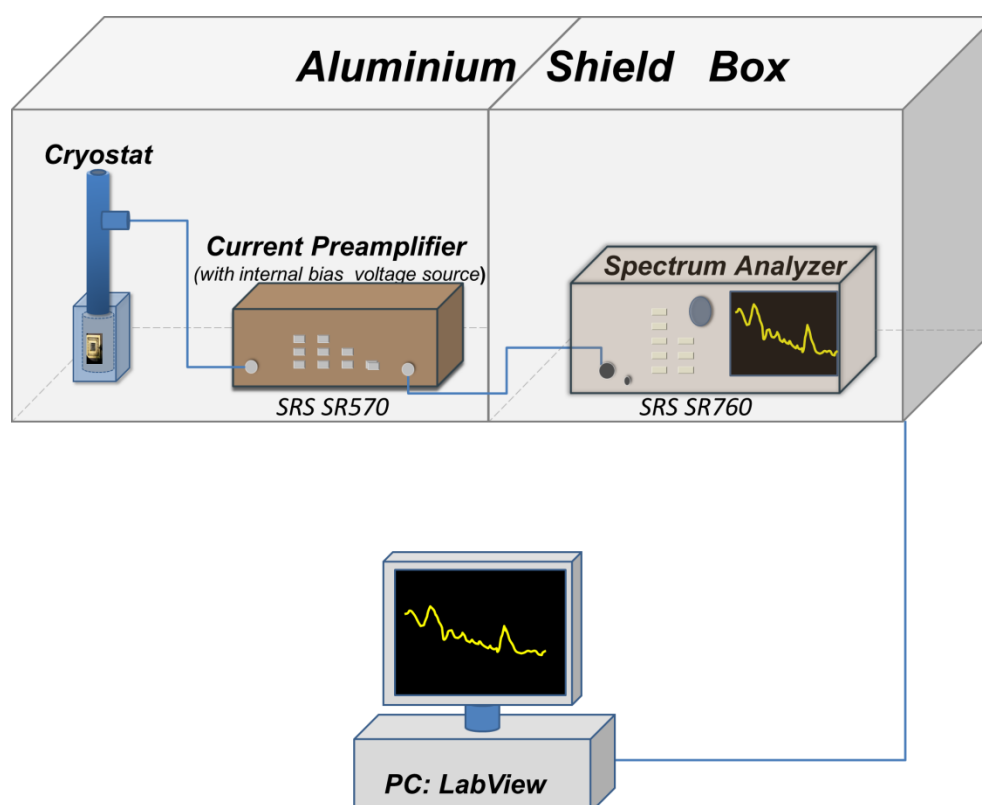
Figure 3.11 Noise Measurement Setup.

All the noise measurements are controlled by a computer with noise measurement vi written by LabVIEW software via GPIB and RS232 ports. Front and block panels of the software is given in Appendix A.

CHAPTER 4

ELECTRICAL AND OPTICAL ANALYSIS

In this chapter, results of optical and electrical measurements are presented and discussed. Responsivity, quantum efficiency, dark current density and RA results are discussed for SL2, SL3 and SL4 diodes. In particular, we focused on device performance for these three different designs, and the effect of surface passivation with Si_3N_4 and SiO_2 layers. Response time result of SiO_2 passivated SL3 sample is also briefly discussed. In all measurements, the photodiode size used is $400x400\mu m^2$. All the measurements are realized at approximately 79K sample temperature.

4.1. Optical Results

Optical results in terms of responsivity, quantum efficiency and response time are presented in this section. All the measurements are carried out as described in Chapter 3.

4.1.1. Responsivity and Quantum Efficiency

Figure 4.1 (a) shows the results of unpassivated samples for the three structures. It can be observed that the best result is achieved in SL4 sample and SL2 sample shows the least peak responsivity value. These results are meaningful due to the fact that in p-i-n junction photodiodes, photocurrent is created in the intrinsic (non-intentionally doped) and p-type regions. In the structure of SL4 sample, the total period of i and p-

type regions is 180 while it is 150 in SL3 sample and 130 in SL2 sample. Peak responsivity values are 1.27 A/W, 1.2 A/W and 1.15 A/W for SL4, SL3 and SL2 samples respectively. The peak responsivity values are at 3.95μm for each sample. We see that the responsivity correlates well with the thicknesses of the active absorbing region of the diodes.

In the (b) part of Figure 4.1, maximum quantum efficiency values are 45% at 3.1μm, 43% at 3.27μm and 39% at 3.26μm for SL3, SL4 and SL2 unpassivated samples, respectively. Quantum efficiency of SL3 sample is higher than SL4's up to 3.3μm and this is in agreement with the responsivity values. While quantum efficiency curve of SL2 sample is still the lowest one, maximum quantum efficiency value is reached by SL3 sample at short wavelength values. This result seems to be in contradiction with the responsivity results however it can be easily understood when we consider that the energy of a photon at 3μm (0.41meV) is 33% higher than that at 4μm (0.31meV) where the responsivity values for these wavelengths are close to each other. One photon, regardless of its energy, can excite one electron. Since the quantum efficiency values is given by the ratio of photo excited carriers per incident photons and the responsivity is a function of incident photon energy, one obtains lower responsivity values for short wavelengths.

In Figure 4.2 (a), effects of passivation layers on SL3 samples are given. Peak responsivity values are 1.25 A/W at 3.95μm, 1.24 A/W at 4.08μm, 1.2 A/W at 3.95μm and 1.08 A/W at 3.27μm for SiO2 passivated, Al2O3 passivated, unpassivated and Si3N4 passivated SL3 samples respectively. Like other materials, the molecules in the passivation layers scatter and/or absorb the IR radiation. Therefore, the passivation layer may cause some decrease in responsivity and quantum efficiency values.
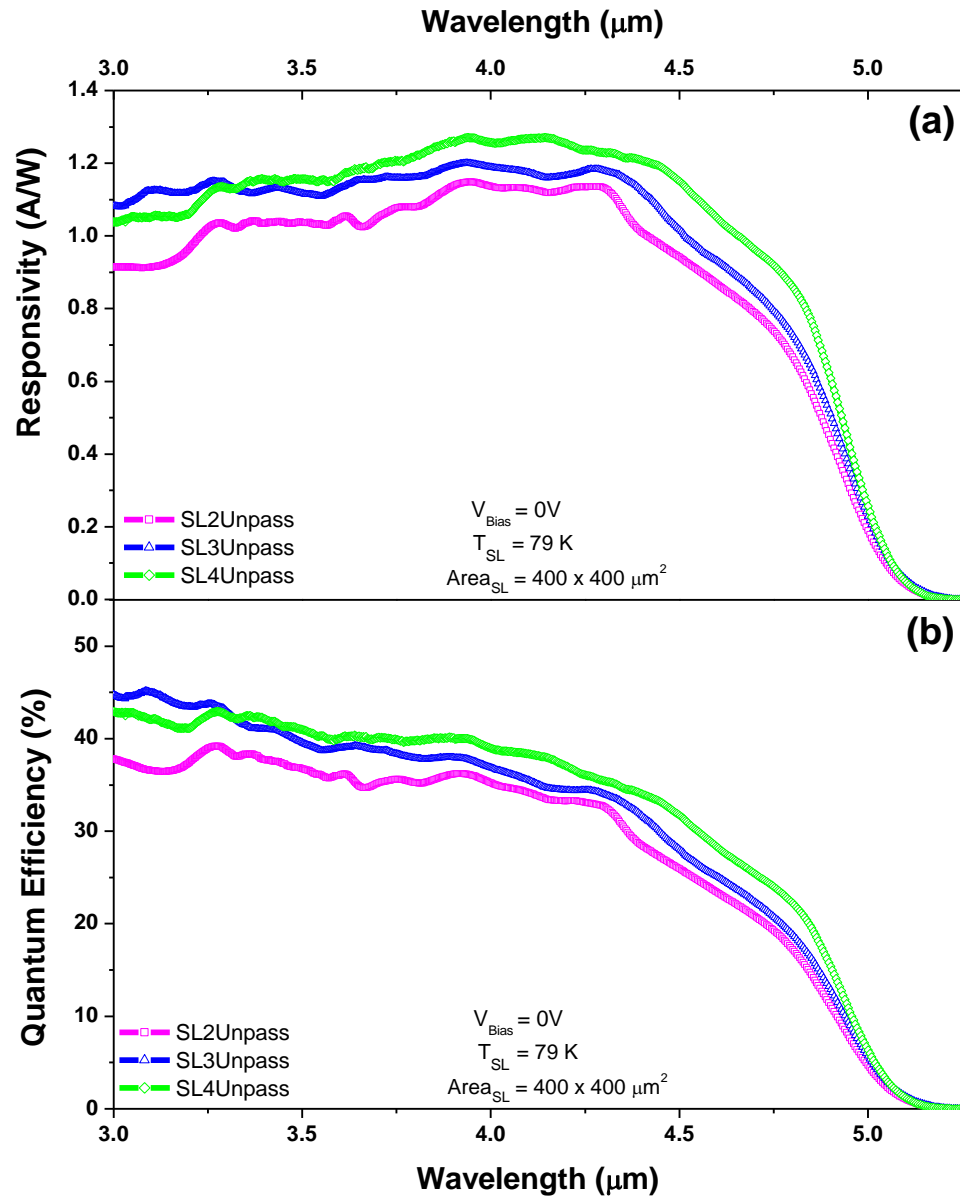
Figure 4.1 Responsivity and Quantum Efficiency curves of unpassivated SL2, SL3 and SL4 samples.

On the other hand, if the applied passivation works well, one might expect improvement in the responsivity due to the fact that the passivation material fills the surface states, i.e. dangling bonds on the surface, impurities and defects in the surface region of semiconductor. By filling surface states with an appropriate passivation material, the probability of carrier trapping by surface states will be lowered. Therefore, depending on the effectiveness of the positive and negative functions, the passivation layers may improve or degrade the optical performance of the photodiode.

In Figure 4.2 (a), it is seen that the responsivity performance of SL3 sample passivated with Si_3N_4 degrades when compared to the unpassivated SL3 sample. It is however, not clear that the degradation is a consequence of whether less photon incidence due to scattering and/or absorption or creation of more surface states due to an inappropriate passivation. Therefore, optical measurements by itself cannot conclude on physical mechanisms for the result of Si_3N_4 passivation.

In contrast to the results of Si_3N_4 passivation, SiO_2 passivated sample shows both improvement and degradation characteristics. Between 3.75μm and 4.3μm, there is an improvement in the responsivity of SL3 sample passivated with SiO_2 while between 3μm and 3.55μm region, there is an obvious degradation.

Al_2O_3 has similar optical results with unpassivated sample as well as SiO_2 passivated one. Peak responsivity value is a higher than unpassivated one however it does not show any absorption characteristic like the other passivation layers.

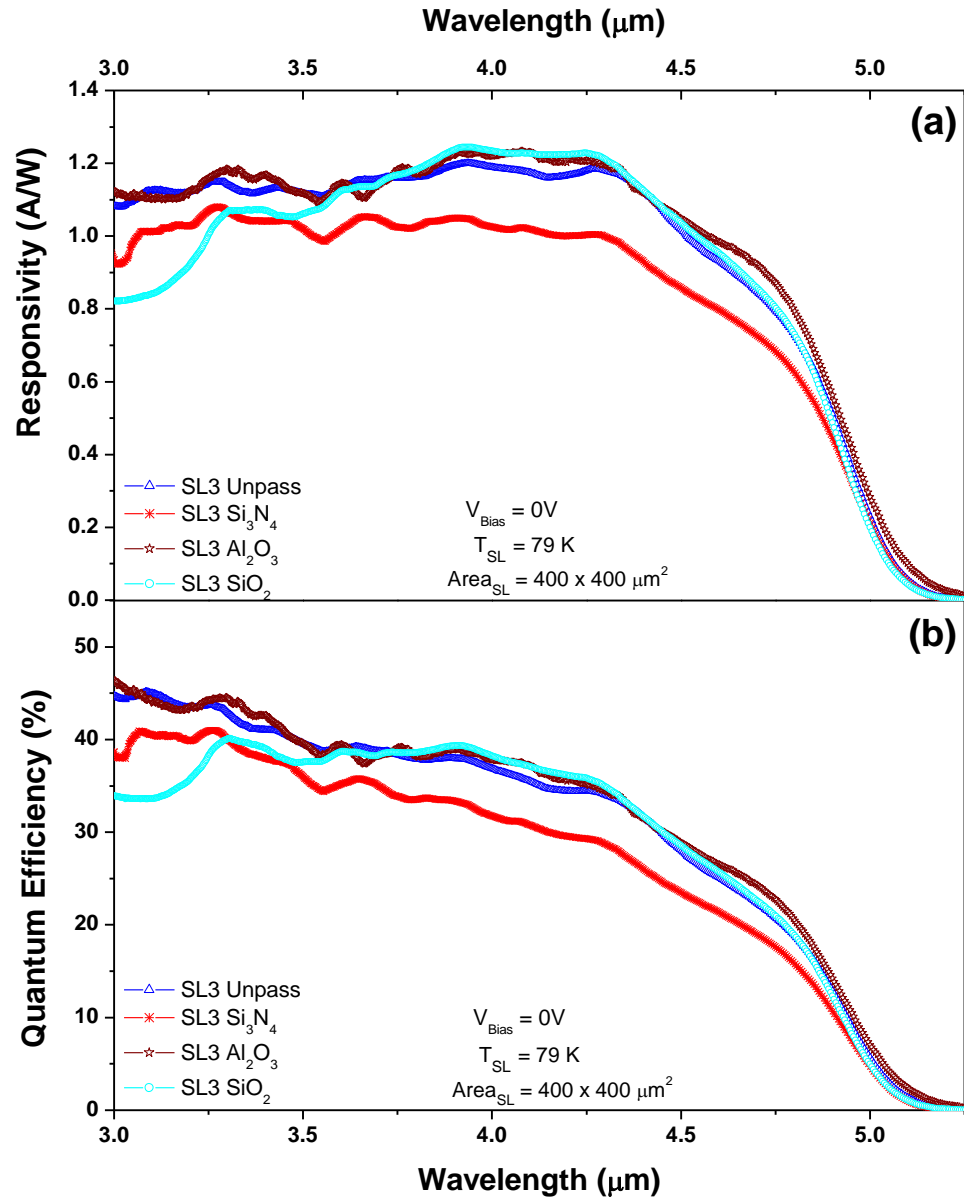**Figure 4.2 Responsivity and Quantum Efficiency curves of SL3 samples with different passivations.**

In part (b) of Figure 4.2, maximum quantum efficiency values are 46% at 3.07μm, 45% at 3.09μm, %41 at 3.25μm and %40 at 3.3μm for AL_2O_3 passivated, unpassivated, Si_3N_4 passivated and SiO_2 passivated SL3 samples respectively. While SiO_2 passivated sample gives the highest peak responsivity value, it gives the lowest result in peak quantum efficiency value. The reason of this exchange is discussed above in the discussion part of Figure 4.1. The ultimate goal of research on single pixel detector is to develop imaging arrays, i.e. FPAs. When the pixels are integrated with the read-out circuit (ROC) electronics, the performance of the system is directly related to the amount of generated signal. Therefore, for this application, responsivity should be more crucial than the quantum efficiency.

Considering the results summarized above, it can be concluded that while SiO_2 provides a good passivation of the surface states and improves the optical performance of the device for the region closer to the mid-infrared region, it causes some degradation between 3μm - 3.55μm region possibly due to the absorption of the incident beam. Al_2O_3 passivation increase peak responsivity value by filling the surface states while transmitting IR radiation.

The responsivity and quantum efficiency values of Type-II SL single pixel photodetectors are very promising when comparing the results with the literature and Table 2.1. We have obtained high efficiency and responsivity with relatively straightforward device design. With more intelligent device design and improvement in the crystal growth, the device performance can be significantly improved.

Cut-off wavelength of a photodiode determines the wavelength limit of a photodetector and is directly related to bandgap of the material used. The wavelength that corresponds to the half of the peak responsivity value is defined as the 50% cut-off wavelength of the photodiode. 50%

cut-off wavelength values are 4.85μm for unpassivated SL2, SiO_2 and Si_3N_4 passivated SL3 samples, 4.89μm for unpassivated SL4 sample and 4.86μm for unpassivated and Al_2O_3 passivated SL3 sample. 100% cut-off wavelength indicates the wavelength where the signal approaches to zero. For all samples, 100% cut-off wavelength is 5.17μm. As a result, it can be concluded that as expected, the cut-off wavelength is independent of passivation layer and number of period of p-i-n regions.
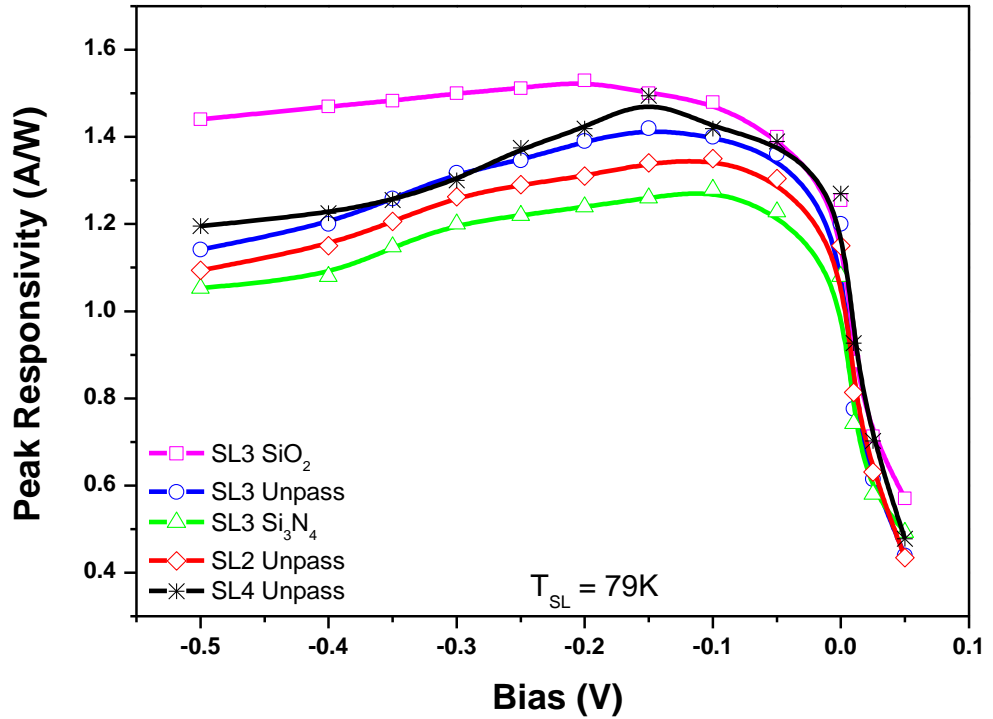
Figure 4.3 Peak Responsivity with respect to bias for all samples.

Figure 4.3 shows the variation of the peak responsivity with applied bias. The peak responsivity of all samples increases with the reverse bias and drastically decreases with forward bias which is expected for p-n

junction photodiodes. SiO$_2$ passivated SL3 sample has the greatest increment of all. Increments at peak responsivity values with respect to zero bias values are 23% at -0.2V, 17% at -0.15V, 19% at -0.1V, 18% -0.1 and 18% at -0.15 for SiO$_2$ passivated SL3, unpassivated SL3, Si$_3$N$_4$ passivated SL3, unpassivated SL2 and unpassivated SL4 samples respectively.
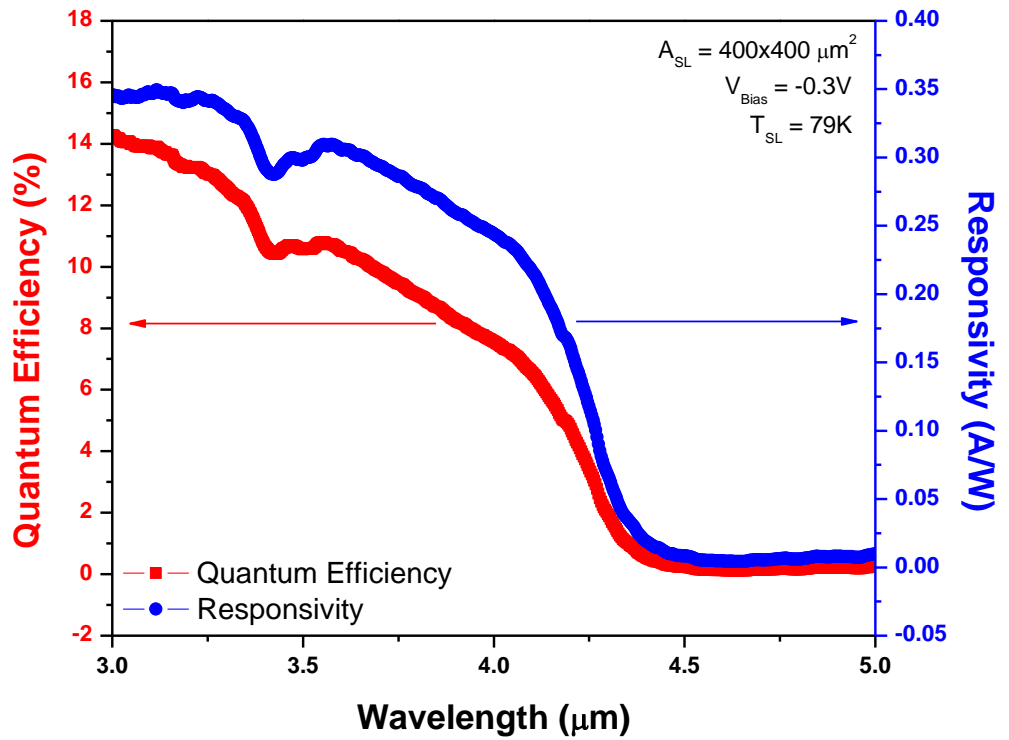
Figure 4.4 Responsivity and Quantum Efficiency of SiO$_2$ passivated SLN sample.

Responsivity and quantum efficiency results of SLN sample are given in Figure 4.4. AlSb layers affect both the cut-off wavelength and the peak responsivity of the photodiode. AlSb layers act as a barrier for photogenerated charge carriers and as a consequence the signal obtained

is not high. These layers narrow the width of quantum wells that causes higher ground state energy level and shorter cut-off wavelengths. By widening the layer thicknesses, not only the cut-off wavelength reach around 5µm, but also responsivity of photodiode increases by absorbing much more photons. It can be concluded that "N" structure does not provide any improvements in optical results yet, however it can achieve competitive result by introducing some minor modifications.

4.1.2. Response Time

In response time experiments, SiO_2 passivated SL3 sample is measured. The reason why the response time is measured at 100Hz chopper frequency can be understood from Figure 4.5, where the frequency response of the diode is seen.
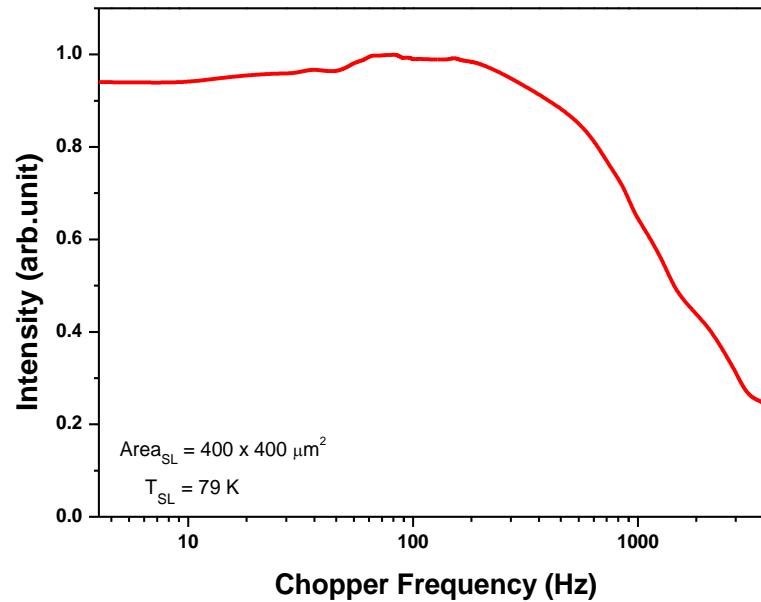
Figure 4.5 Intensity of signal with respect to chopper frequency.

Intensity of signal on the spectrum analyzer is at its maximum value at around 100Hz. After 200Hz, intensity begins to decrease due to the cut-off frequency of the voltage preamplifier.
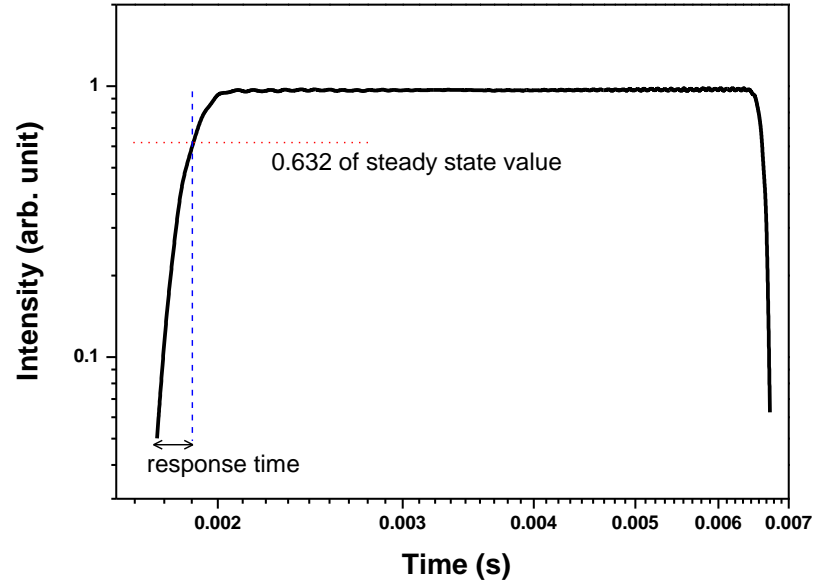
Figure 4.6 Response Time Curve of SL3 SiO₂ passivated sample at 79K, 100Hz.

The response time measurement graph is presented in Figure 4.6. The result is around 100μs which is an average response time for infrared detectors. This result can be improved by increasing mobility of carriers by introducing fewer scattering defects.

4.2. Electrical Results

Electrical results in terms of dark current density and RA presented in this section.

4.2.1. Dark Current Density and RA

RA values presented in this part of the study are calculated from dark I-V measurements as described in Chapter 3.4.1.

In Figure 4.7 (a), zero bias current density values are $531nA/cm^2$, $3.9\mu A/cm^2$, and $8\mu A/cm^2$ for $400\mu m$ x $400\mu m$ size, unpassivated SL2, SL3 and SL4 samples respectively at 79K. From the dark current density values, unpassivated SL2 sample seems to be the best one due to its lower dark current density; and it is also the same for R_0A values. However, this result is in the reverse order with respect to the responsivity results and the reason is probably the same; the more periods the structure have, the more electron-hole pairs are created.

In Figure 4.7 (b), R_0A values are $31k\Omega.cm^2$, $17k\Omega.cm^2$, and $10k\Omega.cm^2$ for SL2, SL3 and SL4 samples respectively. In R_0A calculations, the closest points to zero bias are taken into account. As can be seen in Figure 4.6 (a), the closest point near zero bias for SL2 sample has the lowest current density value. Therefore, SL2 sample has the highest value of R_0A.

If the RA values are compared with the results in the literature, it can be concluded that the wafer quality needs to be improved for FPA applications. Therefore, passivation process for this wafers is inevitable. In Figure 4.8, the dark current density and R_0A comparison of unpassivated, SiO_2, Si_3N_4 and Al_2O_3 passivated SL3 samples are shown. SL3 samples are used in order to observe the effect of passivation more clearly. In part (a), at zero bias, it is seen that, with respect to unpassivated sample ($3.95\mu A/cm^2$), while dark current density values of SiO_2 ($1.34\mu A/cm^2$) and Al_2O_3 ($0.56\mu A/cm^2$) passivated samples decreases 3 and 7 times respectively, the dark current density of Si_3N_4 passivated sample ($4.3\mu A/cm^2$) increases 1.1 times. At 500mV reverse bias value, the effect of passivation layers can be seen more clearly.
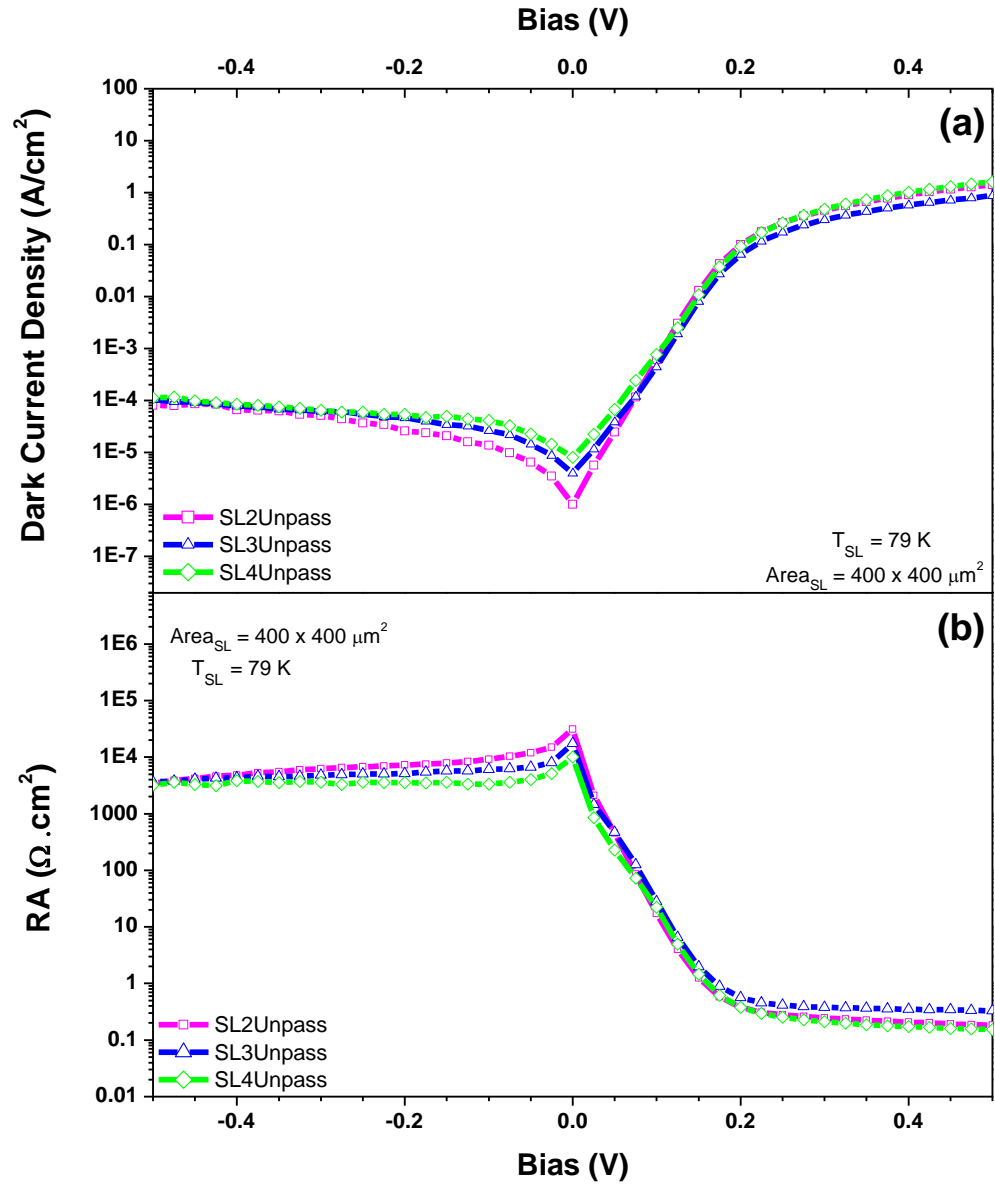
Figure 4.7 Dark Current Density and RA results of unpassivated SL2, SL3 and SL4 samples.

There is a two order of magnitude difference between dark current density of SiO_2 passivated sample and unpassivated one. However, the dark current density of Si_3N_4 is around one order of magnitude higher than unpassivated one. Therefore, we can conclude that SiO_2 passivation layer saturates the surface states on and near the surface of the device while Si_3N_4 passivation layer degrades the diode quality. Al_2O_3 deposition by ALD technique also works, in fact it decreases dark current at zero bias more than SiO_2 passivation. However, with increasing reverse bias, dark current of Al_2O_3 passivated sample tends to increase. The electrical potential created by Si_3N_4 layer might attract the charge carriers to the surface and thus enhance the surface leakage.

In part (b), the effect of passivation layers can be also observed in RA values. As in the dark current density results, there are not so much differences in R_0A values ($17k\Omega.cm^2$, $64k\Omega.cm^2$, $9k\Omega.cm^2$ and $155k\Omega.cm^2$ for unpassivated, SiO_2, Si_3N_4 and Al_2O_3 passivated samples respectively). However differences between values increase drastically with creasing reverse bias. While the peak RA values of unpassivated and Si_3N_4 passivated samples are at zero bias, that of Al_2O_3 and SiO_2 passivated samples are not at zero bias; they are $400\ k\Omega.cm^2$ and $500k\Omega.cm^2$ at 100mV reverse bias, respectively.

In a good photodiode, the change in the current around the zero bias is larger than the change in the reverse bias condition due to the fact that potential difference across the junction is higher at reverse bias than the difference at zero bias. This leads to a shift of peak resistance. The amount of shift depends on at how much reverse bias is needed to stabilize the potential difference. After reaching peak resistance, by increasing bias voltage, the resistance of diode begins the decrease due to the defect related current mechanisms.
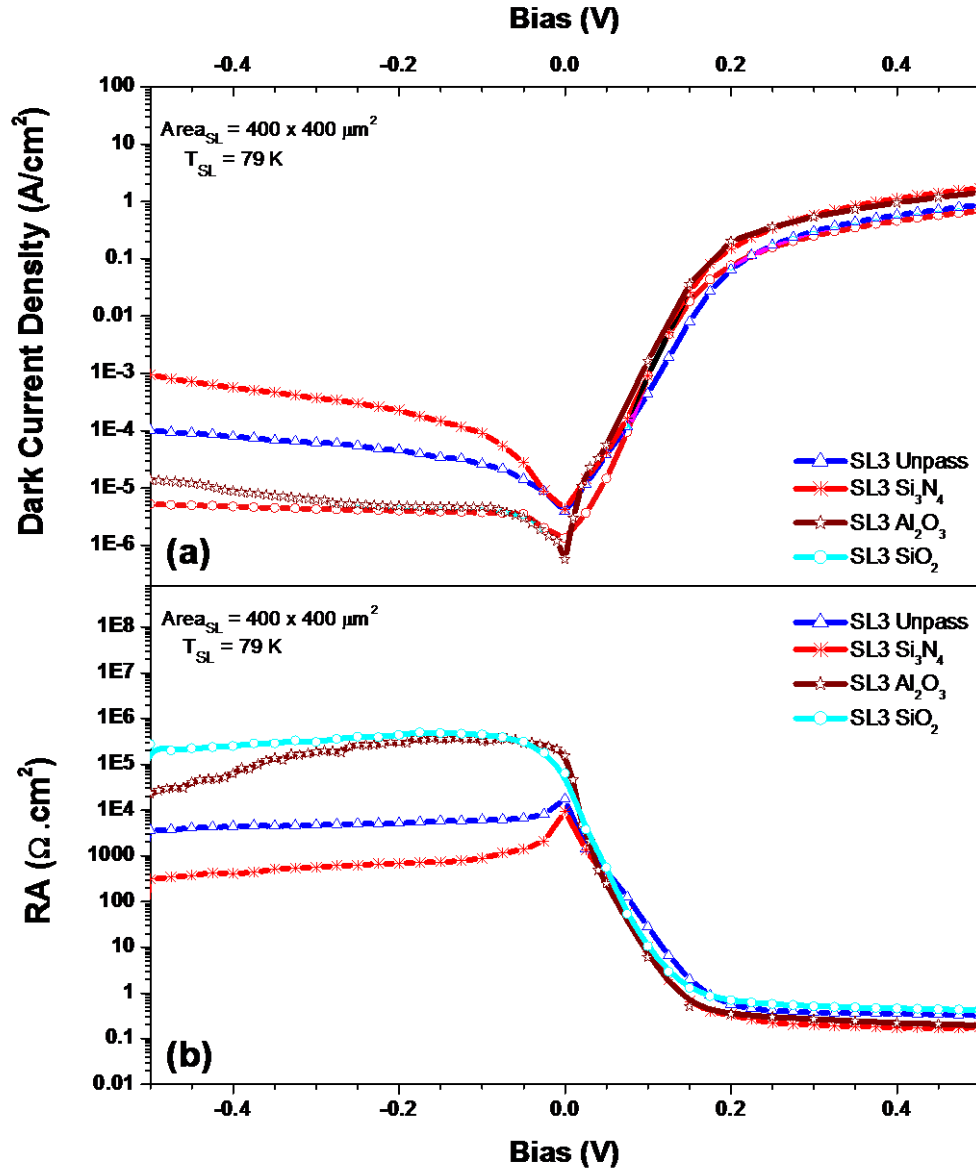
Figure 4.8 Dark Current Density and RA results of unpassivated, Si_3N_4, Al_2O_3, and SiO_2 passivated SL3 samples.
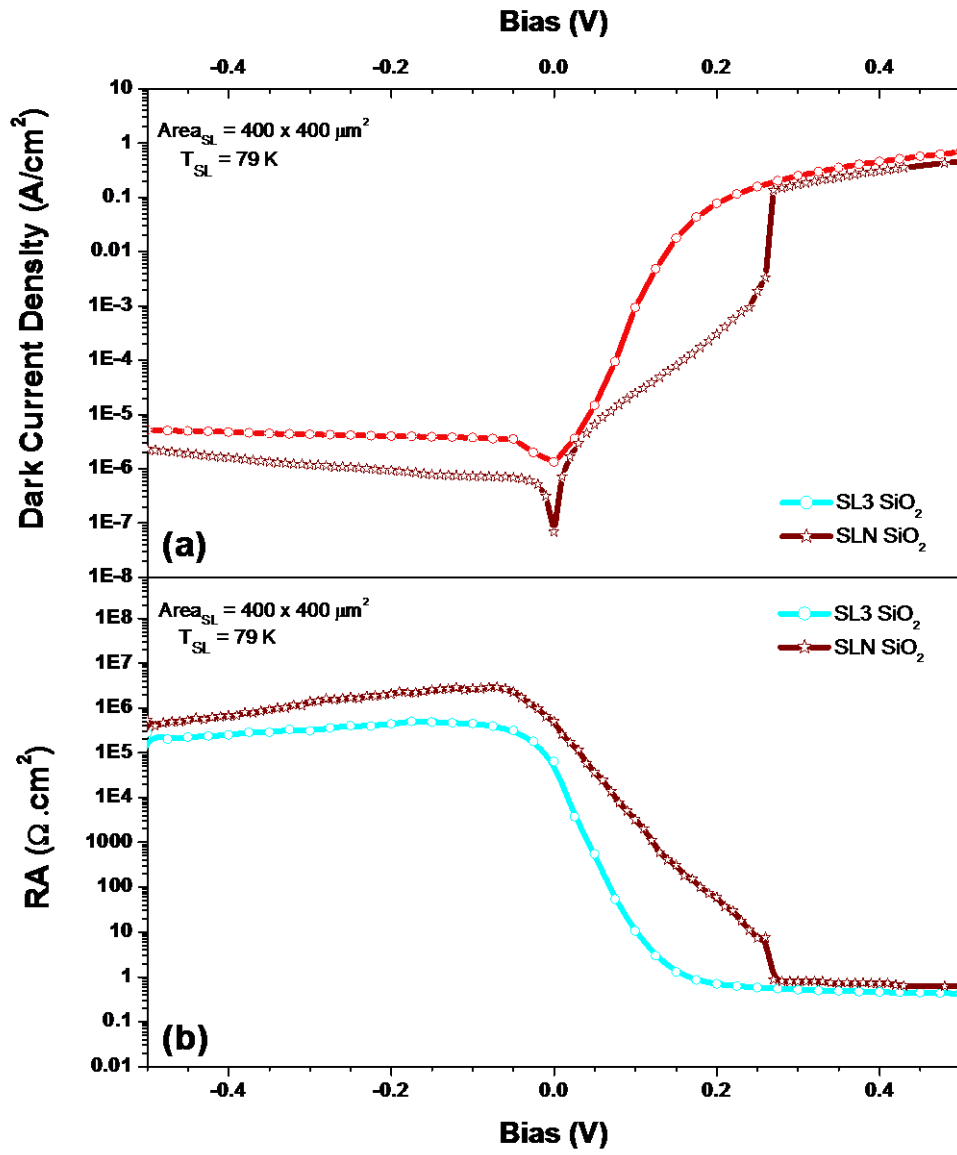
Figure 4.9 Dark Current Density and RA results of SiO$_2$ passivated SL3 and SLN samples.

In Figure 4.9, results of dark I-V measurement for SiO_2 passivated SL3 and SLN samples are given. The effect of AlSb barrier on charge carriers is impressively obvious. Dark current density of SLN sample ($70nA/cm^2$) is lower by two orders of magnitude and R_0A product ($500k\Omega.cm^2$) increase 8 times at zero bias. The energy of carriers probably is not sufficient to overcome from the barrier until 0.25V forward bias therefore there is drastic drop at that bias value. Further investigations are needed to clarify that effect.

RA results of straight forward design Type-II SL single photodetectors are not so close to the best values in the literature. By doing modification in the design, results can be improved as in the "N" structure. With improvement in the crystal growth and fabricating the device more attentively, higher RA results can be reached.

CHAPTER 5

NOISE ANALYSIS

In this chapter, noise characteristics of Type-II InAs/GaSb Superlattice single pixel detectors are discussed, types of detector noise are introduced, theoretical and experimental noise and detectivity results are compared. In order to match the experimental results and theoretical calculations, activation energy results are given and these results are used to propose a new noise type called surface recombination noise.

5.1. Noise Characterizations

Before presenting noise measurement results, noise types will be discussed. Then, passivation effects on noise characteristics are given and results will be compared with theoretical approaches.

5.1.1. Types of Detector Noise

In photon detectors, there are mainly 3 types of noise; Schottky noise, Johnson noise and 1/f noise.

- Schottky Noise:
  It is also known as shot noise. Schottky noise arises from discreteness nature of electron charge, as illustrated in Figure 5.1. Random generation and arrival of electrons causes time-

dependent fluctuations at output signal. Schottky noise is calculated by using Equation 5.1.1.1 [46].

$$i_{SN}^2 = 2qI\Delta f \qquad (5.1.1.1)$$

where q is electron charge, I is output signal in terms of current and Δf is signal bandwidth.
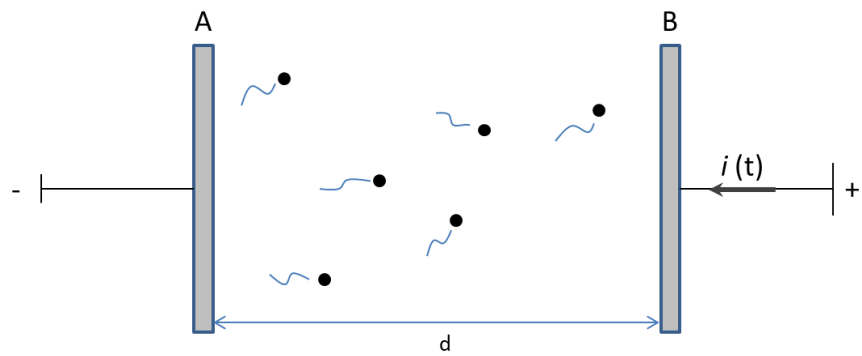
Figure 5.1 Schematic diagram for Shot Noise.

- Johnson Noise:

  It is also called as thermal noise due to the fact that Johnson noise is a consequence of thermal motion of charge carriers. Johnson noise can be calculated in term of voltage and current noise as shown in Equation 5.1.1.2 and 5.1.1.3 where k is Boltzmann constant, T is temperature, R is resistance and Δf is signal bandwidth [46].

$$v_{JN}^2 = 4kTR\Delta f \qquad (5.1.1.2)$$

$$i_{JN}^2 = 4kT\Delta f / R \qquad (5.1.1.3)$$

- 1/f Noise:

   It is also known as pink noise and flicker noise. 1/f noise is dependent on frequency, causes fluctuations in low frequencies and limits the low frequency detectivity. 1/f noise has no ultimate equation and is generally empirical. Therefore, in noise measurements, usually it is the noise type most struggled with.

5.1.2. Effect of Passivation Layers on Noise Characteristics

Johnson noise and Schottky noise are the intrinsic noises; consequences of physical events in the bulk material of detectors and form *white* noise $(i_{SN}^2 + i_{JN}^2)$ of the detector. 1/f noise is usually dependent on surface of the device; surface leakage current is one of the most essential sources of 1/f noise. Therefore, the noise measurements are realized with different types of surface passivation materials as in dark I-V measurements. The results of these measurements have already been published in IEEE Photonics Technology Letters [49].

Dark current noise vs. frequency measurements are carried out up to 200 Hz which is set by the cut-off frequency of current preamplifier at the gain value that we used. In most of the measurements at zero bias voltage, the dark current noise values match with the calculated white noise values at 30Hz therefore in dark current noise vs. bias voltage measurements, dark current noise values at 30Hz are taken into account.

The peaks at 50Hz, 65Hz and their harmonics are external discrete noises that cannot be prevented with Faraday cage. The peak at 50Hz is due to the AC oscillation rate of city electricity.

Figure 5.2 Dark current noise with respect to frequency for unpassivated SL3 sample at 0V and -0.1V.

In Figure 5.2, dark current noise characteristics as function of frequency at zero bias and 0.1V reverse bias for unpassivated SL3 sample are given. It is seen that the sample shows 1/f characteristic up to around 20Hz at zero bias voltage. Between 20Hz and 50Hz, calculated white noise value matches with the experimental data. On the other side, at -0.1V, the sample shows 1/f characteristic at the whole frequency spectra. Besides, the dark current noise value is 5 times higher than the white noise value at 30Hz. Therefore, by applying bias voltage, an additional noise source, which is not expected in advance, is introduced to the system.

In Figure 5.3, the difference between calculated white noise values and experimental data when bias is applied can be clearly observed. At -0.5V bias, experimental dark current noise is 7 times higher than white noise value at that bias. Therefore, it can be concluded that application of bias causes additional noise in the device.

In Figure 5.4, dark current characteristics as a function of frequency at zero bias and 0.1V reverse bias for Si_3N_4 passivated SL3 sample is given. It is observed that the sample shows 1/f characteristics up to around 25Hz at zero bias voltage.
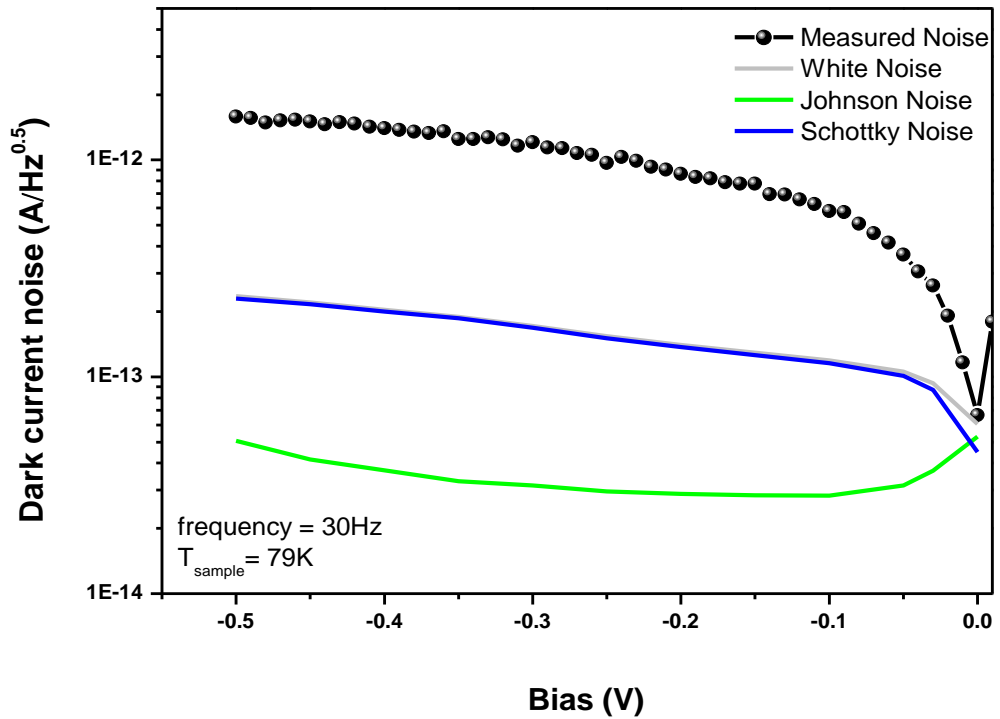
Figure 5.3 Dark current noise with respect to bias voltage for unpassivated SL3 sample.

Between 25Hz and 50Hz, calculated white noise value matches with the experimental data. On the other side, at -0.1V, the sample shows 1/f characteristic at the whole frequency spectra as the unpassivated sample. The dark current noise value is 3.5 times higher than the white noise value at 30Hz. Hence, the same conclusion as the unpassivated sample is also valid for Si_3N_4 passivated sample with a less difference between the white noise and experimental noise. There may be two explanation of this: even if the passivation does not work, it suppresses the additional noise source or additional noise cannot be so dominated when the total dark current noise is too high.
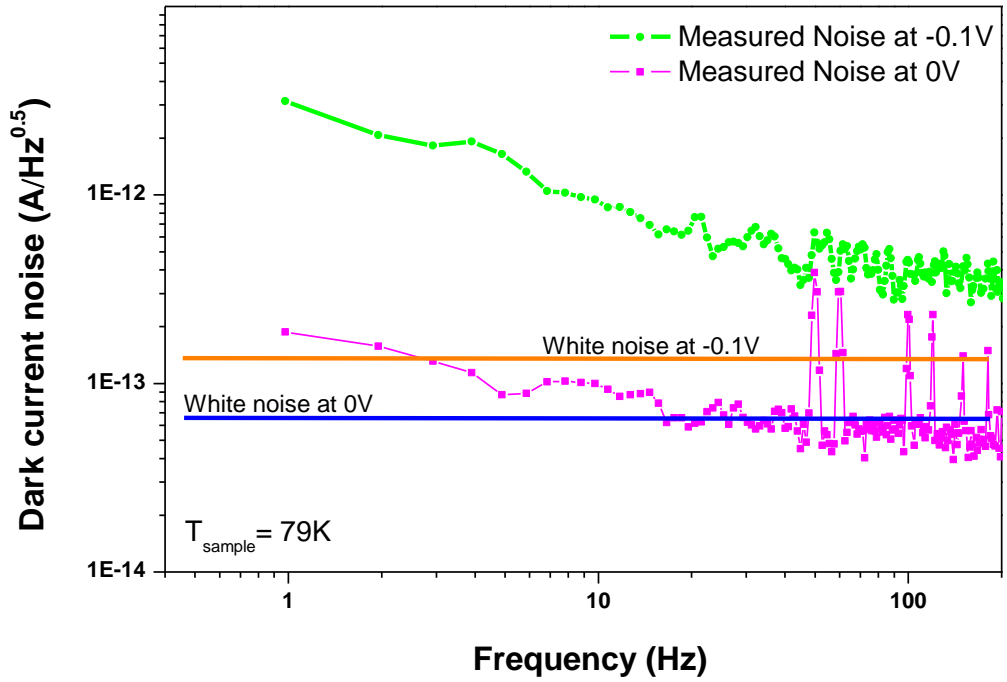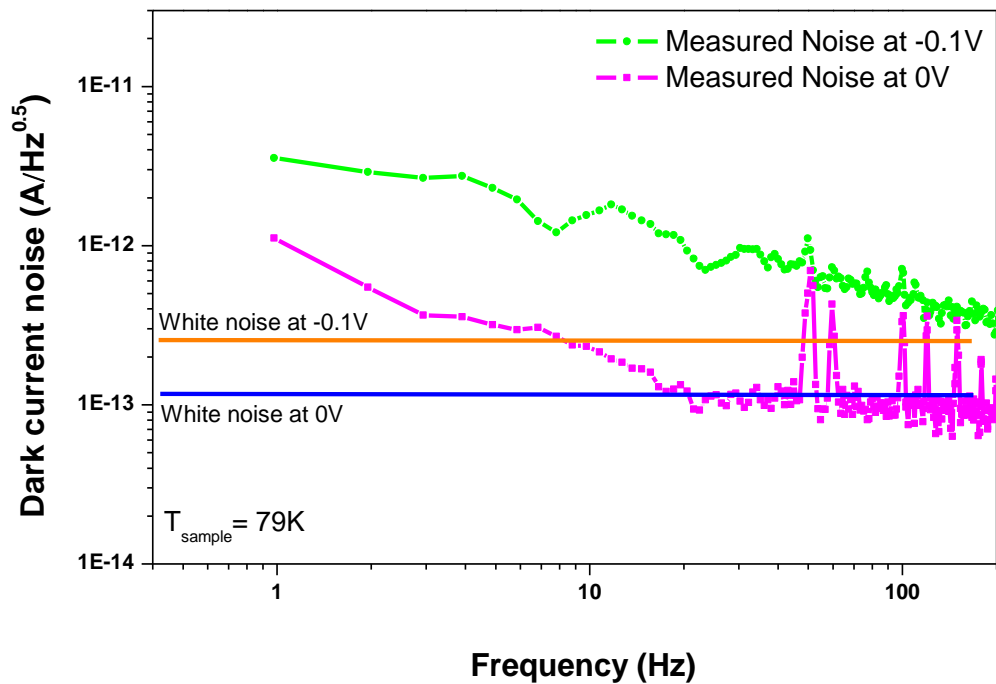

Figure 5.4 Dark current noise with respect to frequency for Si_3N_4 passivated SL3 sample at 0V and -0.1V.
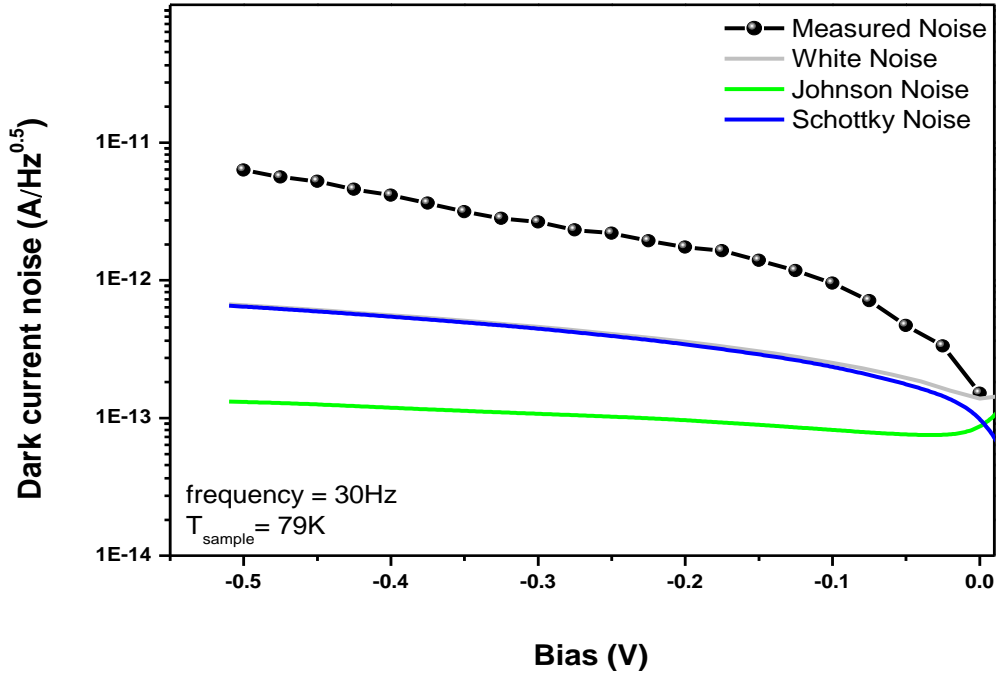
Figure 5.5 Dark current noise with respect to bias voltage for Si$_3$N$_4$ passivated SL3 sample.

Figure 5.5 shows the difference between white noise and the experimental noise for Si$_3$N$_4$ passivated SL3 sample. The difference is higher than 1 order of magnitude at 0.5V reverse bias.

In Figure 5.6, dark current characteristic as function of frequency at zero bias and 0.5V reverse bias for SiO$_2$ passivated SL3 sample is given. It can be seen that the sample shows 1/f characteristic up to around 20Hz at zero bias voltage. Unlike the unpassivated and Si$_3$N$_4$ passivated samples, dark current noise spectra is given for V$_{bias}$ = -0.5V instead of V$_{bias}$ = -0.1V. The reason is that the dark current noise values and white noise values at -0.1V bias and zero bias cannot be distinguished easily. Between 20Hz and 50Hz, calculated white noise value matches with the experimental

data at zero bias. On the other side, at -0.5V, the sample shows 1/f characteristic for the whole frequency domain as the other samples results at -0.1V. The dark current noise value is 2.8 times higher than the white noise value at 30Hz even at -0.5V.
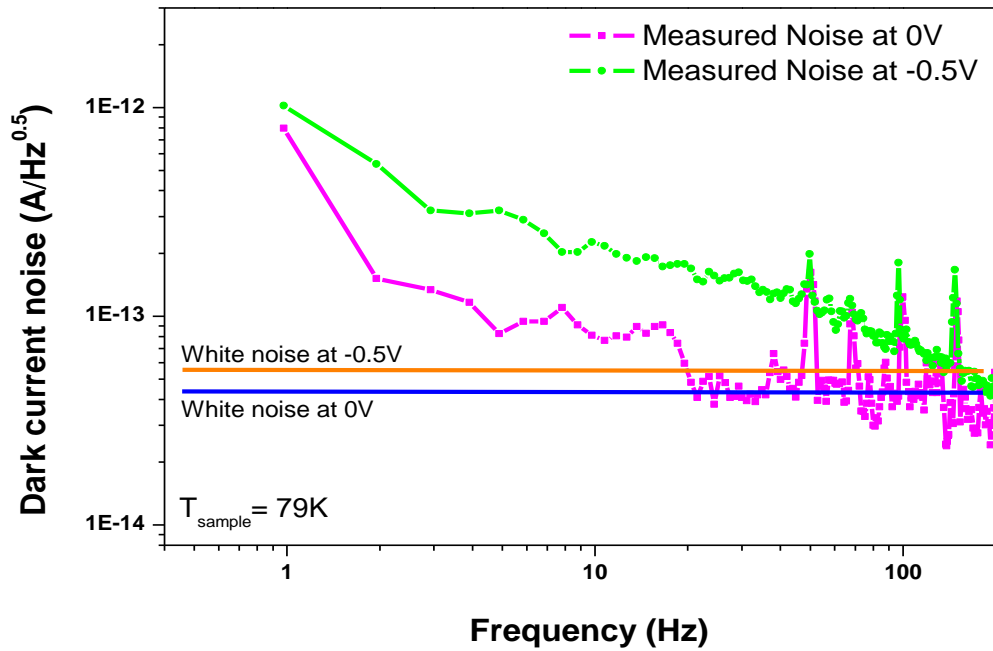
Figure 5.6 Dark current noise with respect to frequency for SiO$_2$ passivated SL3 sample at 0V and -0.5V.

In Figure 5.7, up to -0.18V, white noise values are very close to the experimental data. At reverse bias voltage values higher than 0.2V, a similar difference between white noise and experimental noise is observed as in the unpassivated and Si$_3$N$_4$ passivated samples. SiO$_2$ passivation can suppress additional noise up to -0.18V even if the total noise is very low compared to the other samples. The additional 1/f related noise does not dominate the system up to a point if an appropriate passivation is applied.
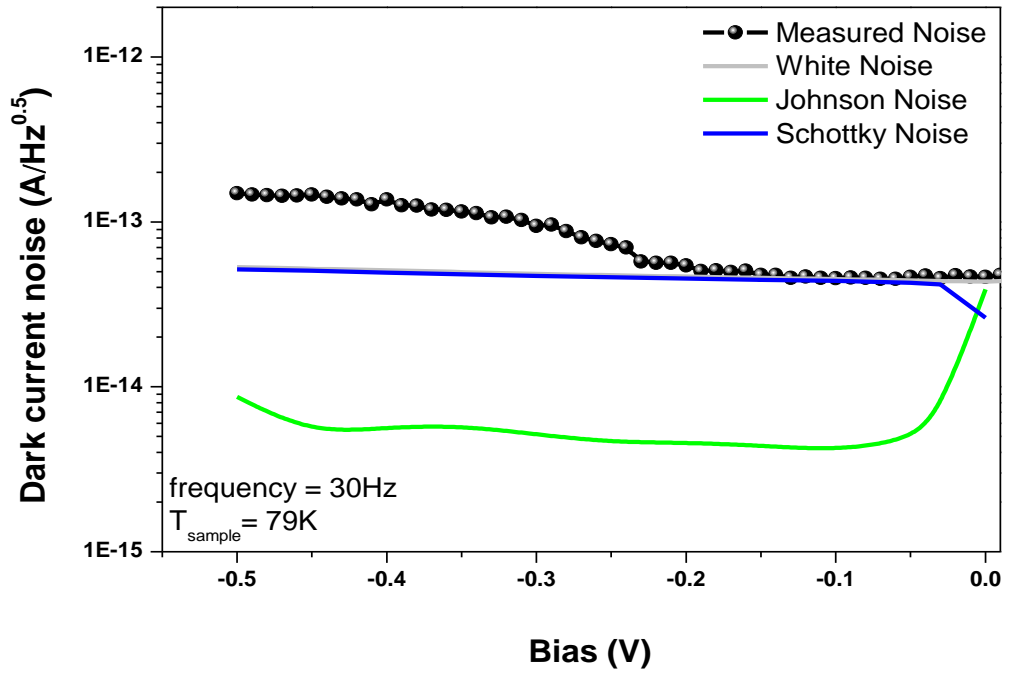
Figure 5.7 Dark current noise with respect to bias voltage for SiO_2 passivated SL3 sample.

5.1.3. Detectivity Results

After obtaining responsivity and dark current noise values, the detectivity values can be determined. Detectivity values can be calculated using either measured dark current noise values or calculated white noise values. Therefore, we will able to show the difference in detectivity values between theoretically calculated and experimentally obtained for SL3 samples.
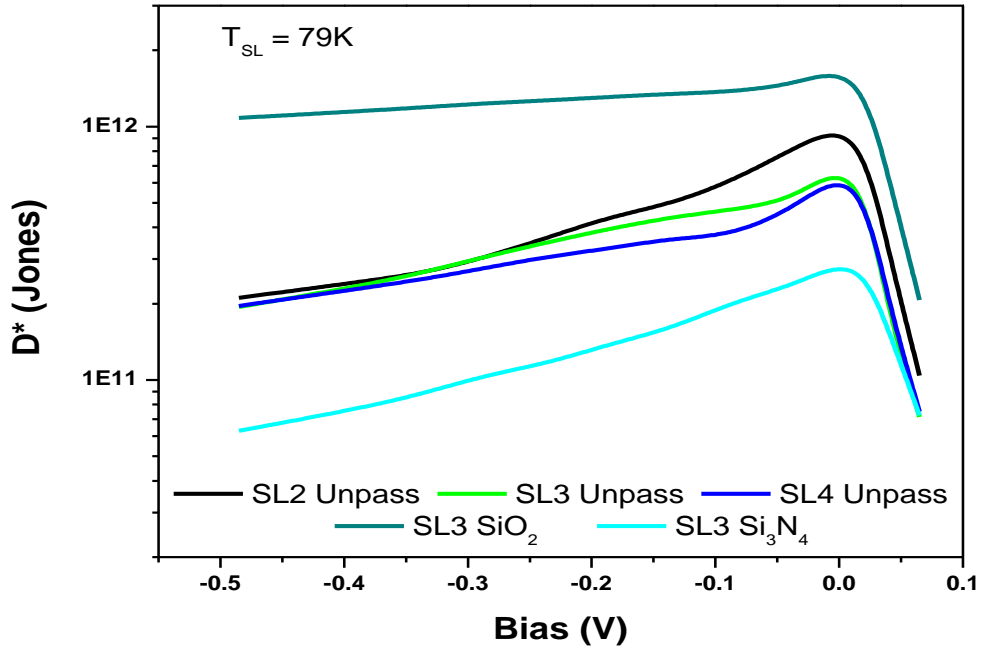
Figure 5.8 Detectivity curves calculated by using white noise data for regular samples.

Figure 5.8 shows the detectivity values calculated with white noise data with respect to applied bias for regular samples. As given in Equation 3.1.3.1, there are two parameters, namely responsivity and dark current noise, in the detectivity equation. While peak responsivity data of all samples shift to higher reverse bias values, detectivity values peak at zero bias as in the dark current noise values. This demonstrates the importance of dark current noise.

Effect of low dark current noise on detectivity can be clearly seen in the result of SiO_2 passivated SL3 sample which has the highest detectivity value of 1.8×10^{12} Jones. While detectivity values of SiO_2 passivated SL3 sample stays almost constant with increasing reverse bias, those of all

other samples drastically decrease. Peak detectivity values are 9.5×10^{11} Jones, 6.4×10^{11} Jones, 6×10^{11} Jones and 2.9×10^{11} Jones for unpassivated SL2, unpassivated SL3, unpassivated SL4 and Si_3N_4 passivated SL3 samples respectively.

Figure 5.9 shows the effect of noise measurement on detectivity results. Except zero bias detectivity value, it is clearly seen that the detectivity results calculated with white noise data does not reflect true detectivity values for unpassivated SL3 sample. The misleading also occurs at higher reverse bias values than -0.15V for SiO_2 passivated sample. These results demonstrate the importance of the noise in determining the detectivity of the photodiode.

Detectivity values calculated using white noise values for Al_2O_3 passivated SL3 sample and SiO_2 passivated SLN samples are 2.7×10^{12} Jones and 2×10^{12} Jones respectively. Both detectivity values are higher than that of standard design and regular passivation methods. It is seen that dark current and resistance of diode are so crucial because even if the responsivity of SLN structure is 4 times lowered than others, detectivity value is higher than those.

The highest detectivity results in the literature (Table 2.1) exceed 10^{13} Jones while we reached 2.7×10^{12} Jones with SiO_2 passivated SLN sample even if the responsivity value of that sample is very low. Therefore, SLN sample can compete with the results in the literature by increasing its responsivity.
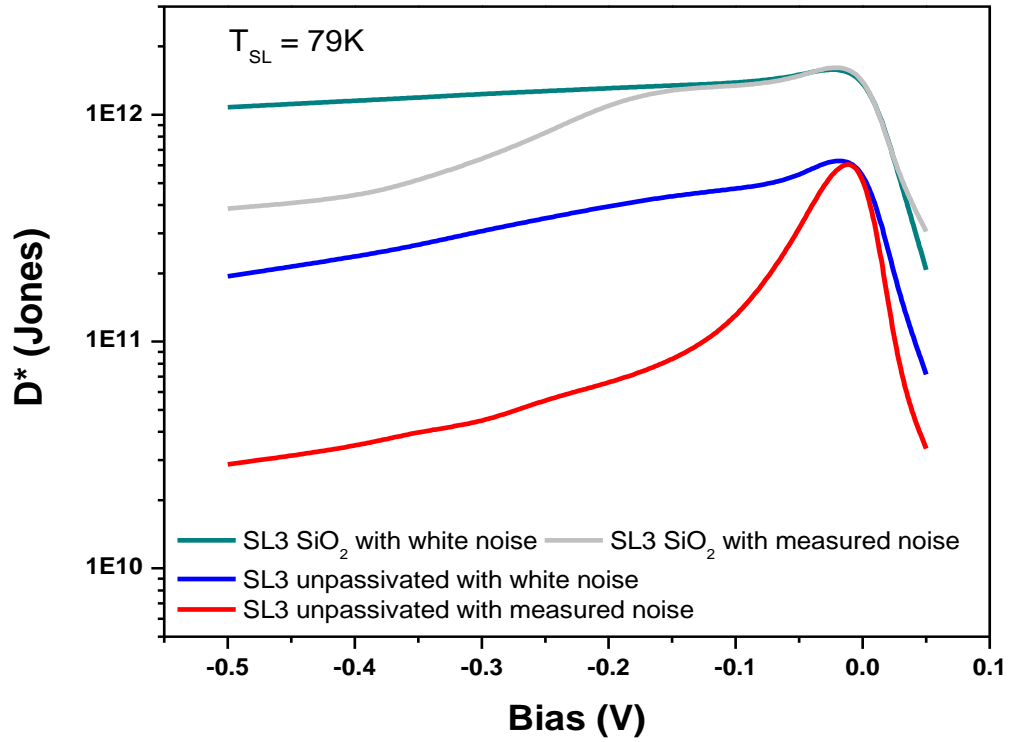
Figure 5.9 Comparison of detectivity curves calculated with white noise data and measured noise data for unpassivated and SiO$_2$ passivated SL3 samples.

5.2. Activation Energy Calculations

As mentioned above, the additional noise acts as 1/f noise and probably due to the surface leakage current. The relation between surface currents and the noise properties of the detector needs to be clarified for a complete understanding. In order to do this, first of all it should be verified that at temperature range around 80K, the dominant current mechanism is surface limited current. Temperature dependent I-V measurements and Arrhenius Plot analysis provides evidence for dominated current mechanisms.

Figure 5.10 shows results of temperature dependent I-V measurements in the form of resistance vs. bias for temperature range from 11K to 250K for SiO_2 passivated SL3 sample. The effect of temperature on resistance of the photodiode is clearly seen.

This measurement is also realized for unpassivated and Si_3N_4 passivated SL3 samples. For each temperature, resistance values at specific bias values are extracted from the data to plot resistance as a function of inverse temperature graph as presented in Figure 5.11.
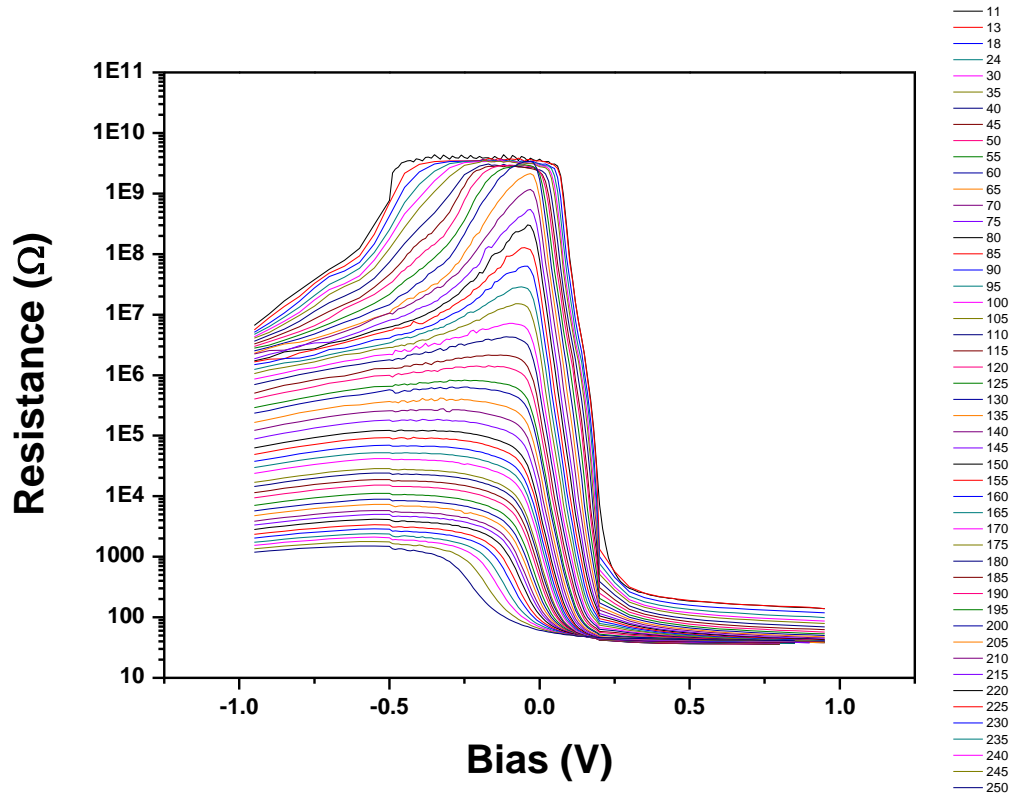
Figure 5.10 Resistance vs. Bias results from 11K to 250K temprature range for SiO₂ passivated sample.

Figure 5.11 shows 3 different current mechanisms for different temperature regions. At temperature values higher than 200K, thermal energies of charge carriers are sufficient to realize band-to-band transition. Therefore the first slop of Arrhenius plot indicates the diffusion current mechanism.

From the slope using Equation 5.2.1, activation energy (E_{act}) required in band-to-band transition can be calculated which is also equal to the bandgap of the device obtained from optical measurements [50]. It is found 0.243meV, very close to optical measurements.

$$E_{act} = k \left(\frac{\partial \ln R_0 A}{\partial u} \right), \ u = 1000/T \qquad (5.2.1)$$

The equation is also applicable to other slopes. The slope between 200K and 100K indicates Generation-Recombination centers (G-R) limited current mechanism. In the middle of the band gap, there might be states due to the impurities at the crystal structures. Electrons can excite (be generated) from valence band to these states or from these states to conduction band. Inverse process is also possible: electrons can deexcite (recombine) from conduction band to impurity states or from impurity states to valence band. The creation or loss of electron in this way is called as Generation-Recombination (G-R) current. G-R current mechanism dominates when thermal energy of electrons is not sufficient for band-to-band excitation.

The third slope refers to the surface limited current as stated in References [37], [34]. For this sample, surface limited current mechanism is valid from 100K to 70K temperature range. It is related with the surface states on and near the surface of the device. Due to the fact that 1/f noise is related with surface currents, activation energy values of surface limited current mechanism is calculated and given in Figure 5.12.
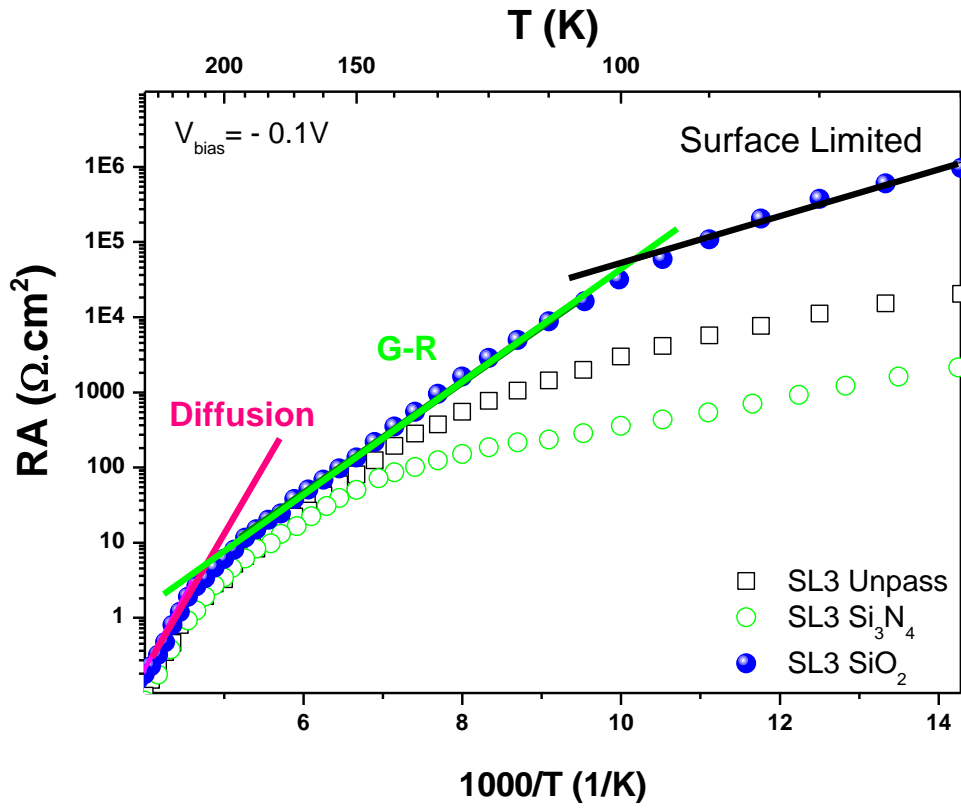
Figure 5.11 Arrhenius plot of unpassivated, SiO$_2$ and Si$_3$N$_4$ passivated SL3 samples.

Clearly, an inverse dependence is seen between E$_{act}$ and V$_{bias}$ for all samples. For each sample, their experimental noise curve and activation energy noise curve are symmetrical about the x-axis. The separation between white noise and measured noise in the SiO$_2$ passivated sample begins at -0.18V bias. The activation energy value for this sample at that bias value is around 60meV. Activation energy values of unpassivated and Si$_3$N$_4$ passivated samples at zero bias are also around 60meV. As mentioned in Chapter 5.1.2, additional noise begins to dominate the dark current noise at higher reverse bias voltage. Therefore, 60meV activation energy value acts as a threshold value for the additional noise.
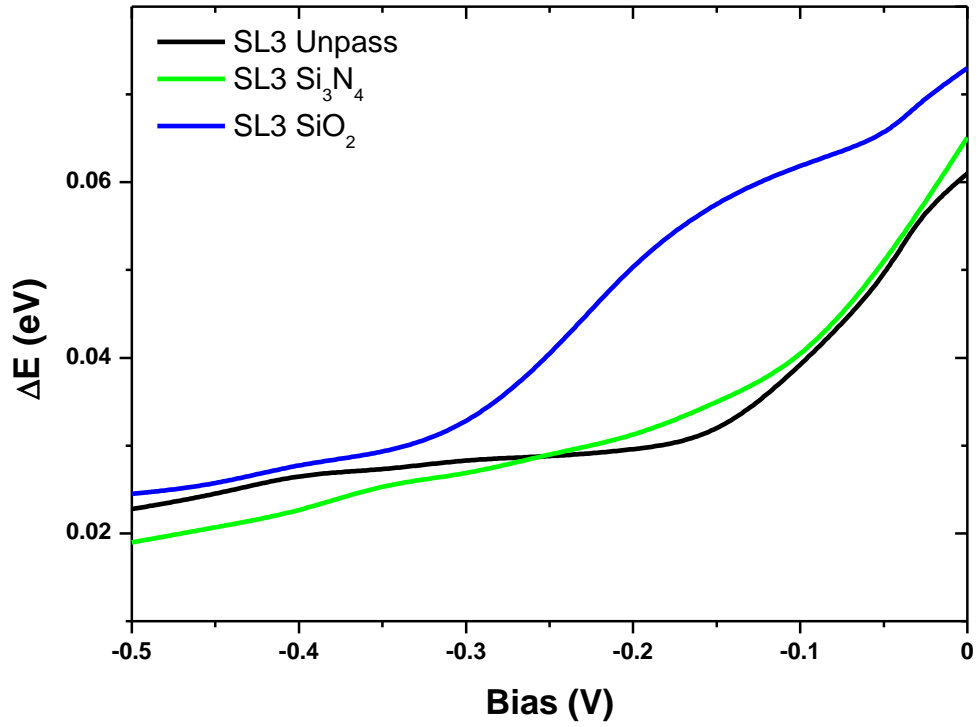
Figure 5.12 Activation Energy as a function of revers bias for unpassivated, SiO$_2$ and Si$_3$N$_4$ passivated SL3 samples.

5.3. Proposal of Surface Recombination Noise

The difference between the measured noise and white noise data can be explained by a model based on the variation of surface potential with the applied bias. We assume that E$_{act}$ of surface states is lowered by the applied electric field and leads to an increase in the number of charge carriers flowing to the surface. However, the charge carriers flowing to the surface cannot be observed in dark I-V measurements. This means that the charge carriers do not leave the device. Although they flow to the surface, they are lost on the surface

and create noise. The most logical explanation of this fact is the recombination of charge carriers on the surface therefore we propose a new noise type called as surface recombination noise. For E_{act} higher than 60meV, Schottky-noise dominates however, for E_{act} smaller than 60meV, the dominating noise type is surface recombination noise at reverse biases greater than - 0.15V in the SiO_2 passivated sample. Hence, decreasing the surface activation energy with applied reverse bias causes more surface recombination noise that acts as an independent noise source. This 1/f-noise source is dominant at the activation energies corresponding to the bias voltages lower than 60meV. Due to the fact that this is a consequence of recombination process, no additional current flow can be seen in I-V characteristics. This noise is only seen in direct noise measurements.

Clearly, surface recombination noise should be related to the surface carrier concentration (n_s) which is strongly dependent on the operating bias voltage for a given temperature. Moreover, an exponential dependence on the activation energy $E_{act,}$ as $n_s \sim \exp(-E_{act}/k_B T)$ where n_s is the electron (or hole) concentrations is expected [50]. Assuming that it is proportional to carrier concentration, the surface current, I_{sc}, can be write as

$$I_{sc} = I_c \exp(-E_{act}/k_B T) \tag{5.3.1}$$

where I_c is the proportionality constant.

According to Ref. [51], the surface recombination noise I_{srn} of SL photodiodes can be calculated using

$$I_{srn}^2 = 2qI_{lc}\,\Delta f \tag{5.3.2}$$

By claiming that all the noise sources (*i.e.* I_{JN}, I_{SN} and I_{srn}) are statistically independent, the total noise I_{total} is then found as

$$I^2_{total}= I^2_{SN} + I^2_{JN} + I^2_{srn} \qquad (5.3.3)$$

To demonstrate the validity of equation (5.3.3), it is fitted to the experimental dark current noise in the voltage range [0 - 0.5V] to identify the dominant bias-dependent dark current noise component, as shown in Figures 5.13.

In order to obtain the best agreement between experimental values and noise calculations, only the parameter I_c was varied as the fitting parameter in the calculation of the total noise dark current density I^2_{total} at around 79K. Other parameters such as E_{act}, I_{SN} and I_{JN} were deduced from the experimental data. An excellent agreement between the fitted curves and experimental data for the unpassivated, SiO_2, and Si_3N_4 passivated SL diodes is observed. This agreement strongly suggests that the additional dark current noise results from the carrier recombination on the surface.

The results presented in this chapter have been submitted to Applied Physics Letters for publication.
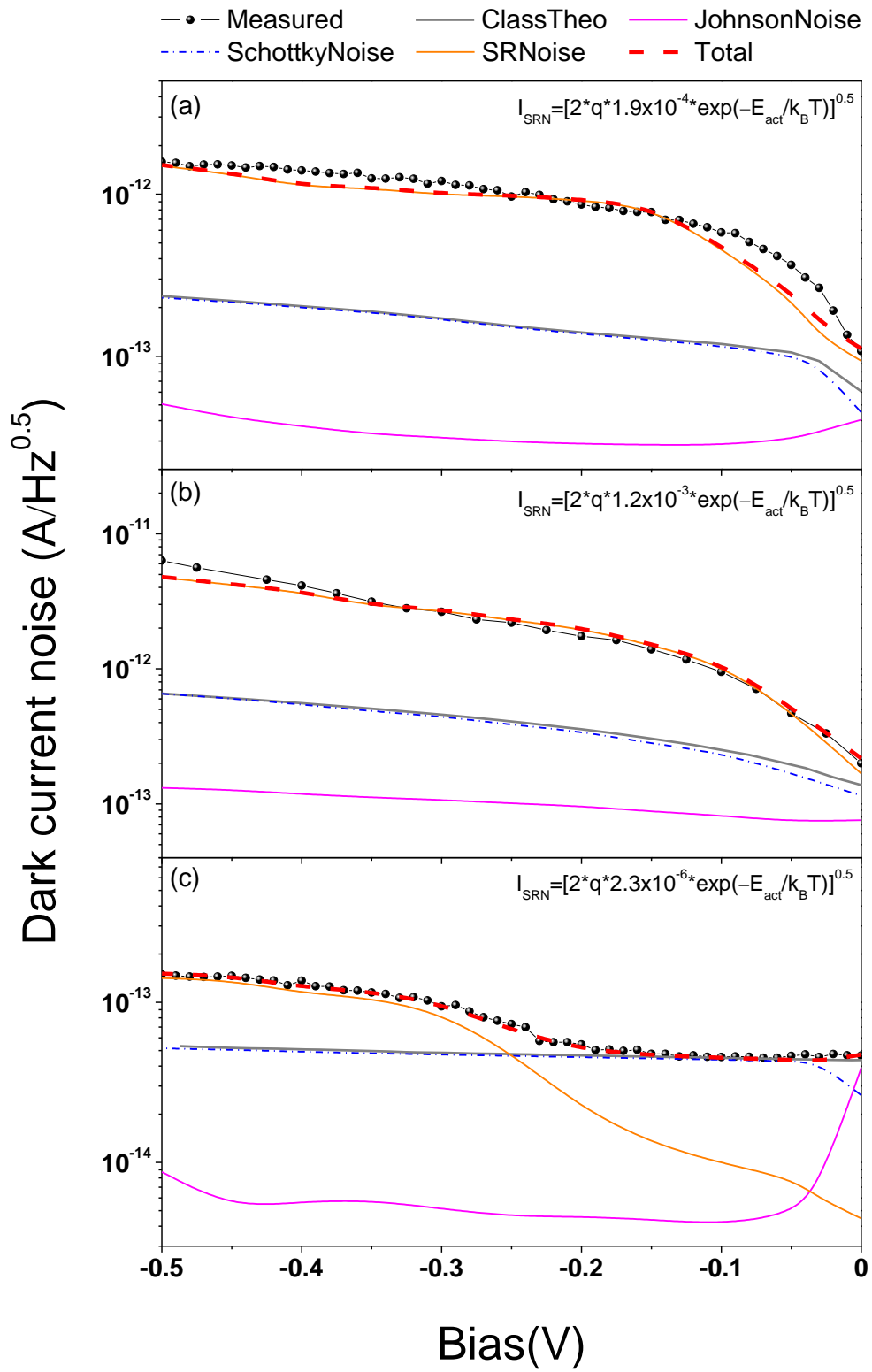
Figure 5.13 Total current noise curves after adding surface recombination noise.

The figure contains three panels (a), (b), (c) showing Dark current noise (A/Hz$^{0.5}$) versus Bias(V). The legend includes: Measured, ClassTheo, JohnsonNoise, SchottkyNoise, SRNoise, Total.

Panel (a): $I_{SRN}=[2*q*1.9\times10^{-4}*\exp(-E_{act}/k_BT)]^{0.5}$

Panel (b): $I_{SRN}=[2*q*1.2\times10^{-3}*\exp(-E_{act}/k_BT)]^{0.5}$

Panel (c): $I_{SRN}=[2*q*2.3\times10^{-6}*\exp(-E_{act}/k_BT)]^{0.5}$

CHAPTER 6

CONCLUSION

This thesis is focused on characterization of Mid-IR InAs/GaSb superlattice single pixel photodetectors designed and fabricated in collaboration with research groups from Anadolu University and Bilkent University. Superlattice detector technology has many potential advantages over other detectors systems available in the market today. The effective bandgap of the Type-II Superlattice can be tailored over a wide range which results multi-color FPA applications. Reduced tunneling currents and reduced Auger recombination lead to low leakage currents and high detectivity values. High quantum efficiency and responsivity can be reached by growing extremely thick (~6 μm) active regions. In contrast to QWIPs, normal incidence absorption is permitted which results in high quantum efficiency. Mature large-format FPA production of III-V semiconductor materials technology also offers technological advantages for the SLs.

In Chapter 1 of this study, the general concept of infrared detection was presented. Detection principles, limitations, detector types were presented. Advantages and disadvantages of competitive infrared detector technologies were discussed.

In Chapter 2, we presented theoretical aspect of the SL technology. Basic operation principles and general properties of superlattice detectors were introduced and common superlattice detector types were described. MBE growth technique was shortly described. Structures and design of SL2, SL3, SL4

and SLN samples were presented. In this chapter, steps of device fabrication and ALD deposited Al_2O_3, PECVD deposited Si_3N_4 and SiO_2 passivation layers were also described briefly. (All device fabrications were carried out by our collaborator at Bilkent University).

The objective of Chapter 3 was to introduce the characterization techniques and experimental setups comprehensively. First, an introduction to measurement system was given. Then, figures of merit for infrared detectors were given. Responsivity and response time characterizations were describe in optical characterization section. Responsivity is output signal per power of incoming photon flux. The responsivity measurement has two steps: spectral measurement using FTIR and peak responsivity with a calibrated blackbody source. The responsivity curve obtained from spectral measurement is multiplied with the peak responsivity value of the pixel calculated from equations inserted the signal obtained from peak responsivity measurement. Responsivity values can be converted to quantum efficiency, the number of electrons generated per number of incoming photon. Response time indicates the time required for a detector to reach $(1 - 1/e)$ of its maximum steady state signal value from zero. This measurement was carried out with a spectrum analyzer instrument.

Dark current vs. voltage, temperature dependent dark current vs. voltage and dark current noise measurement techniques and setups were also introduced in Chapter 3. From current vs. voltage characteristics R_0A and RA values can be calculated. While dark current vs. voltage measurements were carried out with an open system liquid nitrogen cryostat, temperature dependent current vs. voltage measurements were carried out with a closed loop liquid helium cryostat between temperature ranges of 10K to 250K with 5K steps. In dark current noise measurements, frequency spectrum at specific bias voltage values and bias voltage dependency at specific frequency value of photodiodes were investigated. Measurements were carried out in a Faraday Cage in order to prevent interference from external electromagnetic waves.

The results of optical and electrical measurements were presented in Chapter 4. Responsivity and quantum efficiency results were given for unpassivated SL2, SL3, SL4 samples, Si_3N_4, SiO_2 and Al_2O_3 passivated SL3 sample and SiO_2 passivated SLN sample. In the new device structure called "N" type, insertion of AlSb barrier in the superlattice, led to lower in the responsivity and quantum efficiency values to 0.35A/W and 14% respectively. In the comparison of unpassivated samples, SL4 sample showed the highest peak responsivity value of 1.27A/W. Responsivity values of SL3 and SL2 samples are 1.2A/W and 1.15A/W respectively. We saw that the responsivity correlates well with the thicknesses of the active absorbing region of the diodes. Peak quantum efficiency values are 45%, 43% and 39% for SL3, SL4 and SL2 samples. The contradiction between peak responsivity values and peak quantum efficiency values was explained by the energy difference of photon at 3μm and 4μm. Effects of passivation layers on optical characteristics were also studied. Si_3N_4 passivation layer degraded the optical performance of photodiode, peak responsivity value decreased to 1.08A/W and peak quantum efficiency value decreased to 40% of SL3 sample. These results might be consequences of absorbing/scattering of IR radiation and/or creating more surface states by Si_3N_4 layer. By filling trap states, peak responsivity and peak quantum efficiency values of Al_2O_3 passivated SL3 sample improved to 1.24A/W and to 46%. While SiO_2 passivation improved peak responsivity to 1.25A/W, it also decreased peak quantum efficiency to 41%. The possible explanation of this result was scattering/absorbing IR radiation at around 3μm by SiO_2 passivation layer. The peak responsivity of all samples increases with the reverse bias up to a point and drastically decreases with forward bias which as expected from p-n junction photodiodes. The response time value of SiO_2 passivated SL3 sample was around 100μs which is an average response time for infrared detectors. This result can be improved by increasing mobility of carriers by introducing fewer scattering defects. The responsivity and quantum efficiency results of Type-II SL single pixel photodetectors with straight forward design reached the

values in the literature and Table 2.1. Although, "N" structure design has lower responsivity, it can be improved by more intelligent design.

R_0A values calculated from dark I-V measurements for unpassivated SL2, SL3 and SL4 samples were found to be 31kΩ.cm^2, 17kΩ.cm^2 and 10kΩ.cm^2 respectively. The reason of these results lied in the fact that the more periods the structure have, the more electron-hole pairs are created. If the RA values are compared with the results in the literature, it can be concluded that the wafer quality needs to be improved for FPA applications. Effect of AlSb barrier was easily seen in R_0A value, it was 500kΩ.cm^2. While Si_3N_4 passivation layer degraded R_0A value to 9kΩ.cm^2, Al_2O_3 and SiO_2 passivation layers improved R_0A values to 64kΩ.cm^2 and 155kΩ.cm^2. RA results of straight forward design Type-II SL single pixel photodetectors are not so close to the best values in the literature. By doing modification in the design, results can be improved as in the "N" structure. With improvement in the crystal growth and fabricating the device more attentively, higher RA results can be reached.

In Chapter 5, we focused on the noise analysis of photodetectors. At the beginning, Schottky noise, Johnson noise and 1/f noise were introduced. Then, dark current noise vs. frequency results at zero bias and 0.1V reverse bias were presented for unpassivated and Si_3N_4 passivated SL3 samples. Dark current noise vs. bias voltage results at around 30Hz were also given for the same samples. It was seen that calculated white noise of detectors matched with the experimental values only at zero bias. In reverse bias region, there was an additional noise which had not been expected. Dark current noise vs. frequency results at zero bias and 0.3V reverse bias and dark current noise vs. bias voltage results at around 30Hz for SiO_2 passivated SL3 sample was also given. SiO_2 passivation suppressed the additional noise up to 0.18V reverse bias.

Detectivity values were given also in Chapter 5. At zero bias, all detectivity values calculated using white noise values matched with the detectivity value calculated using experimental noise data. They were 2.9×10^{11} Jones for Si_3N_4 passivated SL3 sample, 6×10^{11} Jones for unpassivated SL4 sample, 6.4×10^{11}

Jones for unpassivated SL3 sample, 9.5×10^{11} Jones for unpassivated SL2 sample, 1.8×10^{12} Jones for SiO_2 passivated SL3 sample, 2×10^{12} Jones for SiO_2 passivated SLN sample and 2.7×10^{12} Jones for Al_2O_3 passivated sample. It is clearly seen that the detectivity results calculated with white noise data did not reflect true detectivity values for unpassivated SL3 sample. SiO_2 passivated SLN sample was very close to the highest detectivity results in the literature (Table 2.1) even if the responsivity value of that sample is very low. Therefore, SLN sample can compete with the results in the literature by increasing its responsivity.

In order to verify the dominated current mechanisms at different temperature ranges, temperature dependent I-V measurements and Arrhenius Plot analysis were carried out. In Arrhenius plot, slopes of 3 different current mechanisms, namely diffusion, R-G and surface limited, were seen for different temperature regions. From these slopes, activation energies at different bias voltages were calculated. Activation energy of diffusion current mechanism matched with the cut-off wavelength obtained from optical measurements. By using activation energy of surface limited current mechanism, surface current and surface recombination noises were proposed. An excellent agreement between fitted curves and experimental data was obtained.

REFERENCES

[1] E.A. Plis, "Mid-IR Type-II InAs/GaSb Nanoscale Superlattice Sensors," *Ph.D. Thesis*, p. 5, 2007.

[2] A. Rogalski, "History of Infrared Detectors," *Opto-Electronics Review*, vol. 20, no. 3, pp. 279-308, 2012.

[3] E.A. Plis, "Mid-IR Type-II InAs/GaSb Nanoscale Superlattice Sensors," *Ph.D. Thesis*, pp. 24-28, 2007.

[4] G. Cohensol, and Y. Riant, "Epitaxial (CdHg)Te Infrared Photovoltaic Detectors," *Applied Physics Letters*, vol. 19, no. 10, p. 436, 1971.

[5] E.A. Plis, "Mid-IR Type-II InAs/GaSb Nanoscale Superlattice Sensors," *Ph.D. Thesis*, p. 24, 2007.

[6] P. Norton, "HgCdTe Infrared Detectors," *Optoelectronics Review*, vol. 10, no. 3, pp. 159-174, 2002.

[7] R. Joyce, D.B. Hall, R.S. Aikens, and T.W. McCurnin, "Johnson Noise Limited Operation of Photovoltaic InSb Detectors," *Applied Optics*, vol. 14, pp. 450-455, 1975.

[8] B. F. Levine, "Quantum-Well Infrared Photodetectors," *Journal of Applied Physics*, vol. 74, pp. R1-R76, 1993.

[9] R. Tsu, L. Esaki, and B.A. Sai-Halasz, "A New Semiconductor Superlattice," *Applied Physics Letters*, vol. 30, pp. 651–653, 1977.

[10] D.L. Smith, and C. Mailhiot, "Proposal For Strained Type-II Superlattice Infrared Detectors," *Journal Of Applied Physics*, vol. 62, pp. 2545–2548, 1987.

[11] R. Esaki, and L. Tsu, "Research Note. Technical Report Rc-2418," IBM, 1969.

[12] M.R. Kitchin, and M. Jaros, "Characterization of GaSb/InAs Type-II Infrared Detectors at Very Long Wavelengths: Carrier Scattering at Defect Clusters," *Physica E*, vol. 18, pp.

498-508, 2003.

[13] G.C. Dente, and M.L. Tilton, "Pseudopotential Methods for Superlattices: Applications to Mid-Infrared Semiconductor Lasers," *Journal Of Applied Physics*, vol. 86, pp. 1420-1429, 1999.

[14] C. Grein, P. Young, H. Ehrenreich, and T. Mcgill, "Auger Lifetimes in Ideal InGaSb/InAs Superlattices," *Journal Of Electronic Materials*, vol. 22, no. 8, pp. 1093 - 1096, 1993.

[15] C. H. Grein, H. Cruz, M. E. Flatte, and H. Ehrenreich, "Theoretical Performance of Very Long Wavelength InAs/InxGa1-xSb Superlattice Based Infrared Detectors," *Applied Physics Letters*, vol. 65, no. 20, pp. 2530 - 2532, 1994.

[16] Y. Wei, and M. Razeghi, "Modeling of Type-II InAs/GaSb Superlattices Using an Empirical Tight-Binding Method and Interface Engineering," *Physical Review B - Condensed Matter and Materials Physics*, vol. 69, no. 8, p. 085316, 2004.

[17] P. Piquini, and A. Zunger, "Pseudopotential Calculations of Band Gaps and Band Edges of Short-Period (InAs)n∕(GaSb)m Superlattices with Different Substrates, Layer Orientations, and Interfacial Bonds," *Physical Review B - Condense Matter and Materials Physics*, vol. 77, no. 11, p. 115314, 2008.

[18] E.A. Plis, "Mid-IR Type-II InAs/GaSb Nanoscale Superlattice Sensors," *Ph.D. Thesis*, p. 39, 2007.

[19] M. Razeghi, and B.-M. Nguyen, "Band Gap Tunability of Type-II Antimonide-Based Superlattices," *Physics Procedia*, vol. 3, no. 2, pp. 1207-1212, 2010.

[20] G. C. Osbourn, "InAsSb Strained-Layer Superlattices for Long Wavelength Detector Applications," *Journal of Vacuum Science & Technology B*, vol. 2, no. 2, p. 176, 1984.

[21] S. R. Kurtz, G. C. Osbourn, R. M. Biefeld, L. R. Dawson, and H. J. Stein, "Extended Infrared Response of InAsSb Strained-Layer Superlattices," *Applied Physics Letters*, vol. 52, no. 10, p. 831, 1988.

[22] A. Rogalski, "Comparison of the Performance of Quantum Well and Conventional Bulk Infrared Photodetectors," *Infrared Physics & Technology*, vol. 38, pp. 295-310, 1997.

[23] S. Maimon, and G. W. Wicks, "nBn Detector, an Infrared detector with Reduced Dark Current and Higher Operating Temperature," *Applied Physics Letters*, vol. 89, no. 15, p. 151106, 2006.

[24] J. B. Rodriguez, E. Plis, G. Bishop, Y. D. Sharma, H. Kim, L. R. Dawson, and S. Krishna, "nBn Structure Based on InAs/GaSb Type-II Strained Layer Superlattices," *Applied Physics Letters*, vol. 91, p. 043514, 2007.

[25] S. J. Lee, S. K. Noh, E. Plis, S. Krishna, and K.-S. Lee, "Subband Transitions in Dual-Band n-B-n InAs/GaSb Superlattice Infrared Photodetector Identified by Photoresponse Spectra," *Applied Physics Letters*, vol. 95, p. 102106, 2009.

[26] H. S. Kim, E. Plis, J. B. Rodriguez, G. D. Bishop, Y. D. Sharma, and L. R. Dawson, "Mid-IR Focal Plane Array Based on Type-II InAs/GaSb Strain Layer Superlattice Detector with nBn Design," *Applied Physics Letters*, vol. 92, p. 183502, 2008.

[27] M. A. Kinch, J. D. Beck, C.-F.Wan, F. Ma, and J. Campbell, "HgCdTe Avalanche Photodiodes," *J. Electron. Mater.*, vol. 33, no. 6, pp. 630-639, 2004.

[28] J. Beck, C. Wan, M. Kinch, J. Robinson, P. Mitra, R. Scritchfield, F. Ma, and J. Campbell, "The HgCdTe Electron Avalanche Photodiode," *J. Electonic Mat.*, vol. 35, pp. 1166-1173, 2006.

[29] S. Mallick, K. Banerjee, S. Ghosh, J. B. Rodriguez, and S. Krishna, "Midwavelength Infrared Avalanche Photodiode Using InAs–GaSb Strain Layer Superlattice," *IEEE Photonics Technology Letters*, vol. 19, no. 22, pp. 1843-1845, 2007.

[30] S. Mallick, K. Banerjee, S. Ghosha, Elena Plis, J. B. Rodriguez, S. Krishna, and C. Grein, "Ultralow Noise Midwave Infrared InAs–GaSb Strain Layer Superlattice Avalanche Photodiode," *Applied Physics Letters*, vol. 91, p. 241111, 2007.

[31] P.-Y Delaunay, B.-M. Nguyen, D. Hoffman, A. Hood, E. K.-W. Huang, M. Razeghi, and M. Z. Tidrow, "High Quantum Efficiency Two Color Type-II InAs/GaSb n-i-p-p-i-n Photodiodes," *Applied Physics Letters*, vol. 92, no. 11, p. 111112, 2008.

[32] R. Rehm, M. Walther , J. Fleißner, J. Schmitz, J. Ziegler, W. Cabanski, and R. Breiter, "Bispectral Thermal Imaging with Quantum Well Infrared Photodetectors and InAs/GaSb Type-II Superlattices," *Society Of Photo-Optical Instrumentation Engineers*, 2006.

[33] O. Salihoglu, A. Muti, K. Kutluer, T. Tansel, A. Aydinli, and R. Turan, ""N" Structure for Type-II Superlattice Photodetectors," *Applied Physics Letters*, vol. 101, p. 073505, 2012.

[34] H. S. Kim, E. Plis, A. Khoshakhlagh, S. Myers, N. Gautam, Y. D. Sharma, L. R. Dawson, S. Krishna, S. J. Lee, and S. K. Noh, "Performance Improvement of InAs/GaSb Strained Layer Superlattice Detectors by Reducing Surface Leakage Currents with SU-8 Passivation," *Applied Physics Letters*, vol. 96, no. 3, p. 033502, 2010.

[35] M. Walther, J. Schmitz, R. Rehm, S. Kopta, F. Fuchs, J. Fleißner, W. Cabanski, and J. Ziegler, "Growth of InAs/GaSb Short-Period Superlattices for High-Resolution Mid-Wavelength Infrared Focal Plane Array Detectors," *Journal of Crystal Growth*, vol. 278, pp. 156-161, 2005.

[36] S. Mou, S. Gunapala, J. Mumolo, C. J. Hill, J. V. Li, and S.-L. Chuang, "Midinfrared Type-II InAs/GaSb Superlattice Photodiodes Toward Room Temperature Operation," *Applied Physics Letters*, vol. 93, no. 16, p. 163505, 2008.

[37] B.-M. Nguyen, D. Hoffman, E. K.-w. Huang, S. Bogdanov, P.-Y. Delaunay, M. Razeghi, and M. Z. Tidrow, "Demonstration of Midinfrared Type-II InAs/GaSb Superlattice Photodiodes Grown on GaAs Substrate," *Applied Physics Letters*, vol. 94, no. 22, p. 223506, 2009.

[38] Y. Wei, A. Hood, H. Yau, A. Gin, M. Z. Tidrow, V. Nathan, and M. Razeghi, "Uncooled Operation of Type-II InAs/GaSb Superlattice Photodiodes in the Widwavelength Infrared Range," *Applied Physics Letters* , vol. 86, no. 23, p. 233106, 2005.

[39] G. Chen, B.-M. Nguyen, A. M. Hoang, E. K. Huang, S. R. Darvish, and M. Razeghi, "Elimination of Surface Leakage in Gate Controlled Type-II InAs/GaSb Mid-Infrared Photodetectors," *Applied Physics Letters*, vol. 99, no. 18, p. 183503, 2011.

[40] E.A. Plis, "Mid-IR Type-II InAs/GaSb Nanoscale Superlattice Sensors," *Ph.D. Thesis*, p. 62, 2007.

[41] R. Chaghi, C. Cervera, H. Aït-Kaci, P. Grech, J. B. Rodriguez, and P. Christol, "Wet Etching and Chemical Polishing of InAs/GaSb Superlattice Photodiodes," *Semiconductor Science and Technology*, vol. 24, no. 6, p. 065010, 2009.

[42] M. B. Weissman, "1/f Noise and Other Slow, Nonexponential Kinetics in Condensed Matter," *Reviews of Modern Physics*, vol. 60, no. 2, pp. 537-571, 1988.

[43] O. Salihoglu, A. Muti, K. Kutluer, T. Tansel, R. Turan, C. Kocabas, and A. Aydinli, "Atomic Layer Deposited Al2O3 Passivation of Type-II InAs/GaSb Superlattice Photodetectors," *Journal of Applied Physics*, vol. 111, p. 074509, 2012.

[44] H. Mohseni, E. Michel, J. Sandoen, W. Mitchel, G. Brown, and M. Razeghi, "Growth and Characterization of InAs/GaSb Photoconductors for Long Wavelength Infrared Range," *Applied Physics Letters*, vol. 71, no. 10, pp. 1403-1405, 1997.

[45] C. Besikci, *Infrared Devices and Systems*. Ankara, Turkey: METU, 2008.

[46] J. D. Vincent, *Fundamentals of IR Operation and Testing*.: John Wiley & Sons, 1990.

[47] J. Ready, "Optical Detectors and Human Vision," in *Fundamentals of Photonics*.: John Wiley & Sons, 1991, ch. 6, p. 219.

[48] E. Plis, J. B. Rodriguez, and S. Krishna, *InAs/(In)GaSb Type-II Strain Layer Superlattice Detectors*.: Elsevier, 2011, p. 19.

[49] T. Tansel, K. Kutluer, Ö. Salihoglu, A. Aydinli, B. Aslan, B. Arikan, M. C. Kilinc, Y. Ergun, U. Serincan, and R. Turan, "Effect of the Passivation Layer on the Noise Characteristics of Mid-Wave-Infrared InAs/GaSb Superlattice Photodiodes," *Journal of Applied Physics*, vol. 24, no. 9, pp. 790-792, 2012.

[50] S. Mou, J. V. Li, and S. L. Chuang, "Surface Channel Current in InAs/GaSb Type-II Superlattice Photodiodes," *Journal of Applied Physics*, vol. 102, no. 6, p. 066103, 2007.

[51] C. A. Vergers, *Handbook of Electrical Noise: Measurement and Technology*.: Tab Professional and Reference Books, 1987.

APPENDIX A

LABVIEW VIRTUAL INSTRUMENTS

In Appendix A, front and block panels of VIs written for this study are presented. Figure A.1, A.3 and A.5 show the front panels of dark I-V, responsivity and noise measurement VIs respectively. Figure A.2, A.4 and A.5 show the block panels of the same VIs. Dark I-V VI is written for Keithley 6487 picoammeter / voltage source instrument. Responsivity VI is independent of any instrument; it is for calculating the responsivity value. Noise measurement VI is written for SRS SR570 current preamplifier and SRS SR 760 spectrum analyzer instruments.
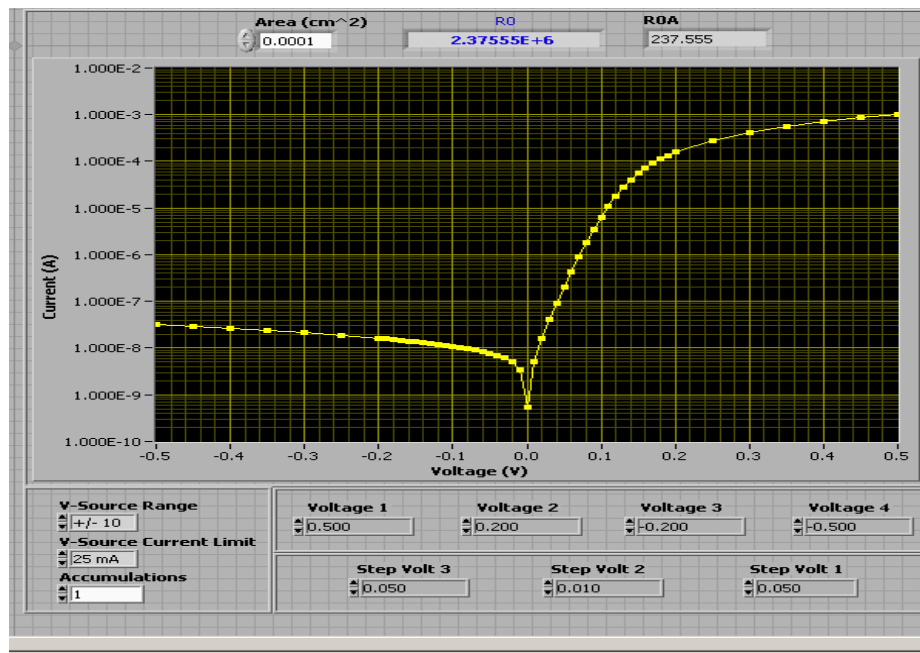

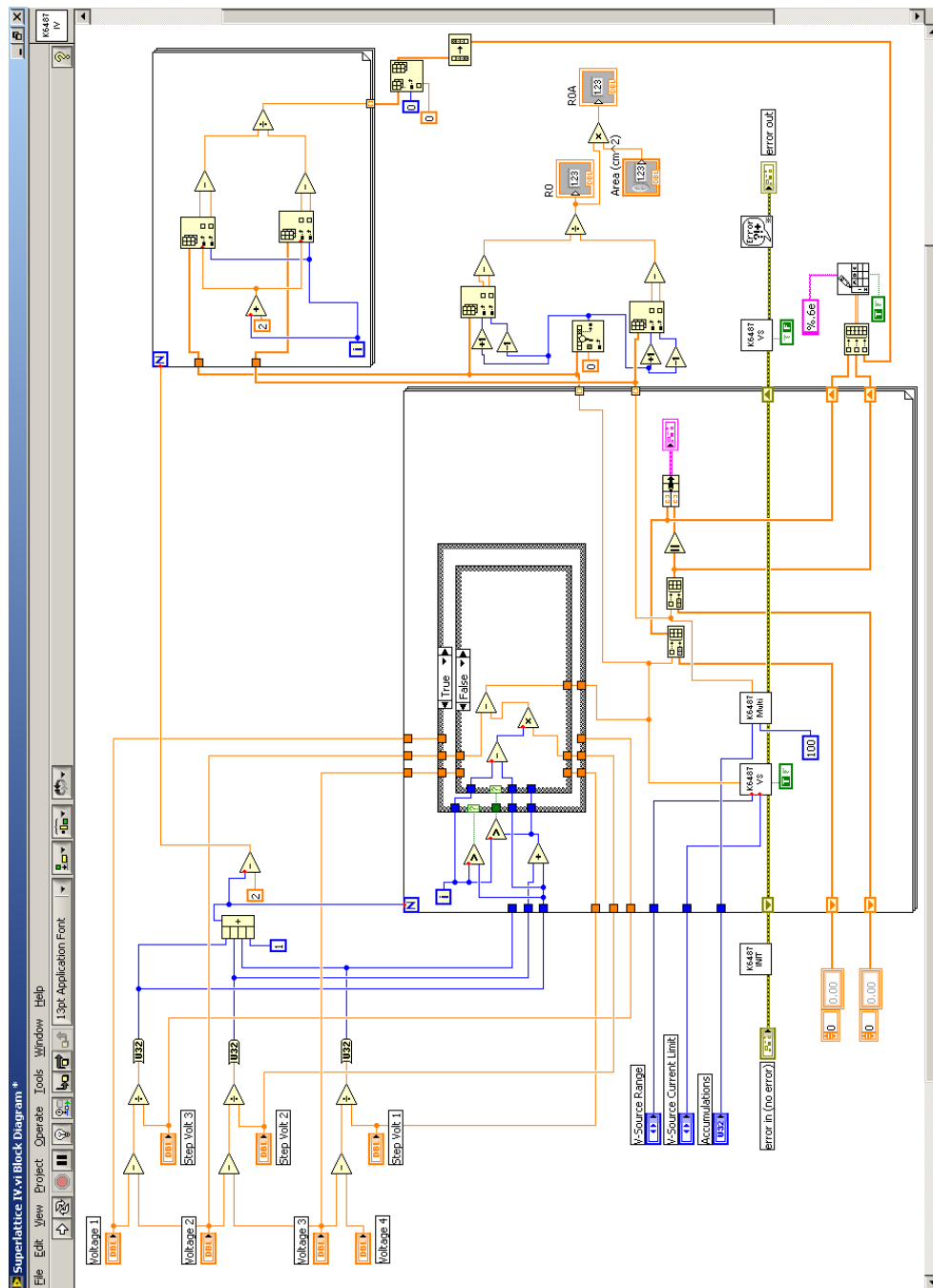**Figure A.1 Front panel of the vi for dark I-V measurements.**

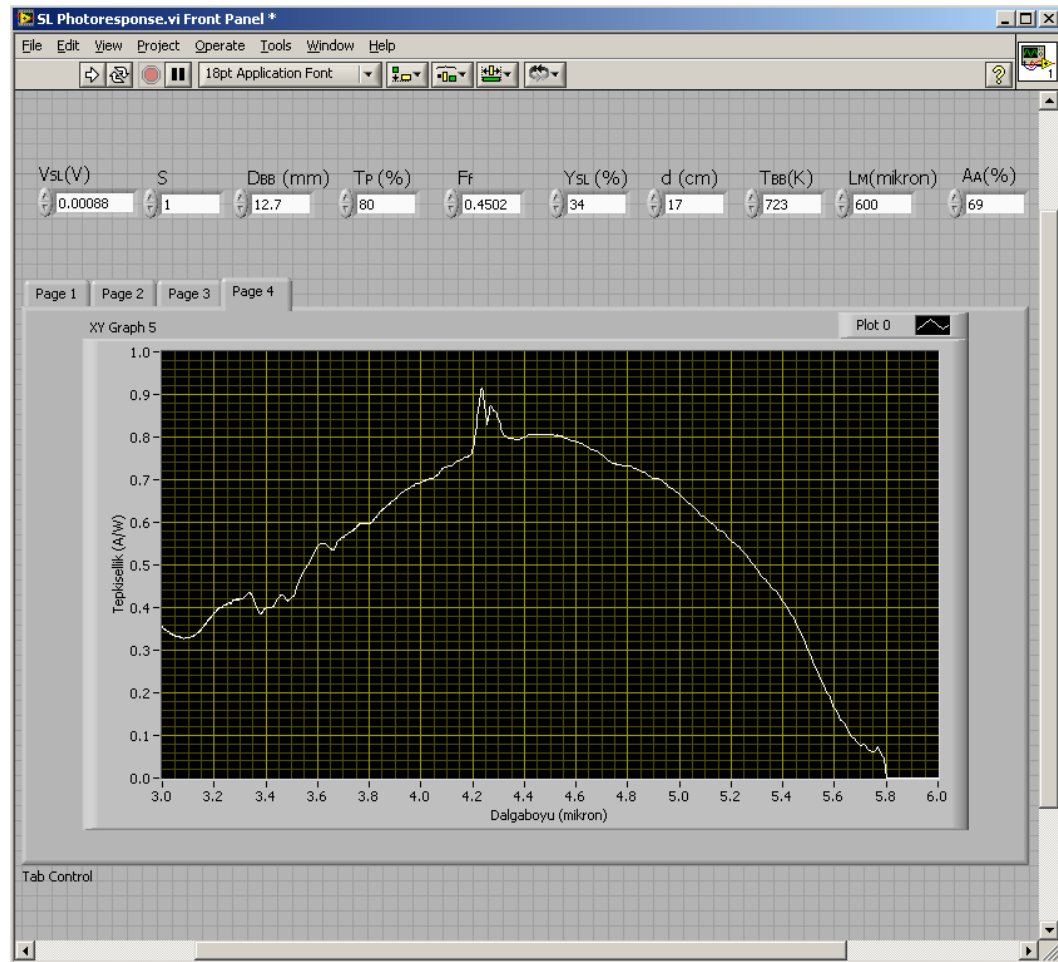**Figure A.2 Block panel of the vi for dark I-V measurements.**

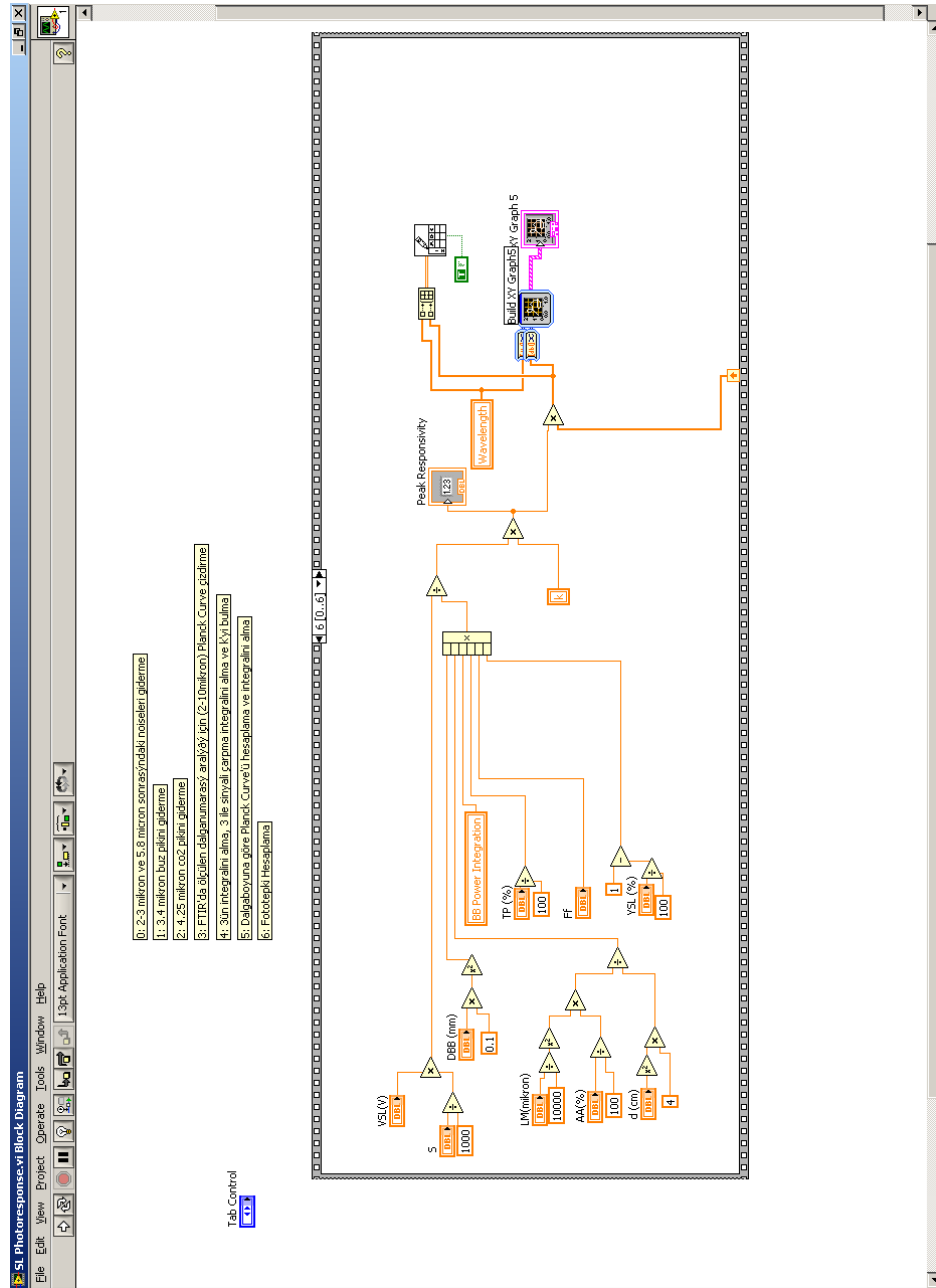**Figure A.3 Front panel of the vi for responsivity measurements.**

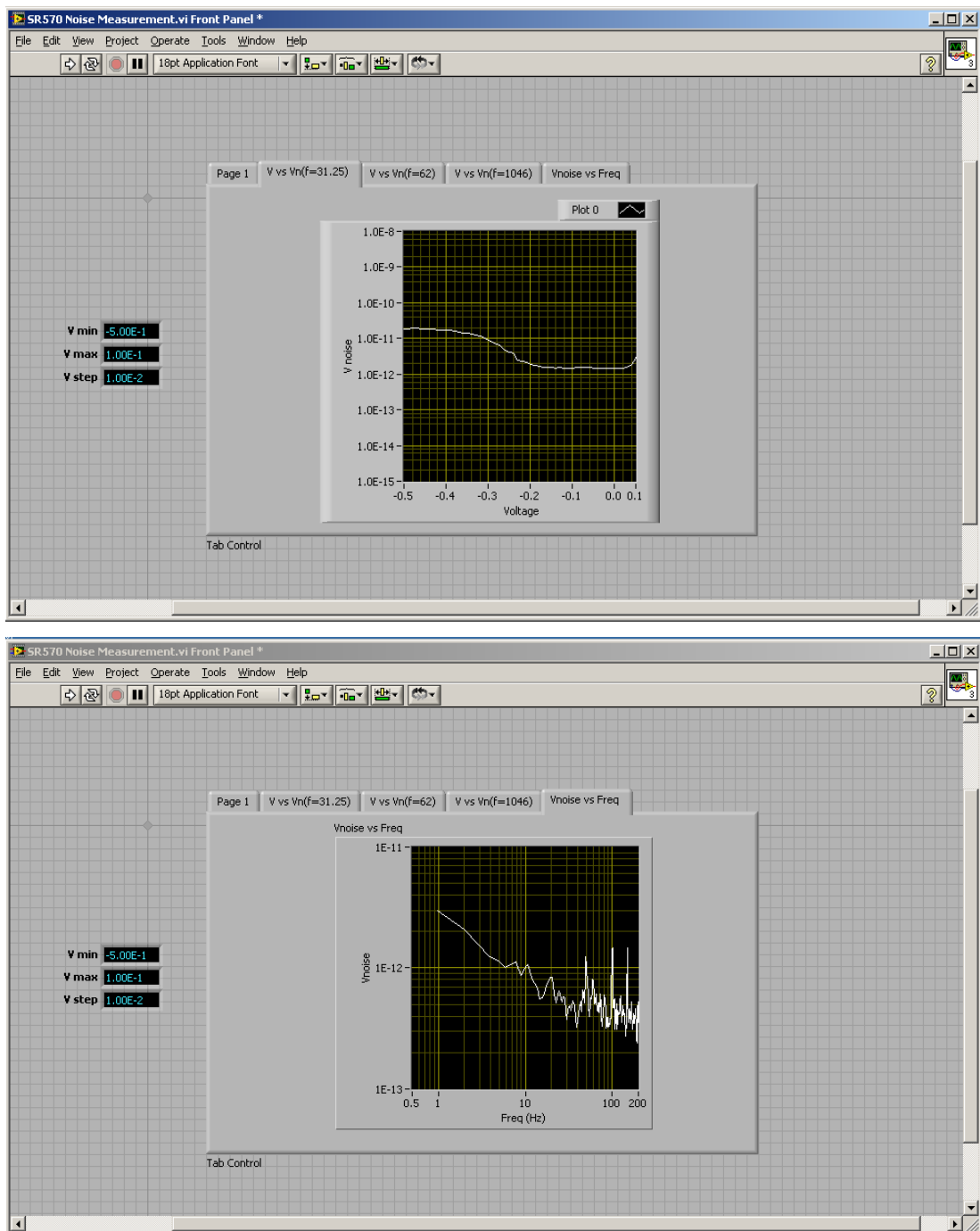**Figure A.4 Block panel of the vi for responsivity measurements.**

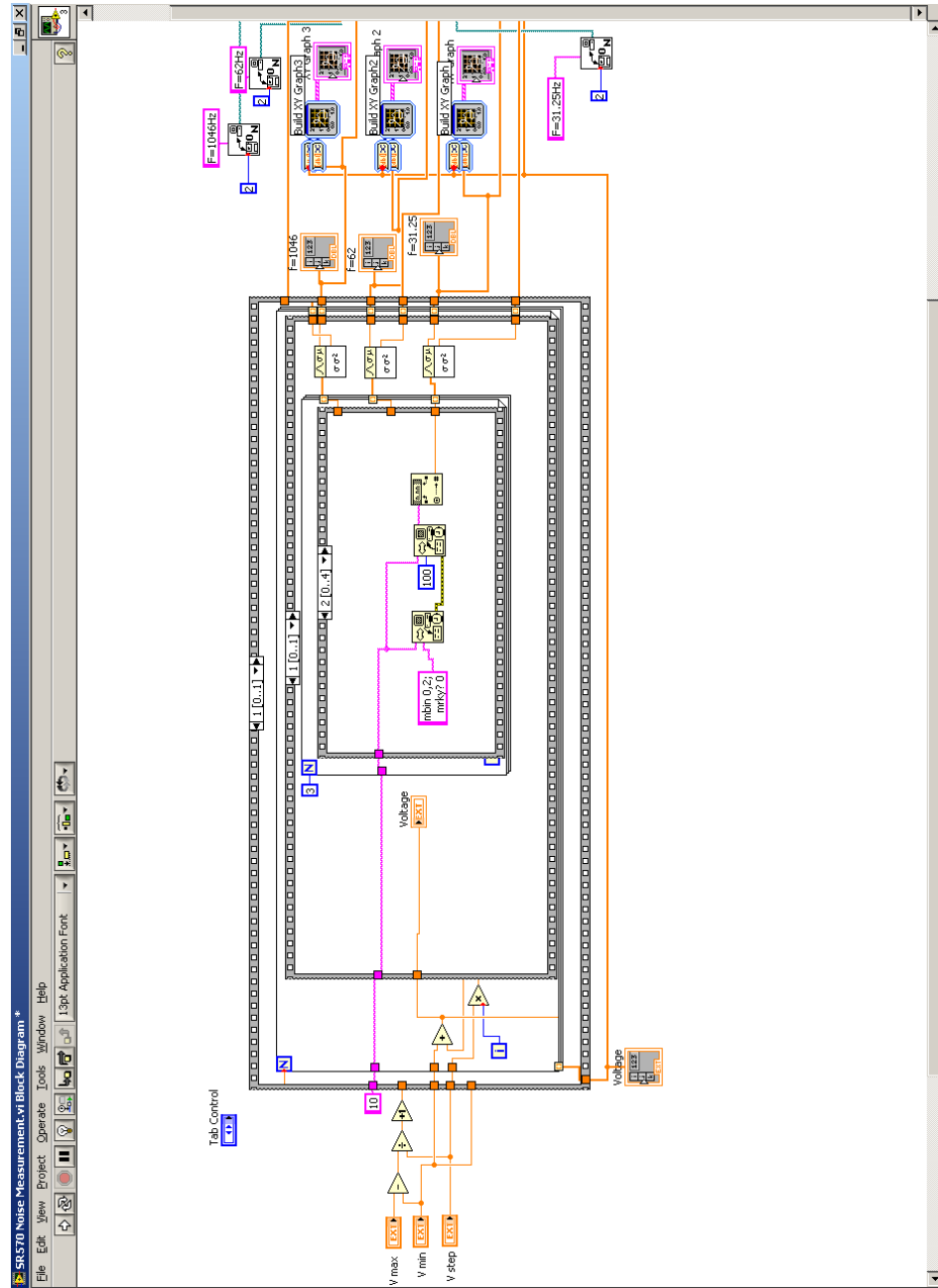**Figure A.5 Front panels of the vi for noise measurements.**

Figure A.6 Block panel of the vi for noise measurements.

CURRICULUM VITAE

PERSONAL INFORMATION

Surname, Name: Kutluer, Kutlu
Nationality: Turkish
Date and Place of Birth: 1985, İstanbul
Web: kutlukutluer.com
email: kutlu@istanbul.com

EDUCATION

Degree	Institution	Year of Graduation
BS	METU Department of Physics	2009
MS	METU Micro and Nanotechnolgy Department	2012

WORK EXPERIENCE

Year	Place	Enrollment
2006-2007	Bilimadami.net	Administrator
2005-2010	Spymastersnake.org	Co-Admin
2009-2012	METU Department of Physics	Scientific Research Expert

FOREIGN LANGUAGES

Fluent English, Beginner German

PUBLICATIONS

1. T. Tansel, **K. Kutluer**, O. Salihoglu, A. Aydinli, B. Aslan, B. Arikan, M.C. Kilinc, Y. Ergun, U. Serincan, and R. Turan, "Effect of the Passivation Layer on the Noise Characteristics of Mid-Wave Infrared InAs/GaSb Superlattice Photodiodes," *IEEE Photonics Technology Letters*, Vol. 24, No. 9, pp.790-792, 2012.

2. O. Salihoglu, A. Muti, **K. Kutluer**, T. Tansel, C. Kosabas, R. Turan, and A. Aydinli, "Atomic Layer Deposited Al_2O_3 Passivation of Type II InAs/GaSb Superlattice Photodetectors," *Journal of Applied Physics*, Vo. 111, 074509, 2012.

3. O. Salihoglu, **K. Kutluer**, A. Muti, T. Tansel, R. Turan, Y. Ergun, and A. Aydinli, "'N' Structure for MWIR Type-II InAs/GaSb Superlattice Detectors," *Applied Physics Letters* 101, 073505 (2012).

4. O. Salihoglu, A. Muti, **K. Kutluer**, T. Tansel, R. Turan, and A. Aydinli, "Skin Like Self Assembled Monolayers on InAs/GaSb Superlattice Photodetectors," *Journal of Physics D* 45, (2012), 365102.

5. O. Salihoglu, A. Muti, **K.Kutluer**, T. Tansel, R. Turan, C. Kocabas, and A. Aydinli, "Passivation of type II InAs/GaSb superlattice photodetectors with atomic layer deposited Al_2O_3," *Proc. of SPIE* Vol. 8353 83530Z-2, 2012.

6. T. Tansel, **K. Kutluer**, O. Salihoglu, A. Muti, A. Aydinli and R. Turan, "Understanding Noise Mechanisms in InAs/GaSb Superlattice Photodiodes," *Applied Physics Letters* (Submitted).